공학박사학위논문

연소 환경 진단을 위한 고속 및 고정확도 화염 자발광 분광법에 관한 연구

A Study of Flame Emission Spectroscopy for Fast Time-Resolved and High Accuracy Combustion Diagnostics

2023년 2월

서울대학교 대학원

기계항공공학부

윤 태 근

연소 환경 진단을 위한 고속 및 고정확도 화염 자발광 분광법에 관한 연구

A Study of Flame Emission Spectroscopy for Fast Time-Resolved and High Accuracy Combustion Diagnostics

지도교수 도 형 록

이 논문을 공학박사 학위논문으로 제출함

2022 년 10 월

서울대학교 대학원

기계항공공학부

윤 태 근

윤태근의 공학박사 학위논문을 인준함

2022 년 12 월

위 원 장 : 고 승 환 (인)

부위원장 : 도 형 록 (인)

위 원 : 송 한 호 (인)

위 원 : 이 관 중 (인)

위 원 : 임 성 균 (인)

ABSTRACT

A Study of Flame Emission Spectroscopy for Fast Time-Resolved and High Accuracy Combustion Diagnostics

Taekeun Yoon
Department of Mechanical and Aerospace Engineering
The Graduate School
Seoul National University

Remarkable combustion techniques have been developed to deal with environmental issues while maintaining the efficiency, stability, and performance of combustion. To operate recent combustors optimally, the gas properties in the reaction zones should be monitored quickly and accurately as well as instantaneously controlled. Flame emission spectroscopy (FES) is one of the candidate solutions for providing accurate gas properties measurements in real-time. This is because FES is a non-intrusive optical method that uses spontaneous and instantaneous emission spectra to estimate gas properties with the simplest experimental setup utilizing only detector systems. However, as the exposure time is reduced to increase the data acquisition rate, the signal-to-noise ratio (SNR) of the flame emission spectrum

decreases as well reducing the accuracy of the FES measurements. On the other hand, even if it is possible to collect signals with a high SNR, it is challenging to predict gas properties directly from the signals because of the requirement for complete chemical reaction path modeling of chemiluminescence. Therefore, predicting gas properties from emission spectra is achieved by a calibration process that correlates flame emission with gas properties. Conventional methods utilize one-to-one calibration functions by extracting local spectral features, such as band intensity ratio, and matching the features to gas properties. Nevertheless, the variations of spectral features are not always monotonic which makes the calibration process not straightforward.

This study mainly discusses the framework for improving the temporal resolution and accuracy of FES for predicting gas properties. A data-driven calibration framework that combines 1) deep learning-based denoising based on the convolutional neural network (CNN) architecture as a signal preprocessor, and 2) data-driven calibration technique using a reduced order model (ROM) consisting of proper orthogonal decomposition (POD) and Kriging model is proposed. A deep learning neural network supervised on data pairs of noisy and clean signals with a loss function that utilizes POD of the spectrum can enhance the SNR of the short-gated spectra with minimal information loss. Then, the POD method with a Kriging model mapping flame emission spectrum to the target gas properties predicts the gas properties from the processed spectra. To sum up, the proposed calibration method

can improve prediction accuracy of gas properties such as equivalence ratio and pressure using short-gated noisy signals.

The proposed combustion diagnosis method was applied to actual spontaneous flame emission spectra in high-pressure conditions. The gas property predictions of the proposed method were compared with experimental values measured by high-precision and high-accuracy sensors to estimate the accuracy and precision of the proposed method. The prediction accuracy and precision of the proposed method were evaluated using the average relative errors of prediction (REP) and the average relative standard deviation (RSD) of the gas predictions from the test spectrum data (not used for model training). The proposed method was investigated under combustion conditions in broad test ranges of equivalence ratio (0.8 – 1.2) and pressure (1 – 10 bar) of methane-air flame, taking a short-gated (0.05, 0.2, and 0.4 s) flame emission spectrum with low SNR as input. It was confirmed that the proposed framework enables flame emission spectroscopy to achieve high accuracy and fast temporal resolution.

Keywords: Combustion Diagnostics, Chemiluminescence, Flame Emission Spectroscopy, Convolutional Neural Network, Proper Orthogonal Decomposition

Student Number: 2017-26386

Table of Contents

List of Tables

List of Figures

Nomenclatures

Latin characters

A	Einstein coefficient
B	spectral radiance
c	speed of light
E	radiant thermal energy
f	surrogate model
h	Planck constant
k	Boltzmann constant
I	photon emission rate
I_{dark}	dark current
L	loss function
$\dot{m}_a$	air mass flow rate
$\dot{m}_f$	fuel mass flow rate
N_c	number of channels
N_d	number of sub-signals
$N_{electron}$	number of counted electrons
N_k	number of kernel size
N_l	number of layers
N_M	number of selected POD basis
N_p	number of CNN parameter
N_R	read noise
N_S	number of data sample
N_{shot}	number of spectral shots
N_{test}	number of test case

N_{train}	number of training case
P	pressure
S_k	main effect sensitivity index
S_{kl}	coupled effect sensitivity index
T	absolute temperature
T_{ad}	adiabatic temperature
T_0	cosine annealing cycle step size
T_{mult}	cosine annealing cycle magnification
T_{up}	cosine annealing linear warmup step size
V	variance
W	number of components in input signal
U_i	i^{th} spectral signal
$\overline{\boldsymbol{U}}$	averaged spectral signal
x_i	short-gated spectrum
y_i	long-gated spectrum
$\hat{y}_i$	denoised short-gated spectrum

Greek symbols

α	constant defined in Eq. (4.2)
$\alpha_{i,j}$	POD coefficient of φ_j in U_i
γ	cosine annealing decrease rate of max learning rate
η	quantum efficiency
η_{max}	cosine annealing max learning rate
ν	light frequency
$\pi_{i,j}$	gas properties measured by the sensors
$\hat{\pi}_{i,j}$	estimated gas property
σ	Stefan-Boltzmann constant
σ_{Photon}	photon noise

σ_{Dark}	dark noise
σ_{Read}	readout noise
ϕ	equivalence ratio
φ_j	j^{th} POD basis
ϕ_p	photon flux at the CCD
χ	species concentration

Abbreviations

ANN	artificial neural network
BIR	band intensity ratio
BI2	band intensity of BB and H_2O*
BI3	band intensity of OH*, CH*, and C_2*
BI5	band intensity of OH*, CH*, C_2*, BB and H_2O*
BB	broadband
BN	batch normalization
CCD	charge-coupled device
CCS	carbon capturing and storage
CNN	convolutional neural network
Conv	convolution
DU	down- and up-sampling
FES	flame emission spectroscopy
FGR	flue gas recirculation
GSA	global sensitivity analysis
HS	high-SNR
IEA	International Energy Agency
IPCC	intergovernmental panel on climate change
LOOCV	leave-one-out cross-validation
LS	low-SNR
MLR	multi linear regression

MSE	mean square error
PLS-R	partial least-squares regression
POD	proper orthogonal decomposition
REA	average relative errors of spectral area
REC	average relative errors of calibration
ReLU	rectified linear unit
REP	average relative errors of prediction
REV	average relative errors of validation data
ROM	reduced order model
RSD	average relative standard deviations
RQL	rich-quench-lean
SNR	signal-to-noise ratio
TES	total energy supply

CHAPTER 1. INTRODUCTION

1.1 Background and Motivation

Modern civilization has heavily relied on combustion-based energy infrastructures. Up until very recently, combustion was the main source of energy conversion in the world. According to the International Energy Agency (IEA), 90% of the total energy supply (TES) is based on combustion, including the use of biofuels and fossil fuels such as coal, natural gas, and oil in over 170 countries and regions, as shown in Figure 1.1 [1]. Given the difficulty of developing renewable energy and the current proportion of renewable energy in TES, combustion will remain the primary energy source for power generation and transportation in the near future.

On the other hand, the combustion of fossil fuels and biofuels inevitably produces pollutants including NO_x, CO, particulate matter, and greenhouse gases such as CO_2. These by-products of combustion have negative effects on the environment, e.g., smog caused by CO and particulates, acid rain caused by NO_x, and global warming mainly caused by greenhouse gases. Countries around the world have addressed these issues by signing agreements such as the Kyoto Protocol (1997) and the Paris Agreement (2015) [2]. In particular for greenhouse gas emissions, the intergovernmental panel on climate change (IPCC) reported the importance of

achieving net-zero CO_2 emissions by 2050 in order to limit the increase in average global temperature by 1.5℃ before 2100 (IPCC, Incheon 2018). As a result, there has been a rapid increase in the number of governments making commitments to reduce carbon emissions to net-zero, as shown in Figure 1.2 reported by the IEA. In addition, these governments have set targets for reducing pollution and greenhouse gas emissions and have strictly regulated those emissions.

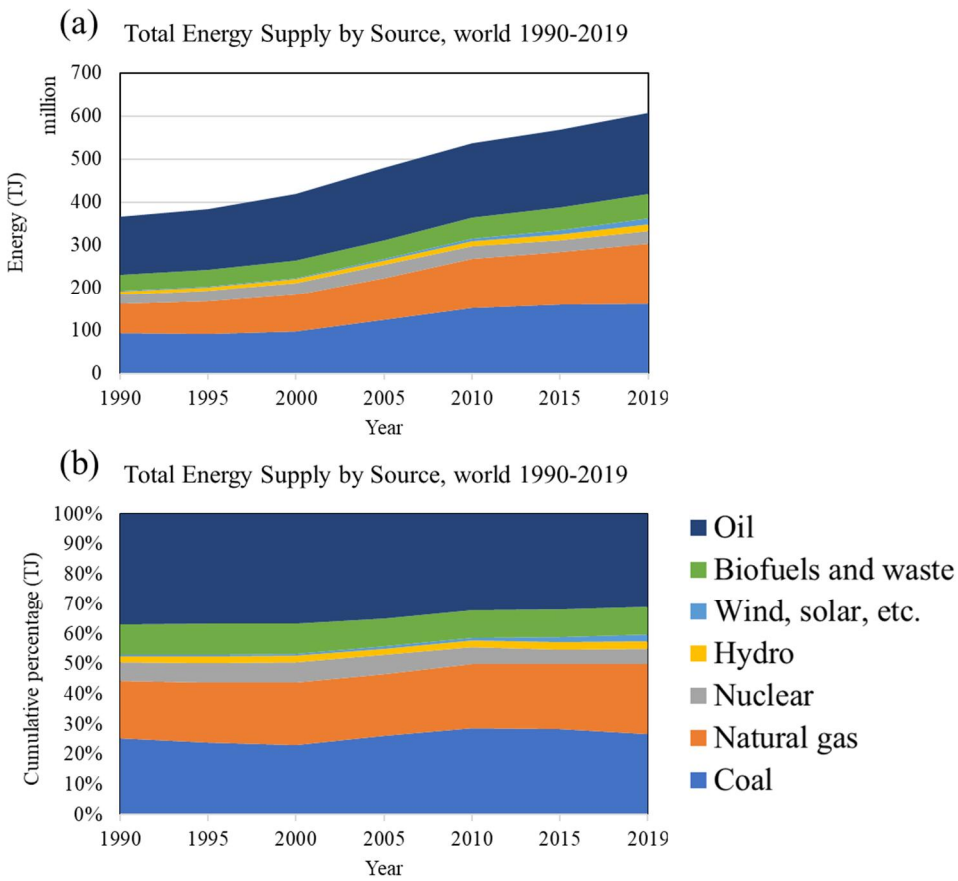

Figure 1.1 Total energy supply (TES) by source in the world 1990-2019 [1]

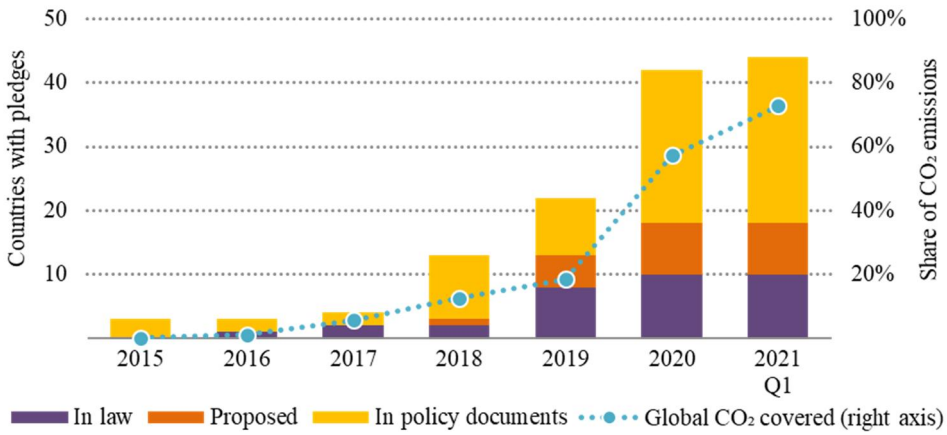

Figure 1.2 The number of national net zero pledges and share of global CO_2 emissions covered [3]

Therefore, recent advancements in combustion technology have been primarily driven by environmental concerns while maintaining combustion systems' efficiency and output power. As a solution to alleviate NO_x production, it is known that the production of NO_x is effectively reduced by lowering the combustion temperature. For instance, a rich-quench-lean (RQL) combustor serially combines fuel-rich and fuel-lean combustion stages, enabling low-temperature but high-power combustor operation [4, 5], and a flue gas recirculation (FGR) system recirculates a portion of high-temperature combustion products for sustaining low fuel-concentration combustion, which reduces the peak combustion temperature [6].

Alternatively, high-pressure combustion enables high-efficiency and high-power output engine operation, which leads to the reduction of pollutants and carbon dioxide emissions per unit of power output [7]. Recent gas turbines operate at above

supercritical pressures of carbon dioxide and water, which are the major combustion product species. For instance, a high-efficiency combustor was operated at 300 bar, combined with a carbon capture and storage (CCS) system to minimize CO_2 emissions [8, 9]. Supercritical fluids have the characteristics of low viscosity and high diffusivity. These characteristics reduce pressure loss and promote mixing, thereby increasing combustion efficiency and reducing pollutant emissions [10].

There are challenges in operating these environment-driven technologies optimally since sophisticated control is required. For example, minimizing NO emissions requires low-temperature flame conditions in which CO emissions increase. Also, combustion at low temperatures suffers from lean-flame instability. On the other hand, when the combustion pressure is high, the rate of heat transfer to the wall increases, and the temperature of the exhaust gas rises due to the combustion heat; therefore, the risk of premature failure of turbine blades exists. To prevent combustion failure due to flame instability and high temperatures, it is essential to monitor and control gas properties at the flame location, e.g., local fuel/diluent concentration and combustion temperature, since these properties determine combustion temperature, flame stability, pollutant generation, and failure.

Optical measurement methods, such as flame emission spectroscopy (FES), have been proposed to monitor gas properties in the combustion reaction zone [11-19]. FES, which utilizes instantaneous flame emission, is one candidate solution that can accurately measure gas properties in real-time. This is because FES measures gas

properties without disturbing the flow of the combustors and uses only photon detection systems. Given the high sampling rate (up to 10MHz [20]) of recently developed high-speed cameras, FES has the potential to achieve high temporal resolution. When measuring rapidly evolving combustion environments, a high sampling rate is desirable given that the sampling rate of the detection system should match the characteristic time scale of the flame. For example, the frequencies of large-scale eddies and precessing vortex cores of swirl flames are several kilohertz (kHz) [21-23]. Furthermore, the typical integral time scale and Kolmogorov scale of flames are tens and hundreds of kHz, respectively [24]. Also, FES utilizes a single optical access without an auxiliary light source, which is preferable in practical combustors.

In previous FES studies, it has been known that spontaneous emissions are generated from excited intermediate and product species during drastic chemical reactions in flame. Some characteristic local spectral features, e.g., atomic emission line strength and width, molecular emission band strength, broadband spectrum profiles, etc., are highly sensitive to gas properties. However, predicting gas properties directly from the emission spectra is challenging. This is because complete modeling of the chemical reaction pathway to analyze light emission from radical and molecular bands is demanding. Variations in gas properties such as pressure and concentration and species of fuel and diluent affect the chemical paths, resulting in the change of the dominant features of the emission spectra. Accordingly,

in previous studies, calibration experiments were conducted to provide a calibration function between the flame emission spectra captured under various flame conditions and the corresponding accurately measured properties. The calibration function is based on the monotonic correlation between a local spectral feature and a gas property, which provides a property indicator for calibrating measurements. Especially, the band intensity profiles generated by the excited radical or product species are used to predict fuel-air ratio (ϕ) [11-14, 25], combustion temperature (T) [15], pressure (P) [16, 17], species concentration (χ) [18], and heat release rate [19].

There are two issues with applying FES to monitor the aforementioned advanced environment-friendly combustion technologies. Firstly, variations in gas properties are interconnected and affect the chemical pathway, leading to changes in the emission spectrum. Specifically, depending on the components of fuel and oxidizer, as well as ambient pressure and temperature, the dominant emission lines become stronger or weaker or even vanish, which requires modification of the calibration indicator. Therefore, to calibrate various parameters, such as ϕ, diluent concentration, and temperature simultaneously, it is necessary to select a spectrum interval in which lines do not overlap and strongly appear to have a high signal-to-noise ratio (SNR) under all flame conditions. However, it is tedious and difficult to determine calibration parameters that work well for the overall range of combustion conditions. For example, increased combustor pressure suppresses the light emission of excited molecules resulting from the collisional quenching process, causing broadband

continuum emission rides over the emission bands. Consequently, spectrum analyses for quantitative property measurements become more difficult in advanced environment-friendly combustion technology.

Secondly, the shorter exposure time to achieve fast-time resolution of FES produces a lower SNR of spectral signals, with its consequent degradation of accuracy and precision. FES utilizes instantaneous combustion chemiluminescence spectra for estimating gas properties, and the sampling rate and exposure time for capturing the chemiluminescence spectra determine the time resolution of FES. However, the SNR of a detector is typically proportional to the square root of the exposure time assuming negligible readout noise. This is a limitation of the fast time-resolved FES because calculating the intensity of emission lines corrupted by noise has a large deviation, and thereby predicting the gas properties in the target flame shows a large error. Furthermore, the distinct emission lines are overlapped by noise in low SNR of signal and could disappear even if the noise floor is higher than the intensity of the emission lines, which makes it impossible to predict target properties. As a result, instantaneous control using FES is more difficult when a high acquisition rate measurement of quantitative properties is required.

This dissertation proposes a novel framework for FES to overcome the limitations of the traditional FES method. The proposed framework provides fast time-resolved and high accuracy combustion diagnostics by combining the data-driven calibration process and deep learning-based denoising method. The data-

driven calibration process is based on a reduced order model (ROM) employing proper orthogonal decomposition (POD) to reduce the dimensionality of spectral signals and the Kriging method to correlate the entire emission spectrum profile. Furthermore, the state-of-the-art deep learning-based denoising method is tuned for denoising and reconstructing low SNR flame emission spectra by employing novel neural network architecture and loss function. Consequently, the integration of deep learning-based denoising and the POD/Kriging method improves the accuracy of FES using low-SNR flame emission spectra with a short exposure time as inputs.

1.2 Previous studies

1.2.1 Mechanism of flame emission

Flame emission including information about the properties of the target flame comes from two mechanisms: 1) thermal radiation and 2) chemiluminescence. Every physical body spontaneously and continuously emits thermal radiation. Thermal radiation can be approximated by black-body radiation, which is thermal radiation from an idealized opaque non-reflective body in thermal equilibrium. Black-body radiation follows the Stefan-Boltzmann law, which states that the total radiant heat energy of thermal radiation is proportional only to the fourth power of the absolute temperature.

$$E = \sigma T^4 \tag{1.1}$$

where E, σ, and T stand for the radiant thermal energy from a unit area per unit time, Stefan-Boltzmann constant, and absolute temperature, respectively. The spectrum of the black-body radiation curve is continuous over a wide range of wavelengths. Planck's radiation law describes the relationship between temperature and energy spectral density.

$$B(\nu, T) = \frac{2h\nu^3}{c^2} \frac{1}{\exp\left(\frac{h\nu}{kT}\right) - 1} \tag{1.2}$$

where B, ν, T, h, c, and k are respectively the spectral radiance, emission frequency, absolute temperature, Planck constant, speed of light, and Boltzmann constant, respectively. Figure 1.3 presents the spectral radiance of blackbody radiation at varying temperatures. The wavelength of the spectral peak gets shorter and the total area also increases as the absolute temperature rises. In the flame under fuel-rich conditions, soot is formed, which causes black-body continuum radiation, depending on the flame temperature [26]. Therefore, spectral pyrometry can measure the temperature of the reacting gas flow by collecting radiation from soot and coal particles [27, 28].

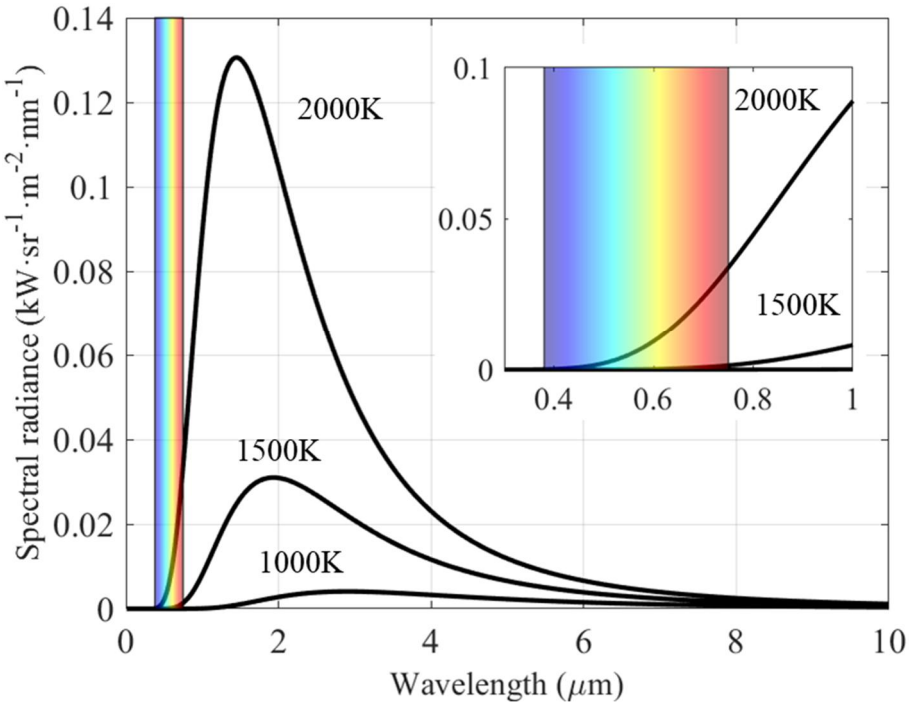

Figure 1.3 Spectral radiance of black-body radiation

Chemiluminescence, the spontaneous emission of light resulting from chemical reactions, is another primary mechanism of flame emission. Especially, hydrocarbon flames are characterized by their visible and ultraviolet wavelength ranges. The band structures of OH*, CH*, C_2*, and CO_2* are distinct from 250nm to 600nm wavelength; the asterisk symbol (*) denotes the excitation state of an atom or molecule. The reaction zone appears blue by spectral emission bands of excited CH radicals with an excess of air, and the reaction zone turns blue-green under fuel-rich conditions due to C_2 radicals. OH radicals are prominent characteristic features, and CO_2* contributes broad range continuum emission overlapping other spectral band

features. Also, to a lesser degree, continuous emission comes from HCO*, and CH_2O* [25, 29, 30].

The states of excited molecules from chemical reactions determine the structure of the bands and lines of flame emission [31]. Specifically, excited diatomic molecules emit photons as they transition from the upper rotational, vibrational, and electronic energy state to the lower rotational, vibrational energy, and electronic state. The wavelength of light emission is determined by the energy gap between the upper and lower states. The rovibrational energy state follows the selection rules that the quantum number changes only by 1 in transition according to quantum mechanical restrictions on the allowable changes. Therefore, the transition in the rovibrational energy state leads to branches and bands which are the groups of the line spectra. Furthermore, the electronic transitions occur between different potential energy wells, which is a higher energy gap, and a group of vibrational bands in the same electronic transition comprises an electronic system. In the following, the emission systems from the excited molecules in the combustion process and the chemical reactions that produce the excited molecules are introduced. Two numbers in parentheses with a comma mean the oscillation quantum numbers of the upper state and the lower state in turn. Two OH* bands are dominant in the UV region (280 – 315 nm). OH* (1, 0) is at 281.1 nm and OH* (0, 0) appears prominently at 306.4 nm, which are produced by the reactions H + O (+ M) → OH* (+ M) (M is the third body molecule), and CH + O_2 → OH* + CO [32]. In addition, CH* (0, 0) is at 431.4

nm and CH*(2, 2) is at 432.3 nm, which are mainly formed from $C_2 + OH \rightarrow CH^* + CO$, $C_2H + O \rightarrow CH^* + CO$, and $C_2H + O_2 \rightarrow CH^* + CO_2$ [33]. Three C_2 swan bands (1, 0) (0, 0) (0, 1) are located at 473, 513, and 563 nm respectively, which are from $CH_2 + C \rightarrow C_2^* + H_2$, and $C_3 + O \rightarrow C_2^* + CO$ [34]. The CO_2^* emission is generated by the reaction from $CO + O (+ M) \rightarrow CO_2^* (+ M)$ [18].

The intensity of a molecular band and broadband is proportional to the concentration of the excited species. The reaction and emission intensity equation are as follows [14, 33].

$$X^* \rightarrow X + \hbar\nu \tag{1.3}$$

$$I_X^* = A[X^*] \tag{1.4}$$

where X stands for the radical species including OH, CH, and C_2, h is the Planck constant and υ is the frequency of chemiluminescence, I is the photon emission rate, and A is the Einstein coefficient for spontaneous emission of transition. The concentrations of the radical species are very small because of low production rates and rapid removal by fast quenching rates [33]. Therefore, the radicals can be assumed to be in quasi-steady condition, which means that the concentrations of excited radicals are determined by the production rate and quenching rate. Therefore, the lines or broadband intensities of radicals can be physically interpreted as the

balance between the production rate and quenching rate. As a result, if the formation reaction and their rates of excited radicals are known, the intensity of chemiluminescence can be simulated. For example, as shown in Figure 1.4, assuming the formation reaction of CH* is only governed by $C_2 + OH \rightarrow CH^* + CO$, $C_2H + O \rightarrow CH^* + CO$, and $C_2H + O_2 \rightarrow CH^* + CO_2$ and the reaction rate constants are k_1, k_2, and k_3 for the corresponding reactions. In addition, the quenching rate constant for CH* by species j is $k_{Q,j}$, A is the Einstein coefficient for CH* transition. The photon emission rate (i_{CH^*}) can be simulated as follows.

$$[CH^*] = \frac{k_1[C_2][OH] + k_2[C_2H][O] + k_3[C_2H][O_2]}{\sum k_{Q,j}[M_j] + A} \tag{1.5}$$

$$i_{CH^*} = A[CH^*] \tag{1.6}$$

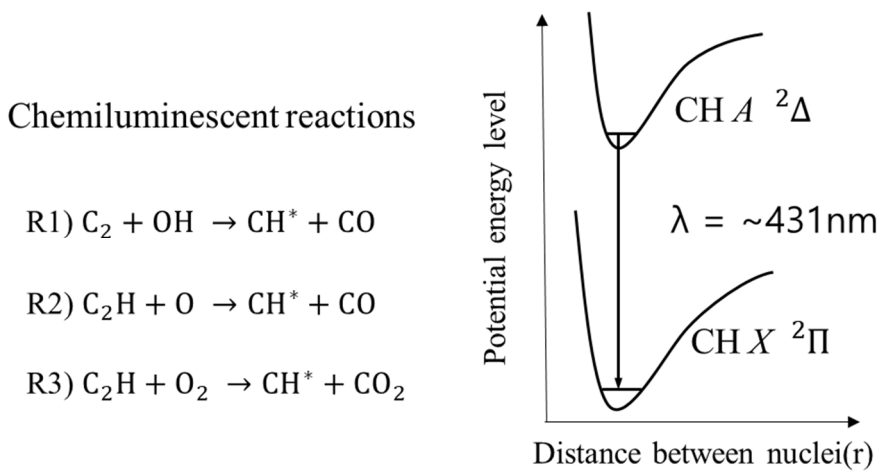

Figure 1.4 Chemiluminescent reaction path and light emission process of CH*

The spectral line shapes are determined by broadening mechanisms such as natural broadening, collisional (pressure) broadening, Doppler broadening, stark broadening, and instrumental broadening [31]. Primary sources of flame emission broadening include collisional broadening, Doppler broadening, and instrumental broadening. Collisional broadening occurs due to changes in the transition energy gap of excited molecules resulting from interaction during molecular collisions. Collisional broadening is a function of pressure and molar concentration and the shape follows the Lorentzian distribution. Doppler broadening is caused by the Doppler shift resulting from the random velocity distribution of molecules. Given the Maxwell-Boltzmann distribution law, the random velocity distribution is a function of temperature and molecular mass. Therefore, Doppler broadening is determined by temperature and molecular mass and the line shape is a Gaussian function. Instrument broadening can result from how a measurement is conducted, e.g., the resolution of a spectrometer.

As a result, characteristics of the intensity and spectral shape of distinct radical emission band is highly sensitive to the properties such as temperature, pressure, and the species and concentration of unburned gas. Figure 1.5 shows the spectrum measured at the equivalence ratio 0.8 and 1.1 of methane flame by changing the diluent gas with N_2 and CO_2 in the oxidizer. As mentioned, OH* appeared prominently in all of the flame conditions, and CH* and C_2* appeared in the rich flame. With CO_2-enriched conditions, the broadband background emission gets more

dominant, and OH*, CH*, and C_2* were weaker than the spectrum of N_2-diluted flame even in the rich region. This is because the concentrations of the intermediates decrease by changes in chemical reaction paths which are sensitive to the species and concentration of diluent [35]. The chemiluminescence in this example is highly dependent on gas properties such as species and concentration of diluent, equivalence ratio, flame temperature, and ambient pressure.

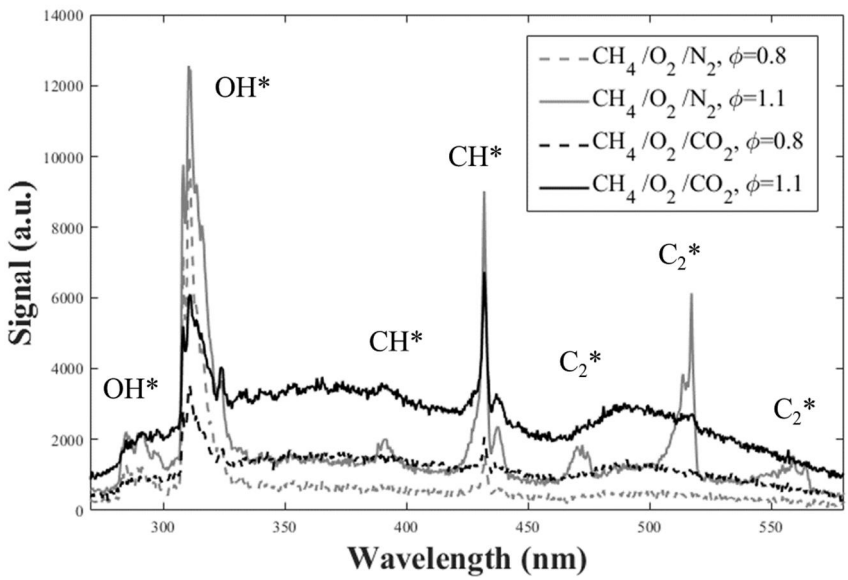

Figure 1.5 Chemiluminescence spectra of lean (equivalence ratio ≡ ϕ = 0.8) and rich (ϕ = 1.1) methane-air flames diluted by CO_2 or N_2

1.2.2 Calibration process of flame emission spectroscopy (FES)

The most common technique for calibrating spectra to the gas property in FES is to derive a monotonic correlation between a local spectral feature and a target gas property while all other properties are constant. For example, Higgins proposed that the intensity of the OH* emission band can indicate the equivalency ratio of the gas mixture while the flow rate and pressure of the air (or mixture), which also affect the emission intensity, are kept constant [11]. Likewise, it is known that the characteristic variation of some regional spectral features like emission bands of CH*, C_2*, CN*, NH*, and CO_2* and their intensity ratios (e.g., OH*/CH*, CH*/C_2* and OH*/C_2*) have been studied in numerous prior research to measure gas properties, such as the equivalence ratio [12-14, 17, 18, 36-39], pressure [17, 37], species concentration [18, 38, 39], and heat release rate [19]. However, these manually selected local spectral features are unable to reveal all the varying gas properties because the interconnected nature of the gas properties makes variations in flame emission non-monotonic. Furthermore, FES measurements are made more difficult due to the use of advanced environmentally-friendly combustion technologies. For example, a high-pressure environment causes the local spectra to be indistinct because it quenches the excited species while enhancing CO2 emission bands.

Data-driven calibration methods, e.g. partial least-squares regression (PLS-R), artificial neural networks (ANN), and POD / Kriging have been used to overcome the drawbacks of the manually selected one-to-one calibration methods [40-44].

Tripathi et al. [40, 41] demonstrated that PLS-R based on the PLS method and multiple linear regression (MLR) offers improved performance on ϕ-predictions in a wider fuel concentration range compared to the accuracy of calibrated OH*/CH* because of the low-intensity spectral peak of CH* in fuel-lean flame conditions. However, only ϕ was calibrated and predicted at atmospheric pressure without sensitivity analyses. Paulo et al. [42] utilized the same method, PLS-R, to measure the octane number in gasoline fuels from flame emission. Also, only the octane number was calibrated and predicted. In addition, Ballester et al. [43] used an ANN to calibrate pollutant concentrations (CO and NO_x) and chemiluminescence spectra. ANN worked well as a non-linear regression tool from spectra to pollutant concentration, but ANN often requires a lot of data to train the neural network and also is a "black box" because interpreting how all the neurons work together to get the final output is not clear to the user. Moreover, Yoon et al. proposed that a calibration process utilizing a ROM based on POD extracts spectral features highly sensitive to diluent concentration, equivalence ratio, and temperature to accurately predict the properties from spectral signals [44].

1.2.3 Deep learning-based denoising

In the raw spectral signals, noise from the image sensors, circuits of the digital camera, and in-camera processing pipelines causes unwanted modifications to signals. In general, noise does not include useful information and is rather random.

Hence, in most cases, noise is desirable to be reduced while recovering the original signal, i.e., a high SNR signal. In signal processing, filters such as a Gaussian, median, low-pass, and Savitzky-Golay filter are commonly used to selectively attenuate noise and to recover the original signal. For example, a Gaussian smoothing filter can enhance SNR by selectively attenuating high-frequency noise [45]. However, these filters will inevitably remove information in the high-frequency range including peaks and band structures which are important indicators of the gas properties in FES, resulting in inaccurate measurements as shown in Figure 1.6.

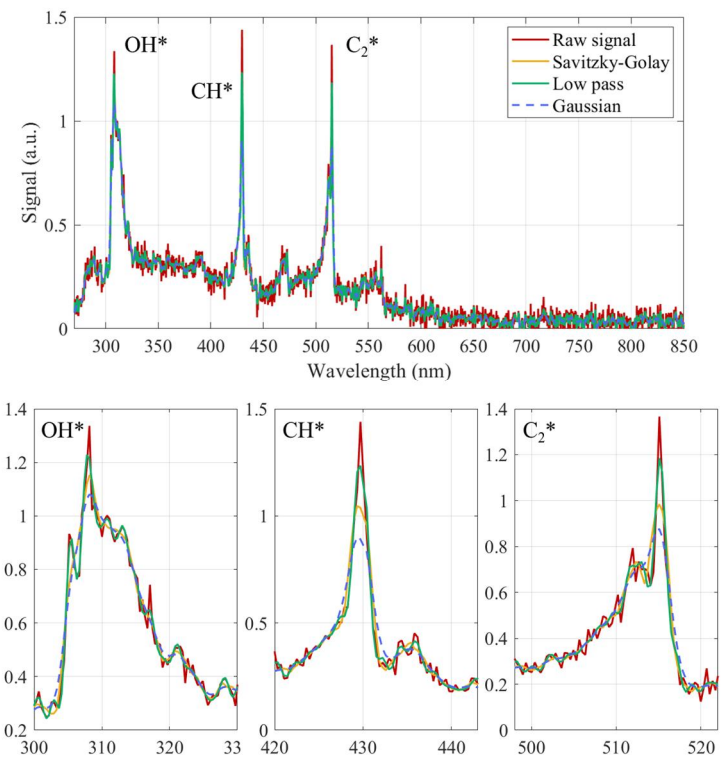

Figure 1.6 Comparison of spectral signals processed with various filters

The noise removal ability of state-of-the-art machine learning techniques based on deep layers has achieved remarkable performance for digital image denoising. The recent development of neural network architecture and regularization methods such as Rectified Linear Units (ReLU) [46], Batch Normalization (BN) [47], and residual learning [48] helps to overcome the drawbacks of the deep architecture, e.g. vanishing gradients, the high computational cost of activation functions such as sigmoid and hyperbolic tangent, and the hardware platform [49]. The deep neural network architectures for CNN, e.g. AlexNet (2012) [46], VGG (2014) [50], and GoogLeNet (2015) [51] were successfully applied to classify the image dataset, which utilizes multiple kernels (filters). These multiple kernels explicitly exploit local features and impose translation invariance, which enables CNN to take advantage of the spatial features in the image dataset. In this context, deep CNNs have been employed in restoring and denoising images since 2015 and have performed well on a wide range of denoising tasks [52].

Recently, convolutional neural networks (CNN) have been most widely applied to restore and denoise images [49, 53-60]. The denoising CNN (DnCNN) improved denoising performance and increased training speed by using plain CNN architecture combining the convolutional layer, BN, and ReLU without pooling and skipping connections, and residual learning as regularizing methods [54]. The fast and flexible denoising CNN (FFDNet) reduced running time and memory usage for the denoising task and the noise level range by using down-sampled sub-images and an explicit

noise level map without residual learning [55]. The down-sampled sub-images in FFDNet effectively increase the receptive field (RF) which is the number of input pixels involved to produce one output pixel, resulting in exploiting global context information. However, these methods are based on data augmentation by adding noise so noise modeling, i.e. probability distribution and the noise level, is required, which is challenging to apply the methods to real-world noisy images. In training the denoising CNN structure, pairing real noisy and high-quality clean datasets without using noise modeling can handle real noise and perform better than conventional noise modeling [56, 57].

The use of noisy data to train the denoising ability in studies such as Noise2Noise, Noise2Self, and Noise2Void was presented to avoid noise modeling and to apply the denoising method where high-quality data is not available [58-60]. Noise2Noise needs independent pairs of noisy data but this requirement is not necessary for Noise2Self and Noise2Void due to being trained by self-supervision. This can be achieved by assuming the noise is conditional independent pixel by pixel and the expectation of noise is zero. These denoising methods perform well when acquiring clean data is limited, but they suffer performance degradation when the noise violates assumptions, e.g., structured noise. In addition, when dealing with data with extremely high noise levels, the overall performance is diminished compared to that of the methods supervised by clean data [60].

The state-of-the-art of these machine learning approaches mainly focuses on

general images rather than quantitative scientific image analyses [49, 53-60]. The adaptation of machine learning-based denoising to spectroscopic analyses for optical diagnosis is promising for the measurement of various quantities. Recently, several studies of the denoising method on spectroscopic analyses have been investigated, including Rayleigh and Raman scattering spectroscopy, laser absorption spectroscopy, electron spectroscopy, and angle-resolved photoemission spectroscopy [61-64]. Machine learning techniques have been demonstrated to increase the accuracy of quantitative measurements of target properties. It is also notable that CNN was adopted in optical combustion diagnosis as a nonlinear regression method. Barwey et al. carried out mapping a series of OH planar laser-induced fluorescence images into three component planar velocity fields with the combination of CNN structures [65]. Rodriguez et al. presented the CNN method for estimating soot volume fraction distribution from integrated light extinction by soot particles, resulting in accurate measurements that are not sensitive to random noise and regularization parameters [66]. Wan et al. proposed a gradient-free regime identification approach to construct a combustion regime based on CNN. Yoon et al. demonstrated that CNN architecture with a wide receptive field and with a modified loss function can significantly reduce noise in spectral signals and achieve fast time resolution of FES [67].

1.3 Outline of the Dissertation

The dissertation includes studies on the characteristics of flame emission, the development of the FES method that provides accurate and fast time-resolved measurements of multi-properties for combustion diagnostics, and its application to flame emission in high-pressure environments. Following is an outline of the remaining chapters of this dissertation.

Chapter 2 presents experimental results investigating the characteristics of flame emission from high-pressure methane-air combustion. The experimental setup for the combustor and detection system is described in this chapter. Furthermore, the variations of prominent molecular emission bands are investigated as indicators of gas properties following conventional calibration methods.

Chapter 3 demonstrates the development of a data-driven calibration process using ROM. The strategy of ROM is composed of POD as a dimension reduction method and the Kriging model as a regression model. Moreover, to validate and analyze the ROM, cross-validation and global sensitivity analysis (GSA) are introduced, and the result of the method in the calibration process is discussed.

Chapter 4 describes the development of deep learning-based denoising for flame emission spectra. A deep learning architecture is proposed that combines reversible down- and up-sampling (DU) operators with plain CNN. The training of the neural network is regularized by the loss function that consists of the mean square error

(MSE) and squared L2 norm of the POD coefficients. This chapter discusses how the proposed methodologies efficiently and accurately preserve information in flame spectra using a deep learning-based denoiser.

Chapter 5 proposes a framework for fast time-resolved and high-accuracy FES utilizing the data-driven calibration process and the deep learning-based denoising technique. The framework is applied to the flame emission from high-pressure methane-air combustion. Additionally, this chapter discusses the effect of exposure time on the prediction accuracy of measurements.

Chapter 6 presents the conclusions of the research and suggests further research.

1.4 Contributions

The main contribution of this dissertation is the development of a data-driven calibration process and deep learning-based denoising method to achieve fast time-resolved and high-accuracy FES. Moreover, the performance of the proposed method of FES has been validated using actual flame spectra from the combustion experiments in the high-pressure combustion environment. Below are the detailed contributions.

1. This dissertation proposes a novel data-driven calibration process utilizing ROM including POD and a Kriging model. In contrast to the traditional one-to-one calibration method of FES using distinctive local spectral features, the proposed data-driven calibration process results in accurate measurements and can be applied to multiple properties in high-pressure conditions. The POD extracts feature at a wide range of wavelengths and regression using the Kriging model correlates the POD coefficients with the target gas properties. In Chapter 3, the details are discussed.

2. This dissertation proposes a novel denoising deep learning architecture and loss function designed specifically for flame emission spectra. Using the proposed method, it is possible to obtain high temporal resolution measurements of gas properties using short exposure time signals. A neural network using a DU operator and plain CNN effectively expands the receptive

field and regularizes training by the squared L2 norm of the POD coefficients that include features in a broad wavelength range. This method effectively overcomes the problem of measuring gas properties with low SNR signals by enhancing SNR utilizing both pixel-wise global and local contextual information. In Chapter 4, the details are discussed.

3. This dissertation proposes a framework for FES combining the data-driven calibration process and deep learning-based denoising method to achieve fast time-resolved and high-accuracy combustion diagnostics. The framework is applied to actual flame spectra from high-pressure combustion for demonstration, and successfully predicts gas properties with low SNR signals that represent FES from unstable and unsteady flames where fast temporal resolution is desirable. Furthermore, the effect of exposure time on the accuracy of gas property prediction including noise analysis of the spectral signal is discussed. In Chapter 5, the details are discussed.

4. In summary, the proposed framework has a significant contribution in that it is a novel concept that addresses the limitations of conventional FES. This dissertation shows that the proposed framework remarkably improves the accuracy, precision, and temporal resolution of FES to measure multiple gas properties by combining the advantages of each method.

CHAPTER 2. EXPERIMENTAL RESULT OF FLAME EMISSION

2.1 Flame emission measurement

Spectral signals from high-pressure methane-air combustion are investigated to understand the characteristics of flame emission and calibrate gas properties of flame conditions. A high-pressure methane-air flame is supposed to be a laboratory-scale combustor of a modern gas turbine. Methane, which is the main component of natural gas, has significant environmental advantages over fossil fuels such as coal and gasoline. Since they produce more heat and energy per unit of mass, they cause far less smog and air pollution, as well as carbon dioxide. Moreover, if methane is produced from non-fossil sources, e.g., food industries such as rice and corn, landfills, and biomass burning, the combustion of methane can be more environmentally-friendly [68].

2.1.1 Experimental setup

A steady state methane-air flame with equivalence ratio, ϕ ($= \frac{\chi_{CH_4}/\chi_{O_2}}{(\chi_{CH_4}/\chi_{O_2})_{stoic}}$) of 0.8 – 1.2 and pressure, P of 1 – 10 bar is produced by a custom-built McKenna burner in a high-pressure chamber with four separate viewports. The experimental setup for operating a high-pressure burner consists of three systems; flow control, burner, and

laser ignition system, as shown in Figure 2.1. The flow control system including a compressor, dehumidifier, buffer tank, and mass flow bench regulates and maintains constant mass flow rates of fuel and methane to be provided to the burner. Thermal-type mass flow controllers (Bronkhorst, EL-FLOW, F-211AV for methane, and F-211AC & F-002AV for air) accurately regulate the fuel and air flows to control ϕ. The burner system consists of a high-pressure chamber, flat flame burner, heat exchanger, and back pressure regulator, which is designed to sustain a high-pressure flame environment. The air and fuel from the flow control system are fully mixed before being fed to the burner, and the burner composed of a low porosity sintered brass plate (porosity = 0.365 and diameter = 60.5 mm) provides a uniform flow field above the exit plane. The flow rates of air and fuel are controlled by considering the corresponding ϕ and laminar flame speed calculated by ANSYS Chemkin-Pro using GRI-Mech 3.0 under given flame conditions. The flow speed on the exit plane was kept higher (2–6%) than the laminar flame speed to sustain and stabilize the flat flame about 1 mm above the outlet plane. The temperature of unburned premixed gas is precisely controlled at 298K by water cooling with a cooling coil in the metal plate, presumably the same as the reactant temperature. The speed of air shielding from the outer sintered brass ring is matched with the speed of the burned gas after considering thermal expansion, and this shielding stabilizes the outward edge of the flame. The air shielding also helps to keep the total fuel concentration in the chamber below the lean flammability limit for safety reasons. A back pressure regulator (Equilibar, GSD4SNT5-NSBP300T300I8KK) precisely controls the ambient

pressure in the high-pressure chamber by opening up the right amount to maintain the appropriate pressure, and a static pressure sensor (TIVAL, TST-10.0, ± 0.25% of the full scale (40 bar)) measures the pressure. The back pressure regulator is made up of a metal body and diaphragm whose operating temperature is up to 300°C, and therefore, the temperature of burned gas is lowered to under 300°C by using a heat exchanger composed of brass tubes for passing the burned gas and a water tank for circulating cool water. The laser ignition system includes a high-power laser, mirror, and focusing lens. The second harmonic laser beam (wavelength = 532 nm) from Nd YAG laser (Spectra-physics, Quanta-Ray LAB150) is focused by a plano-convex lens (Thorlabs, LA1979-A, A-coated, focal length = 200 mm). The energy per pulse of the laser was about 100mJ and the pulse width was 6 ns which is enough to provide the spark to ignite the premixed gas.

The flame emission spectra are collected by a UV-camera lens (Nikon, UV-Nikkor, f = 105 mm) from the perpendicular plane of the flame front from an optical access on the high-pressure chamber. The collected emission appears as a flame image at the focusing location, and this image is placed at the entrance of an optical fiber (Ocean optics, QP600-2-SR-BX) that transmits light in the wavelength range 200 to 1100 nm. The other end of the fiber is directly connected to a portable spectrometer (Ocean optics USB 2000+, 600 grooves/mm grating for 0.5 nm spectral resolution), and the spectrum of flame emission is analyzed in a broad spectral range from 250 to 850 nm. The distances between the flame and the lens and between the lens and

fiber were 370 mm and 145 mm, respectively, which magnified the flame image by a factor of 0.4. Since the thickness of the flame is approximately 1 mm and the diameter of the fiber core is 500 μm, the entire image of the flame plane is fed through the fiber. 2 s exposure is sufficient to record high-SNR spectrum signals. To investigate the effect of exposure time on spectral signals and the accuracy of gas property prediction, various exposure (gate) times (0.05, 0.2, and 2 s) are used to acquire the spectra.

In summary, systems of mass flow control, burner, laser ignition, and optical diagnostics are built to operate a high-pressure flat flame burner precisely and collect a spectral dataset of the flame emission at given flame conditions as illustrated in Figure 2.2.

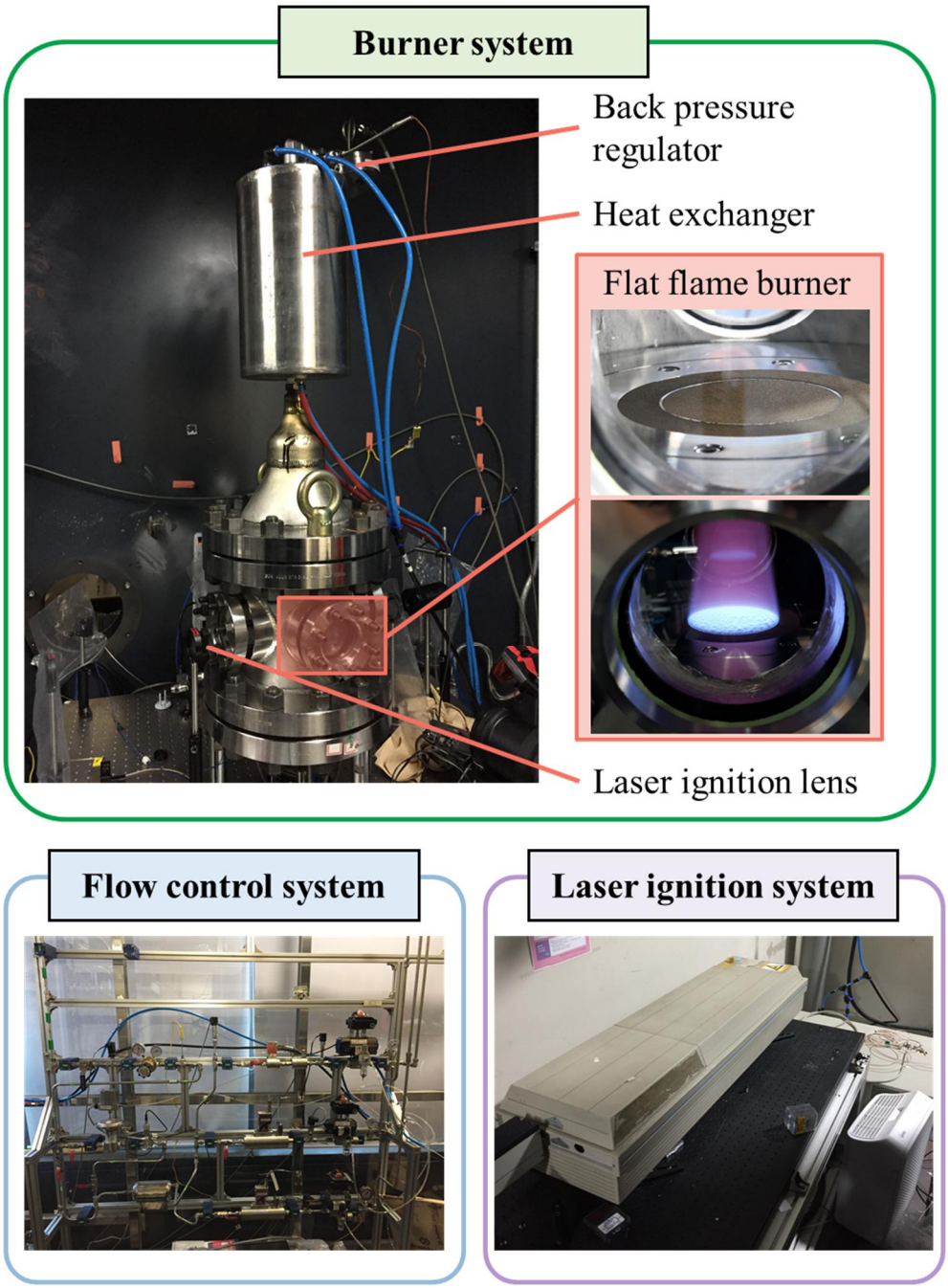

Figure 2.1 Experimental setup for high-pressure flat flame McKenna burner

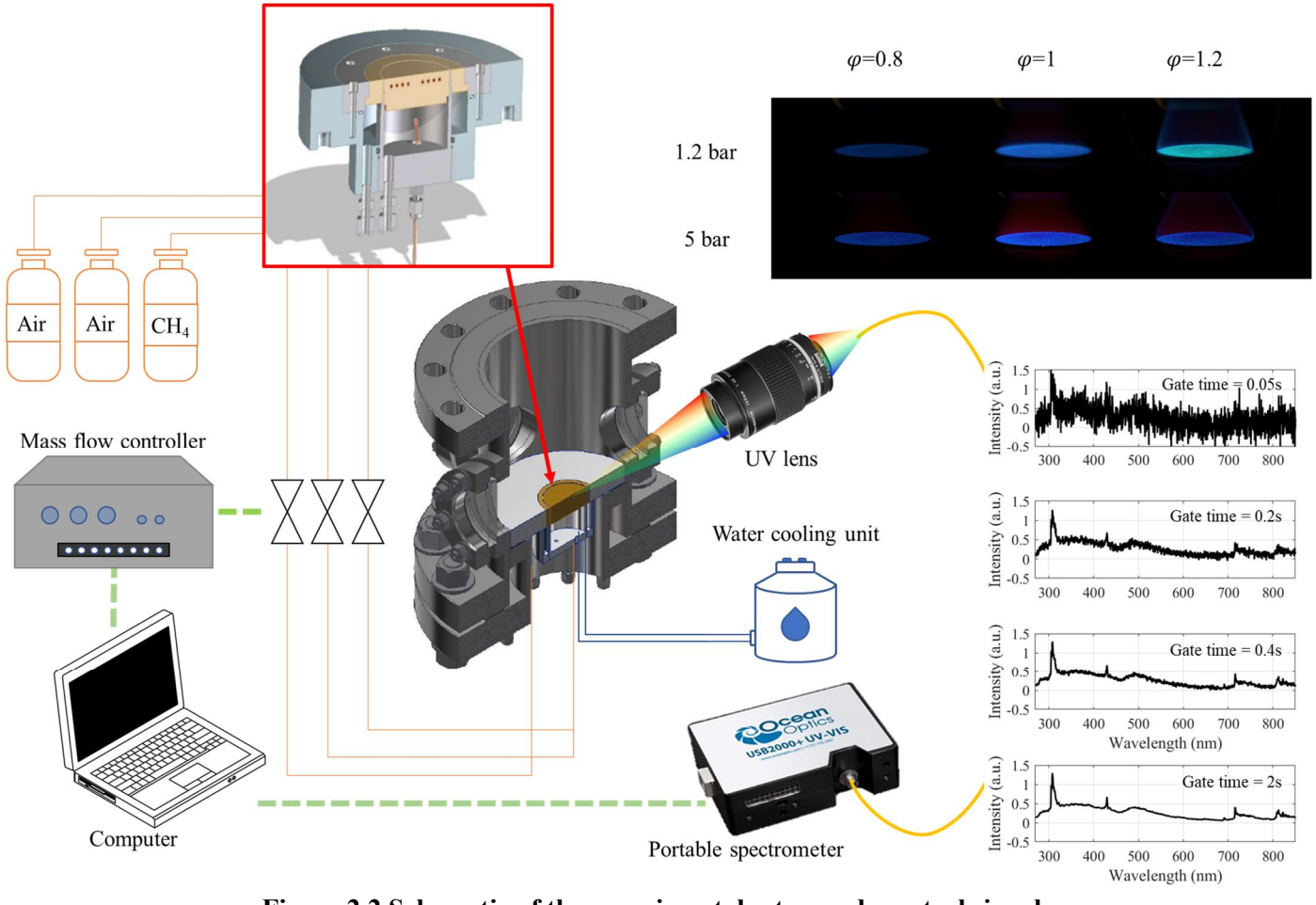

Figure 2.2 Schematic of the experimental setup and spectral signals

2.1.2 Uncertainty quantification of experimental measurement

The uncertainty of experimental measurements is estimated by evaluating component level uncertainty and its propagation to the target properties [69]. In this study, the uncertainty of the equivalence ratio is quantified by a linearly parameterized model assuming that each component is independent and the first derivative terms are dominant. For example, if the uncertainties of each flow controller are known, the uncertainty of the equivalence ratio can be estimated using the equation below (Eq. (2.1)).

$$\sigma_{\phi}^{2} = \left(\sigma_{\dot{m}_f} \frac{\partial \phi}{\partial \dot{m}_f}\right)^2 + \left(\sigma_{\dot{m}_a} \frac{\partial \phi}{\partial \sigma_{\dot{m}_a}}\right)^2 \tag{2.1}$$

where $\dot{m}_f$, and $\dot{m}_a$ are mass flow rate of air and fuel, and σ_{ϕ}, $\sigma_{\dot{m}_f}$, and $\sigma_{\dot{m}_a}$ indicate the uncertainty of each variable. The mass flows of fuel and air were regulated by thermal-type mass flow controllers (Bronkhorst, EL-FLOW, F-211AV for methane, and F-211AC & F-002AV for air). According to the technical specifications of Bronkhorst, the accuracy uncertainty of EL-FLOW select F-211AV is the sum of ± 0.5% of reading digit(s) and ± 0.1% of the full scale (20 slpm), and the accuracy uncertainty of EL-FLOW select F-211AC & F-002AV is the sum of ± 0.5% of reading digit(s) and ± 0.1% of the full scale (250 slpm). The estimated uncertainty of ϕ considering technical specification and propagation is between 0.89% and 1.68% and the numbers are listed in Table 2.1. In addition, the uncertainty of

pressure measurement in the combustion chamber was 0.1 bar estimated by the specification of a static pressure sensor, TIVAL TST-10.0, which has ± 0.25% of the full scale (40 bar) uncertainty.

Table 2.1 Estimated uncertainty of equivalence ratio

Unit: %	Equivalence ratio (ϕ)				
P (bar)	0.8	0.9	1.0	1.1	1.2
1.2	1.68	1.43	1.31	1.29	1.37
2	1.42	1.23	1.14	1.13	1.20
3	1.27	1.12	1.05	1.04	1.12
4	1.19	1.06	1.00	0.99	1.07
5	1.14	1.02	0.96	0.96	1.04
6	1.10	0.99	0.94	0.94	1.01
7	1.07	0.97	0.92	0.92	0.99
8	1.05	0.95	0.91	0.90	0.97
9	1.03	0.93	0.89	0.90	0.96
10	1.01	0.92	0.89	0.90	0.94

2.1.3 Noise analysis of spectral signal

The application of FES to monitor the rapidly evolving combustion environment requires the exposure time and sampling rate of the detection system to be matched with the characteristic time scale of the flame. For example, the time scale of large-scale eddies and precessing vortex core of swirl flames are several microseconds [21-23]. Furthermore, the integral time scale and Kolmogorov scale of flames are hundreds and tens of microseconds [24]. However, the short exposure time causes noise-corrupted signals as presented in Figure 2.3. To determine the correlation between the SNR and exposure time, the noise level of spectrum is quantitatively estimated by calculating the three primary noise sources of the charge-coupled device (CCD) sensor in the spectrometer: 1) photon noise, 2) dark noise, and 3) read noise [70]. 1) The photon noise is caused by the stochastic arrival of photons on the charge-coupled device (CCD). The number of photons that reach the CCD follows a Poisson distribution, and the square of the error is inversely proportional to this amount. 2) Dark noise is the spontaneously produced current even when no photons are incident on the CCD. It also follows the Poisson distribution and the square of the dark noise equals the number of dark electrons. 3) The readout noise is produced by the conversion of the charge-voltage and digitization processes and it depends on the sampling frequency and tends to rise as the sampling rate increases [71].

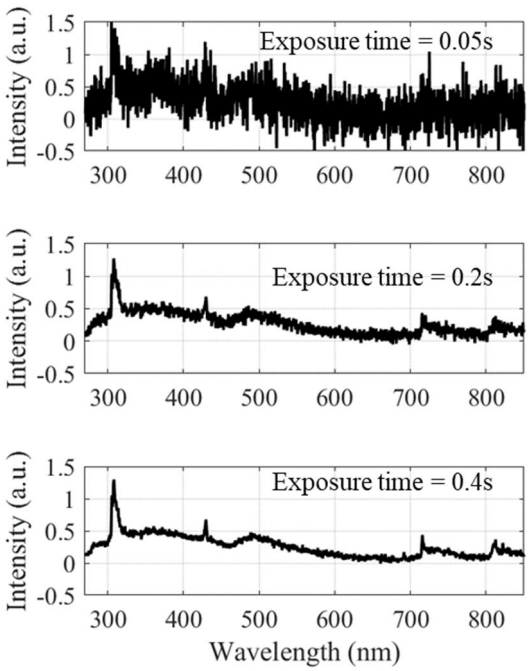

Figure 2.3 Typical chemiluminescence signals with three different exposure times (0.05, 0.2, and 0.4 s)

Both the photon noise and dark noise follow the Poisson distribution which can be approximated to the Normal distribution. This is because the central limit theorem is satisfied when the exposure time is long enough. As each noise source is independent, the total noise equals the root sum square of its components. As a result, the SNR of a spectrum signal can be estimated via the equation below, Eq. (2.2),

$$SNR = \frac{N_{electron}}{\sqrt{\sigma_{Photon}^2 + \sigma_{Dark}^2 + \sigma_{Read}^2}} = \frac{\phi_p \eta \tau}{\sqrt{\phi_p \eta \tau + I_{dark}\tau + N_R^2}} \qquad (2.2)$$

where, $N_{electron}$, σ_{Photon}, σ_{Dark}, σ_{Read}, ϕ_p, η, τ, I_{dark}, and N_R denote for the number of counted electrons, photon noise, dark noise, readout noise, photon flux

at the CCD, quantum efficiency, exposure time, dark current, and the number of thermal electrons, respectively. A monotonic decrease in SNR is predicted with reduced exposure time according to the estimation of SNR (Eq. (2.2)).

In this study, the spectrometer was Ocean optics USB 2000+, which utilizes a CCD image sensor (Sony, ILX551, 2048-pixel CCD Linear image sensor). According to a report about the comparison of line array sensors including ILX551B [72], the dark current slope fit at 25 °C is measured as 0.0363 digital count/ms and 0.011 mV/ms, and the root mean square of readout noise at 500kHz is measured as 2.1159 digital counts and 0.63mV. The SNRs of the OH* peak at 308 nm at P = 10 bar and ϕ = 1 are quantitatively evaluated and each noise component is converted to digital counts, mV, and electron, as listed in Table 2.2. The SNRs of the chemiluminescence signals monotonically decrease with decreasing exposure time; the average SNR of OH* at 308nm is 4.3, 14, and 22 for 0.05, 0.2, and 0.4 s exposure time, respectively.

Table 2.2 Noise analysis of OH* peak (308 nm) at P = 10 bar and ϕ = 1

	Exposure time (s)								
	0.05			0.2			0.4		
	e^-	DC	mV	e^-	DC	mV	e^-	DC	mV
Counted Signal	115	9.97	2.99	463	40.2	12.0	934	81.2	24.3
σ_{Photon}	10.7	0.93	0.28	21.5	1.87	0.56	30.6	2.66	0.80
σ_{Dark}	4.56	0.40	0.12	9.14	0.79	0.24	12.9	1.12	0.34
σ_{Read}	24.3	2.12	0.63	24.3	2.12	0.63	24.3	2.12	0.63
SNR	4.3			14			22		

2.2 Computational simulation of flame properties

Laminar flame speed and burned gas speed on the burner at the given condition, i.e., ϕ, P, and reactant temperature conditions need to be estimated to operate the high-pressure flat flame McKenna burner. Moreover, adiabatic flame temperature and pollutants such as CO and NOx are used as gas properties to be calibrated with spectral signals, as will be discussed in section 3.4.3. Therefore, modeling and simulating chemical reactions of the gas phase are carried out by ANSYS Chemkin-pro 2020 R1 with GRI-Mech 3.0. Computational simulation using GRI-Mech 3.0 is a detailed kinetic mechanism developed for methane-air flame and is validated by experimental data in high-pressure conditions up to 20 atm [73]. 1D laminar flame was assumed for the simulation and the grid parameters were 0.1 and 0.5 for adaptive grid control based on solution gradient and curvature respectively to obtain grid-independent results. The results of flame speed, adiabatic flame temperature, and the pollutant such as CO and NOx with varied ϕ and P are illustrated in Figure 2.4 and listed in table A.1 in Appendix A.

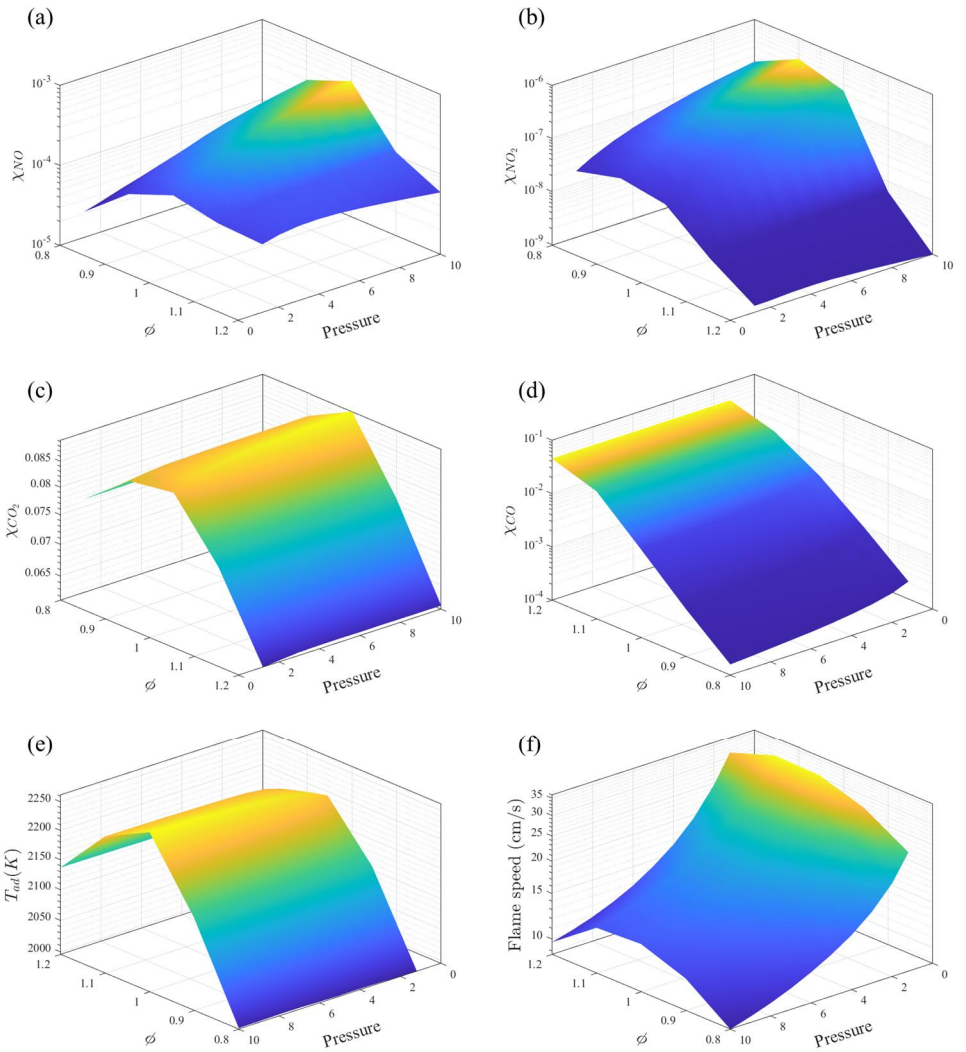

Note that the pressure axis of (d), (e), and (f) are reversed for better visibility.

Figure 2.4 Simulation result of flat flame using Chemkin-pro (a) χ_{NO}, (b) χ_{NO_2} (c) χ_{CO_2}, (d) χ_{CO}, (e) T_{ad}, and (f) Flame speed

2.3 Characteristics of flame emission

In this section, spectral signals with varying gas properties, ϕ and P, are presented, and the variations of the spectral signals are quantified by conventional indicators, e.g. the intensity and ratio of bands of each radical. The signals which are measured by an optical spectrometer, are 10 signal-averaged with 2 s exposure time to get high-SNR flame emissions, and are adjusted to account for the dark spectra that are acquired without flame. As presented in Figure 2.5, the spectral signals consist of peaks and bands overlapping with broadband features spontaneously emitted from excited radicals and molecules. The band structures of OH*, CH*, and C_2* are observed, which is consistent with previous experimentally measured results [12, 16]. In particular, OH* (1, 0) is at 281.1 nm, and OH* (0, 0) appears prominently at 306.4 nm. CH* (0, 0) is at 431.4 nm, and CH* (2, 2) is at 432.3 nm. In addition, three C_2 swan bands (1, 0), (0, 0), and (0, 1) are located at 473, 513, and 563 nm, respectively. The band emissions from H_2O* consist of the dominant feature in the range of 690 – 850 nm. Blackbody radiation is hardly observed in the signals because the production of soot and particles is limited because of the nature of the premixed methane-air flame. Each distinct radical band is also displayed in the zoomed plot as presented in Figure 2.5. It clearly shows that the emission from radicals related to carbon decreases with fuel-lean conditions, and the band intensities are reduced as ambient pressure increases by accelerated collisional quenching effects.

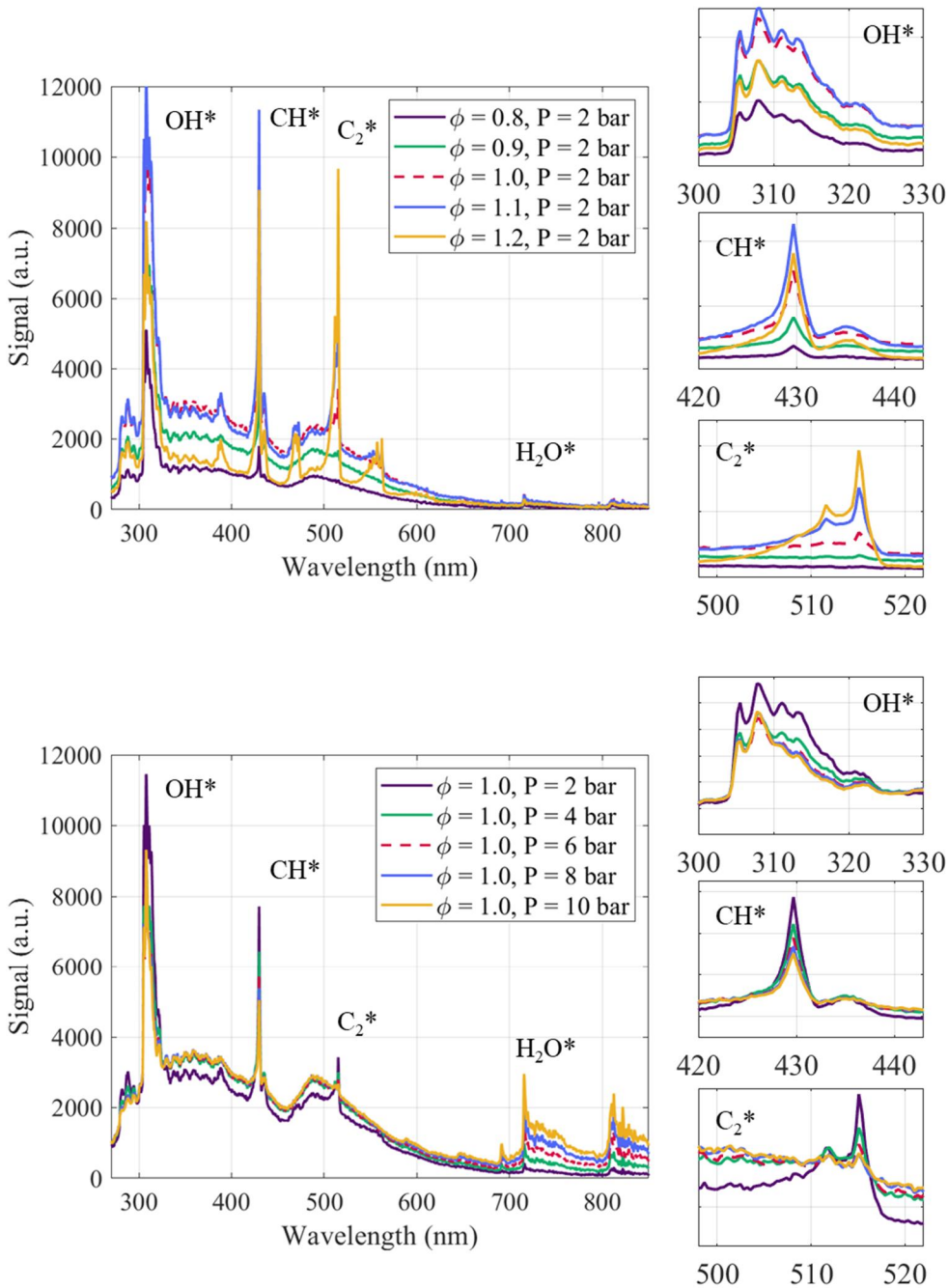

Figure 2.5 Spectral signals of methane-air flame with varying ϕ and P

Some dominant local features from radical emissions are selected for further analysis as presented in Figure 2.6 (a). As shown in the figure, the spectral signals are decomposed by the distinct features, i.e., OH* (306 – 338 nm), CH* (420 – 443 nm), and C_2* (498 – 522 nm), H_2O* (713 – 791 nm), and broadband (BB, 270 – 650 nm) mainly from CO_2*. To calculate the intensity of each band structure, broadband curve fitting is obtained by interpolating the data points avoiding distinct emission bands of radicals as shown in Figure 2.6 (b). The interpolation is constructed by the modified Akima function to avoid excessive local oscillation of the broadband signal [74].

The variations of spectral local features from radical emissions are presented in Figure 2.7. As P rises with fixed ϕ (Figure 2.7 (a), (c), and (e)), the emission bands of radicals (OH*, CH*, and C_2*) decrease because of collisional quenching, while the broadband increases and then is about constant at higher pressures. The trends in emission bands (OH*, CH*, and C_2*) show monotonic behavior in fuel-lean conditions ($\phi \leq 1$) but the trends change monotonically in fuel-rich ($\phi = 1.2$) and low-pressure conditions ($P < 2$) as shown in Figure 2.7 (e). Therefore, these variations can be used as indicators of pressure only under fuel-lean conditions, not fuel-rich conditions. Otherwise, in all equivalence ratio conditions, H_2O* increases linearly proportional to pressure so these monotonic changes in H_2O* can be calibrated to pressure. Figure 2.7 (b), (d), and (f) show the changes in emission intensity (OH*, CH*, C_2*, H_2O*, and BB) with fixed P. The OH* and CH* emission bands increase

until ϕ reaches unity because of increasing the flame temperature. Under fuel-rich conditions ($\phi > 1$), the radical emissions weaken with increasing ϕ while fuel concentration, which can be a source of carbon and hydrogen atoms, continues to rise. This is because the flame temperature decreases as ϕ increases above the stoichiometric ratio. However, the trend of band intensity changes with higher pressure so that the maximum values of OH* and CH* are closer to the stoichiometric ratio. This is because the pressure and equivalence ratio interconnect with flame temperature which affects the chemical reaction path of spontaneous emission. Otherwise, C_2* monotonically increases with the equivalence ratio, and thereby, the intensity of C_2* can be calibrated to the equivalence ratio in all pressure conditions.

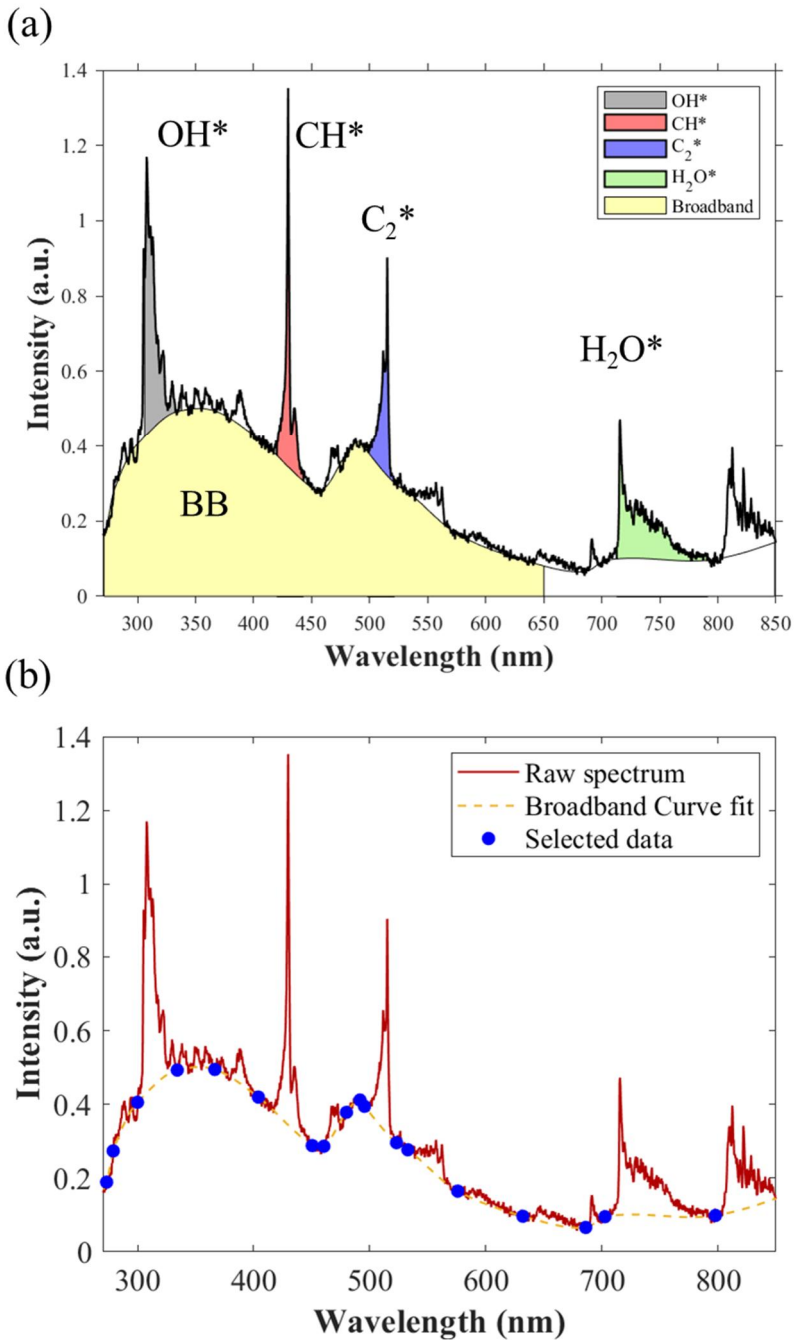

Figure 2.6 (a) Selected distinct local spectral features and (b) broadband curve fit to extract local features

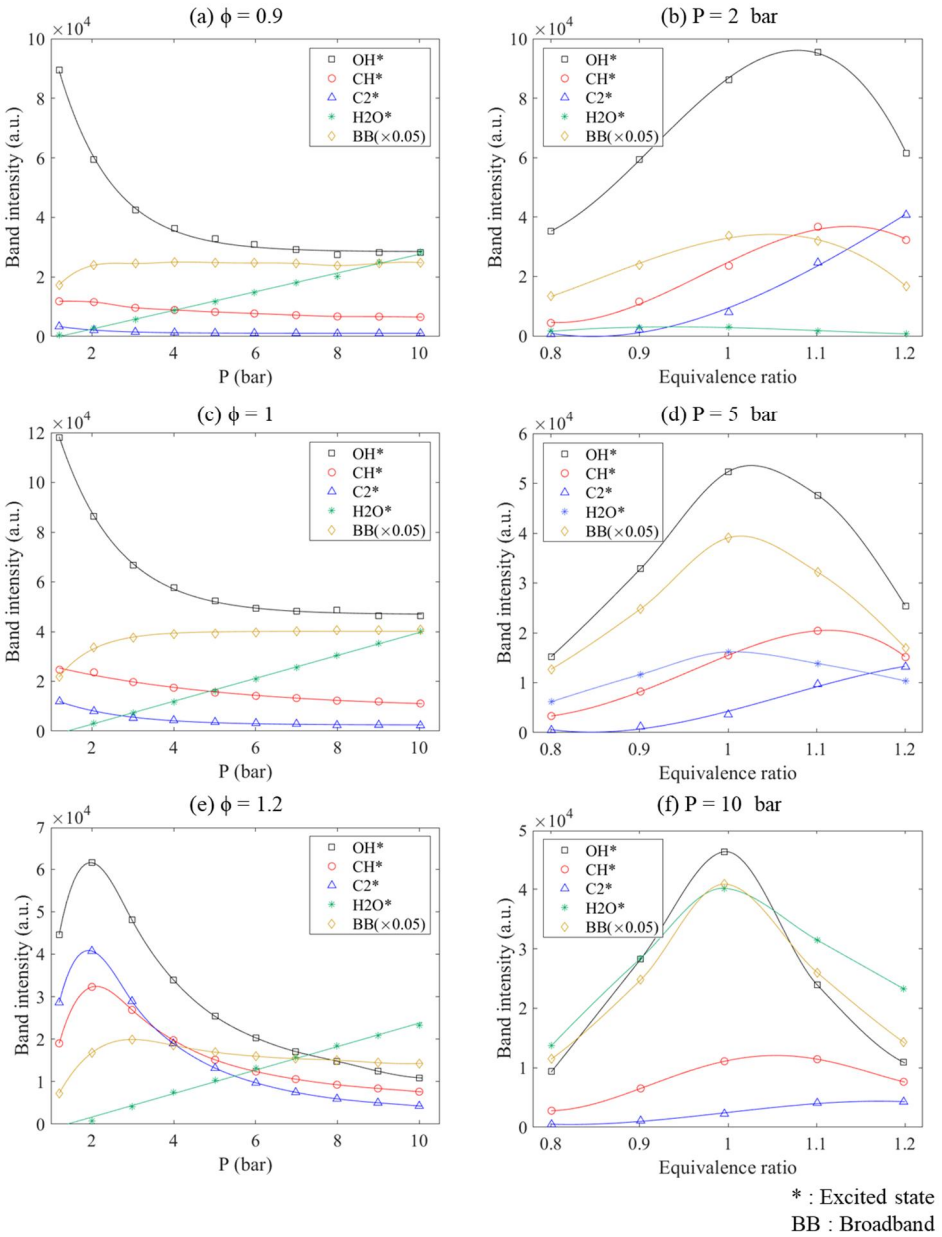

Figure 2.7 Band intensity variations of local features with variable ϕ and P

In the previous study, the band intensity ratio (BIR) which compensates for the nonmonotonic behavior of the local spectral features has been utilized to calibrate the gas properties. Therefore, obtaining one-to-one calibration functions between ratios and gas properties within certain property ranges is possible. The main purpose of normalizing the radical band intensity using another band intensity is to remove the impact of nonmonotonic temperature variation, allowing a normalized band intensity to only indicate the given fuel concentration. Figure 2.8 (a), (c), and (e) show that BIR between radicals, i.e., CH*/OH*, C_2*/OH*, and C_2*/CH*. As shown in Figure 2.8 (a), all the BIRs of radicals monotonically increase with ϕ between 0.8 and 1.2, which provides one-to-one calibration functions even though the slope of the functions, the sensitivity of the indicators, is flat in fuel-lean conditions, which implies low accuracy in measurement. However, Figure 2.8 (c) demonstrates that these monotonic trends of BIR change to nonmonotonic in lean conditions, and thereby, the indicators do not work under $\phi = 1$ in high pressure. This is because the BIR of radicals does not take into account the effect of pressure that affects the emission spectrum, as shown in Figure 2.8 (e). A normalization factor such as BB can also be used to exclude or reduce the influence of gas properties since BB is strongly affected by ambient pressure and temperature. As shown in Figure 2.8 (b) and (d), CH*/BB can be an indicator of equivalence ratio in low-pressure conditions but also it does not work well in high-pressure conditions. Otherwise, Figure 2.8 (f) shows that H_2O*/BB is linearly proportional to pressure, resulting in a reasonable pressure indicator.

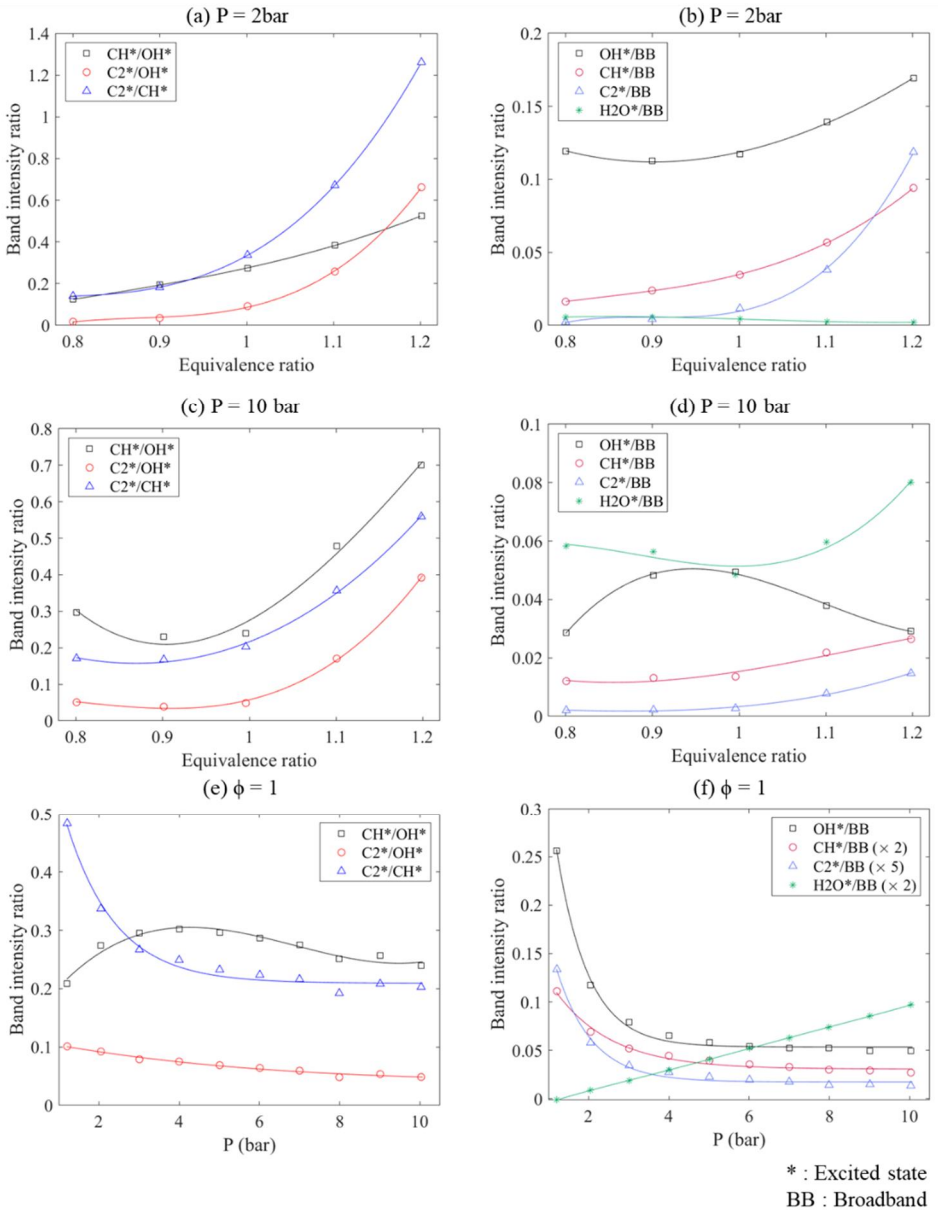

Figure 2.8 Band intensity ratio (BIR) versus ϕ and P in methane-air flame

CHAPTER 3. DEVELOPMENT OF DATA-DRIVEN CALIBRATION PROCESS

3.1 Overview of data-driven calibration process

It is evident that there is a strong correlation between the intensity of each distinct radical emission band and the chemical reaction paths. These reactions are affected by properties such as e.g., equivalence ratio (ϕ), component concentration (χ), temperature (T), and ambient pressure (P). For example, the band intensity area and its ratios of excited species are presented in section 2.3 and the relations between gas properties are discussed. Although some indicators can be calibrated to gas properties, it is difficult to manually find indicators with a high sensitivity to the target property over a wide range of pressure and equivalence ratios. Furthermore, an indicator, for example, the integrated OH* intensity (band intensity), cannot fully exploit spectral variation on the high-dimensional OH* profile affected by gas properties since the band structure of OH* in the range of 306 – 338 nm includes branches such as (0, 0) R, (0, 0) Q, (1,1) R, and (1,1) Q which can also be changed by chemical reactions that affect the relative population of the rot-vibrational levels [12]. In the presence of these detailed band structures from each radical in a wide wavelength range, finding indicators such as band intensity and its ratio is a tedious and repetitive process. To overcome these limitations, a data-driven calibration

approach can allow the extraction of variations in features based on spectral datasets to produce a calibration function. As long as the dataset contains sufficient information to represent the characteristics, a data-driven approach can benefit from the estimation of nonlinear trends of spectral variation to map target properties. Moreover, the data-driven calibration well adapts to any form of spectrum data, regardless of the wavelength range and resolution, requiring no pre- or post-processing, and to various flame properties, including equivalence ratio, pressure, temperature, and diluent concentration.

In this chapter, a data-driven calibration method based on ROM is presented. ROM has been widely applied in many engineering disciplines, e.g. computational fluid/structure dynamics [75, 76], dynamic control [77], and design optimization [78-80] since ROM reduces the computational complexity and storage requirements of a computer model while maintaining the desired fidelity. The ROM of the calibration process includes the high-dimensional non-linear system from the spectral domain (the number of CCD pixels) to the gas properties (P and ϕ). With this approximate model, gas properties can be estimated within predictable error without additional data from electrical sensors or chemical reaction simulation.

3.2 Calibration framework based on data-driven approach

A framework of the data-driven calibration method based on ROM is presented in Figure 3.1. The high dimensional spectral decomposed by selected POD bases and the variation of these bases mapped with the Kriging model also called Gaussian process regression. Moreover, to validate and analyze the ROM, leave-one-out cross-validation (LOOCV) and global sensitivity analysis (GSA) are introduced. A detailed explanation is given below.

In the case of spectral data, the snapshot matrix subject to POD consists of N_S samples of U_i which represents a raw spectrum vector with W components; e.g., a spectral vector having the dimension (W) of 2,000 emission intensities at 2,000 wavelength pixels from the CCD sensor. It is difficult to correlate the U_i directly with the gas properties of interest, e.g., ϕ, χ, T, and P, due to its high dimension. By extracting and selecting the number ($\mathrm{N_M}$) of principal vectors (φ_j, the basis of the U_i-space), POD can reduce the dimension of U_i. These bases (φ_j) span the entire spectrum vector space used for calibration and define the fundamental directions that represent the spectral variations by gas properties. As a result, the POD coefficient, which is the projection of U_i on each basis ($\alpha_{i,j}$, contribution of φ_j in U_i), becomes highly sensitive to the properties of the gas. This means that a vector of POD coefficient is a low-dimensional ($\mathrm{N_M}$) representation of the original spectrum data. A Kriging model, capable of handling nonlinear systems, can then be used to correlate the vector of the POD coefficient ($\mathrm{N_M} \ll W$) to the gas properties of

interest. A GSA quantifies the contributions of each POD basis on determining the output of the model, i.e., the properties of the gas.

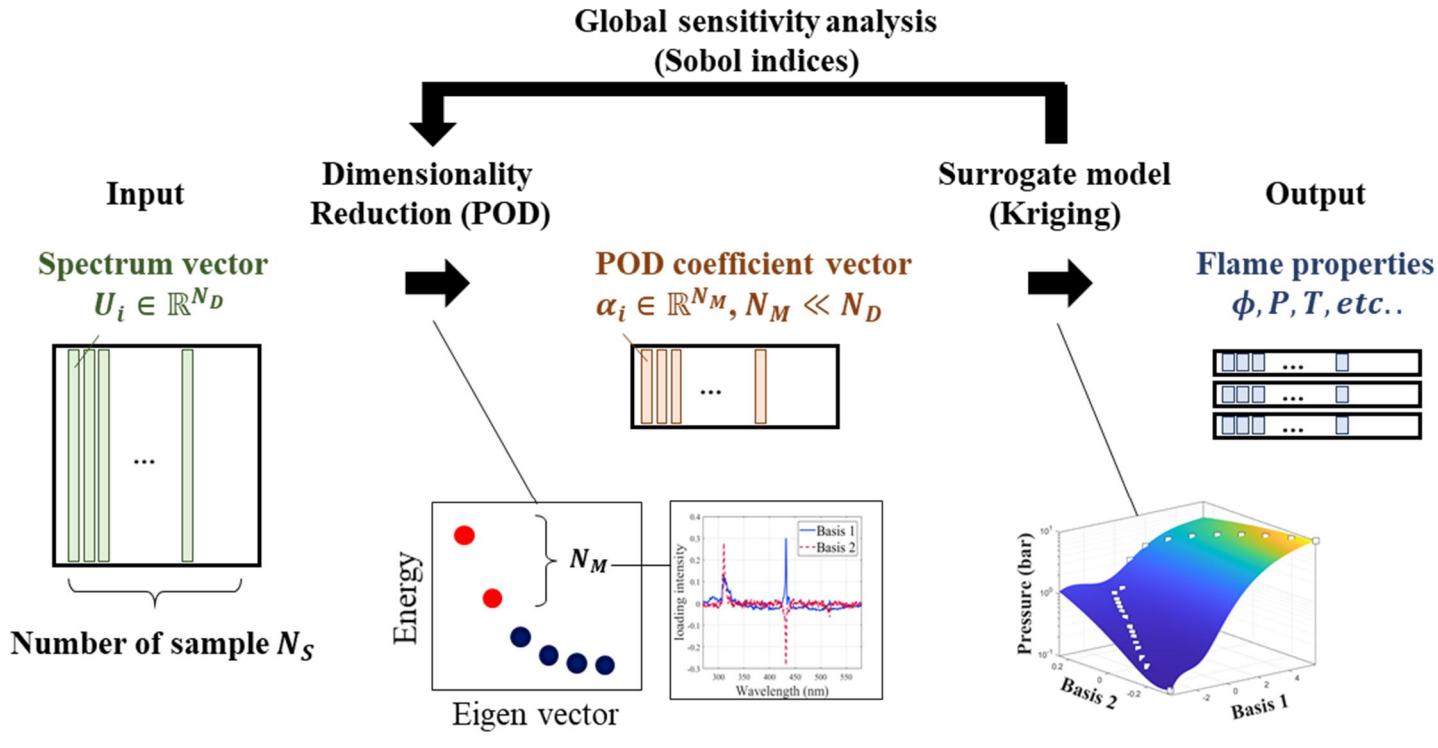

Figure 3.1 Framework of data-driven calibration process using POD, Kriging model, and GSA

3.2.1 Training and test dataset

The flame emission spectra from a stable methane-air flat flame are collected. The details of the experimental setup were discussed in Chapter 2. The exposure time was selected as 2 seconds due to the sufficiently high SNR of the signals. Raw signals are processed by subtracting the dark spectra collected without flame. The subtracted signals are then normalized by the intensity of the averaged OH* bands from 306 – 313 nm because OH* shows distinct features of the overall gas property conditions examined in this work. As shown in Figure 3.2, data from 80 flame conditions were used to train and test the ROM with varying ϕ (0.8 – 1.2) and pressures (1 – 10 bar). The training data, indicated by the green squares, is sampled based on a full factorial design of 50 different gas conditions to cover combinations of target properties. The training data is used to train and validate the ROM calibration process, which is supposed to be a calibration dataset collected prior to arbitrary measurements. After the ROM model is constructed, the prediction accuracy of the training data is evaluated by REC which will be discussed later in section 3.2.5. The test data, indicated by black circles, is randomly sampled based on Latin hypercube sampling of 30 gas conditions [81]. The test data represents FES from arbitrary flame conditions. The accuracy and precision of prediction using test data are evaluated by REP and RSD respectively, which will also be discussed in section 3.2.5. For each case, 10 chemiluminescence signals are collected to analyze the statistical deviation of signal and uncertainty in measurement.

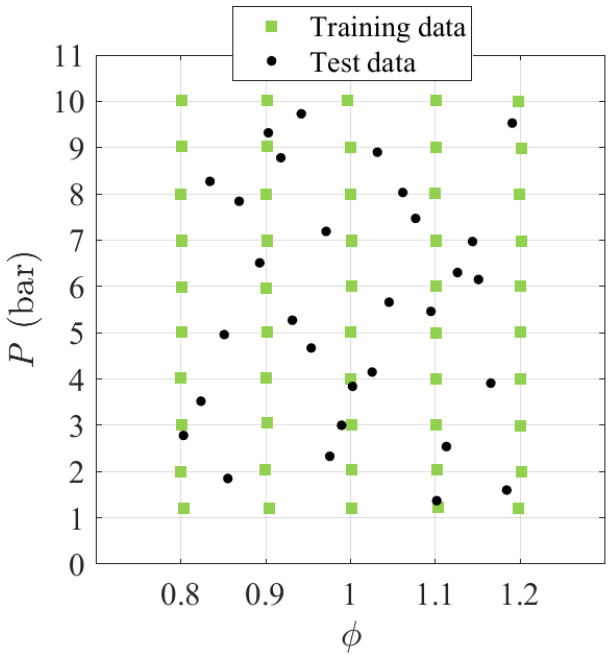

Figure 3.2 Experimental data matrix

3.2.2 Proper orthogonal decomposition (POD)

POD, known as the Karhunen-Loeve decomposition or Principle Component Analysis, is a dimension reduction method that projects high-dimensional data into a low-dimensional linear space as shown in Figure 3.3. Snapshots of spectral data are stacked in terms of column vectors, $\boldsymbol{U}' = \left[\boldsymbol{U}_1 - \overline{\boldsymbol{U}}, \dots, \boldsymbol{U}_{N_S} - \overline{\boldsymbol{U}}\ \right] \in \mathbb{R}^{W \times \boldsymbol{N_S}}$ with the average $\overline{\boldsymbol{U}} \in \mathbb{R}^{\boldsymbol{N_D}}$ value removed. The POD method selects the optimal basis of low-dimensional linear space to maximize the variance of projections of high-dimensional data [82].

$$\max_{\psi} \frac{\langle |(U_i', \psi_j)^2| \rangle}{(\psi_j, \psi_j)} = \frac{\langle |(U_i', \varphi_j)^2| \rangle}{(\varphi_j, \varphi_j)}, \text{subject to } (\psi_j, \psi_k) = \delta_{j,k} \qquad (3.1)$$

where $\varphi_j \in \mathbb{R}^{N_D}$, U_i', $\delta_{j,k}$, $(\cdot,\cdot)$, and $\langle\cdot\rangle$ represent j^{th} POD basis, i^{th} snapshot vector, Kronecker delta, inner product, and averaging operation, respectively. It is known that this optimization problem can be determined by the eigenvalue problem that finds the eigenvectors and eigenvalues of the covariance matrix, $\mathbf{K} = \frac{1}{W}\boldsymbol{U'}\boldsymbol{U'}^{\boldsymbol{T}}$.

As the number of data cases is smaller than the size of the spectral component ($W \gg \boldsymbol{N_S}$) in the calibration process, the size of the covariance matrix ($W \times W$) is so large that the computational cost for finding eigenfunctions becomes practically difficult. Therefore, the snapshot POD method which yields the same decomposed basis with a smaller sized covariance matrix $\mathbf{K} = \frac{1}{N_S}\boldsymbol{U'}^{\boldsymbol{T}}\boldsymbol{U'}$ ($\boldsymbol{N_S} \times \boldsymbol{N_S}$) is utilized [83]. The energy content (E_j), representing the contribution of the eigenvector (φ_j) to spectral variation, is proportional to the eigenvalue (λ_j) of the corresponding eigenvector.

$$E_j = \lambda_j \Big/ \sum_{k=1}^{N_S} \lambda_k \qquad (3.2)$$

Several dominant bases contain most of the energy, so $\mathrm{N_M}$ bases can be selected. The remaining minor bases can be ignored as truncation errors, which significantly reduces the snapshot's dimensions and excludes random noise that is irrelevant to the

change in gas properties [84]. Then each snapshot (U_i), the spectrum vector, can be expressed with minimal dimension ($\mathrm{N_M}$) as eq. (3.3).

$$\boldsymbol{U}_i \approx \sum_{j=1}^{N_M} \alpha_{i,j}\varphi_j + \overline{\boldsymbol{U}}, \qquad N_M \ll W \tag{3.3}$$

where $\alpha_{i,j}$ is the vector of POD coefficients that is the projection of the spectral vector $U_i{}'$ on the eigenvector φ_j.

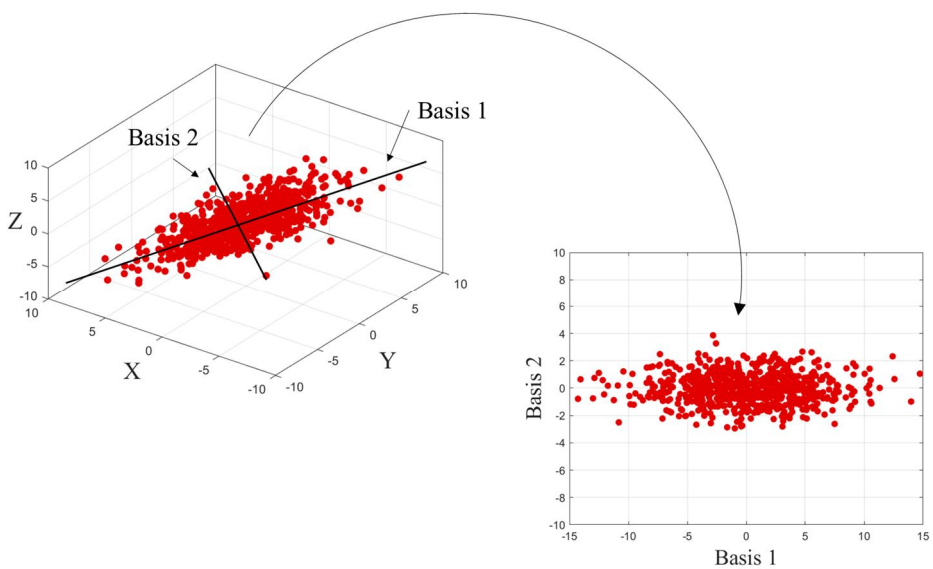

Figure 3.3 Dimension reduction process using POD analysis

3.2.3 Kriging model

A surrogate model is constructed using the POD coefficients of the spectrum vector as input, and the gas properties of interest as output. The Kriging model, also known as Gaussian process regression, is chosen as a surrogate model because of its high flexibility in handling nonlinear problems and its statistical nature to compute empirical confidence intervals [78, 85]. Figure 3.4 illustrates the Kriging model as an approximate model of a real function, which was constructed from a small number of observations.

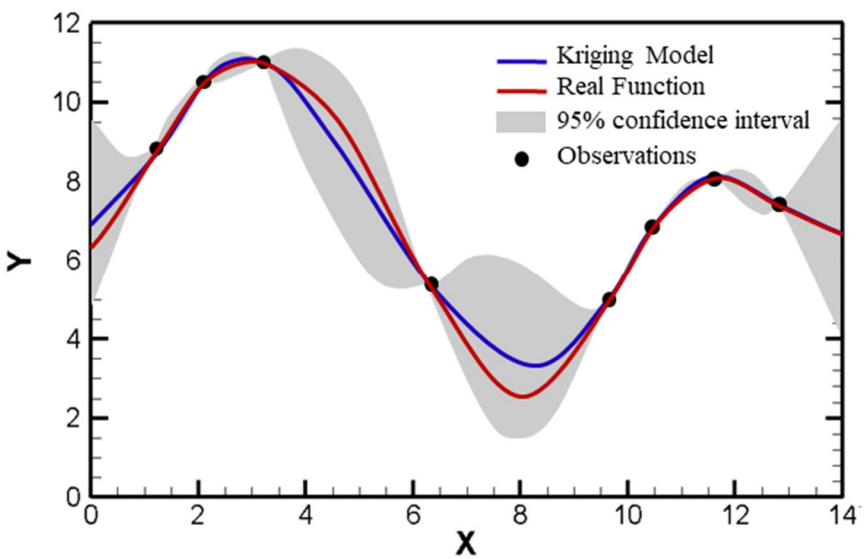

Figure 3.4 Illustration of the Kriging model in one dimension

A Kriging model constructs an approximation model of an unknown function of interest ($y(x)$) using a global approximation function (β) and a stochastic process

with zero-mean ($Z(\boldsymbol{x})$) as eq. (3.4).

$$y(\boldsymbol{x}) = \beta + Z(\boldsymbol{x}) \tag{3.4}$$

In this study, ordinary Kriging assuming constant value β was used and the stochastic process is modeled as a Gaussian and stationary random process with zero mean. The covariance of the stochastic process is presented as eq. (3.5)

$$\mathrm{Cov}\left[Z\left(\boldsymbol{x}^i\right), Z\left(\boldsymbol{x}^j\right)\right] = \sigma^2 \boldsymbol{K}[R(\boldsymbol{x}^i, \boldsymbol{x}^j)] \tag{3.5}$$

$$R\left(x_i, x_j\right) = \exp\left[-\sum_{k=1}^{p} \theta_k \left|x_k^i - x_k^j\right|^2\right] \tag{3.6}$$

where σ^2 is the process variance and $R\left(\boldsymbol{x}^i, \boldsymbol{x}^j\right)$ is a correlation function assumed to depend on the Euclidean distance to reduce complexity. In eq. (3.6), p is the number of design variables, and θ_k are correlation parameters that control the range of influence of nearby points, thereby affecting the smoothness. The correlation parameter (θ_k) of the Gaussian function was optimized with a genetic algorithm optimizer to fit the model to the observed samples by maximizing the log-likelihood function, called maximum likelihood estimation (MLE).

If N_S (number of samples) observations of input ($\mathbf{X} = \{\boldsymbol{x}^1, \boldsymbol{x}^2, \ldots, \boldsymbol{x}^{N_S}\}^{\mathbf{T}}$) and output ($\boldsymbol{Y} = \left\{y^1, y^{\mathbf{2}}, \ldots, y^{N_S}\right\}^{\mathbf{T}}$) data pairs are given, an estimation of the new prediction $\hat{y}$ at $\boldsymbol{x}$ can be made using the linear predictor, $\hat{y}(\boldsymbol{x}) = \boldsymbol{W}^T(\boldsymbol{x})\boldsymbol{Y}$, where

$\boldsymbol{W}$ is a weight matrix, as illustrated in Figure 3.5. Likewise, the predictor of the Kriging model is defined as eq. (3.7).

$$\hat{y}(\boldsymbol{x}) = \hat{\beta} + \boldsymbol{r}^T(\boldsymbol{x})\boldsymbol{R}^{-1}(\boldsymbol{Y} - \boldsymbol{1}\hat{\beta}) \tag{3.7}$$

where $\hat{\beta}$, $\boldsymbol{1} \in \mathbb{R}^{N_S}$, $\boldsymbol{R} \in \mathbb{R}^{N_S \times N_S}$, $\boldsymbol{r} \in \mathbb{R}^{N_S}$ are the constant trend calculated $\hat{\beta} = (\boldsymbol{1}^T\boldsymbol{R}^{-1}\boldsymbol{1})^{-1}\boldsymbol{1}^T\boldsymbol{R}^{-1}\boldsymbol{Y}$, a vector of ones, correlation of all observed data, and correlation vector between new prediction and observed data, respectively.

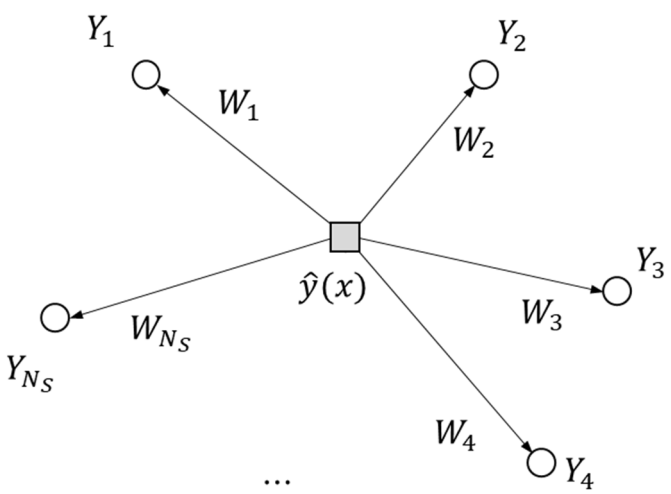

Figure 3.5 Illustration of Kriging predictor

3.2.4 Global sensitivity analysis (GSA): Sobol sensitivity indices

The Sobol sensitivity analysis is a variance-based GSA method that is used to rank the contribution of input parameters (e.g., $\alpha_{i,j}$ extracted from the input spectrum vector) to predicting output (e.g., ϕ, χ, T, and P). If the surrogate model (f) is an integrable function, the function can be represented as a summation of orthogonal functions as eq. (3.8) [86].

$$f = f_0 + \sum_{i}[f_i + \sum_{j>i}[f_{ij} + \sum_{k>j}\left(f_{ijk} + \sum_{l>k}(f_{ijkl} + \cdots + f_{1\cdots N_M})\right)]] \tag{3.8}$$

$$\int_0^1 f_{i_1,i_2,\cdots,i_s}(x_{i_1}, x_2, \cdots, x_s)dx_{i_w} = 0 \tag{3.9}$$

where $f = f(\boldsymbol{x})$ is the square-integrable function defined over the input parameter ($\boldsymbol{x} = [x_1, \cdots, x_{N_M}]$), and the elements are orthogonal decomposed functions of each combination of the input variables, i.e., $f_i = f_i(x_i)$, $f_{ij} = f_{ij}(x_i, x_j)$. Then, from eq. (3.8) and (3.9), the decomposed function can be expressed as below for any $i_w = i_1, i_2, \cdots, i_p$, where $1 \leq i_1 < i_2 < \cdots < i_s \leq N_M$,

$$f_0 = \int f(x)dx \tag{3.10}$$

$$f_i = \int f(x)\prod_{k\neq i} dx_k - f_0 \tag{3.11}$$

$$f_{i,j} = \int f(x) \prod_{k \neq i,j} dx_k - f_i - f_j - f_0 \tag{3.12}$$

If f is the square-integrable function, all decomposed functions $f_{i_1,i_2,\cdots,i_s}$ are square integrable. By squaring both sides of eq. 3.8 and applying the orthogonality condition, the decomposed variance equation (eq. 3.13) is valid. The variance (V) of the output induced by the change in an input parameter is decomposed as the sum of the average (V_0) and variance of each input parameter (V_k) and their coupled effects (V_{kl}, $V_{k(l+1)}$, …, V_{klm}, …).

$$\mathrm{V} = V_0 + \sum_{k=1}^{N_M} [V_k + \sum_{l>k} [V_{kl} + \sum_{m>l} \left(V_{klm} + \sum_{n>m} \left(V_{klmn} + \cdots + V_{k\ldots N_M} \right) \right)]] \tag{3.13}$$

A Sobol sensitivity indices are calculated as the ratio of the partial variance in response to the change in the input parameters (main effect or coupled effect) relative to the total variance:

$$\begin{aligned} &\text{Main Effect Sensitivity Index: } S_k = \frac{V_k}{V} \\ &\text{Coupled Effect Sensitivity Index: } S_{kl} = \frac{V_{kl}}{V} \end{aligned} \tag{3.14}$$

The summation of the main effect and coupled effect sensitivity index equals one, and the larger the S_k indicates the more significant response of the output by the kth input parameter. A Python library for sensitivity analysis, SALib[87], was used to calculate Sobol indices with the Saltelli sampling method [88].

3.2.5 Evaluation of accuracy and precision of calibration process

The accuracy and precision of the calibration methods are estimated quantitatively by three measures: the average relative error of the calibration data (REC), model prediction (REP), and relative standard deviation of the model prediction (RSD) [89]. The different calibration methods are compared using REC, REP, and RSD which indicate calibration accuracy, prediction accuracy, and prediction precision, respectively.

1) REC (%): the average relative error of the calibration (%) to assess the accuracy of calibration (training data in Figure 3.2)

$$REC\ \ (\%) = \frac{100}{N_{train}} \sum_{i=1}^{N_{train}} \left[\frac{1}{N_{i,shot}} \sum_{j=1}^{N_{i,shot}} \left| \frac{\hat{\pi}_{i,j} - \pi_{i,j}}{\pi_{i,j}} \right| \right] \tag{3.15}$$

where N_{train}, $N_{i,shot}$, $\hat{\pi}_{i,j}$, and $\pi_{i,j}$ are the number of training cases in the different conditions, the number of spectral shots in the ith condition, estimated gas property, and true gas properties measured by the sensors (considered as ground truth), respectively.

2) REP (%): the average relative error of the prediction (%) to assess the accuracy of prediction (test data in Figure 3.2)

$$REP\ \ (\%) = \frac{100}{N_{test}} \sum_{i=1}^{N_{test}} \left[\frac{1}{N_{i,shot}} \sum_{j=1}^{N_{i,shot}} \left| \frac{\hat{\pi}_{i,j} - \pi_{i,j}}{\pi_{i,j}} \right| \right] \tag{3.16}$$

where N_{test} is the number of test cases in different conditions.

3) RSD (%): the average relative standard deviation of the prediction to assess the precision of prediction (test data in Figure 3.2)

$$\begin{aligned} RSD\ \ (\%) &= \frac{100}{N_{test}} \sum_{k=1}^{N_{test}} \frac{\sigma_{y_k}}{\pi_k} \qquad with\ \ \sigma_{y_k}^2 \\ &= \sum_{j=1}^{N_{shot}} \frac{\left(\hat{\pi}_{k,j} - \pi_{k,j}\right)^2}{N_{shot} - 1} \end{aligned} \tag{3.17}$$

where π_k is the true gas properties of each test case.

3.3 Validation of data-driven calibration process

3.3.1 POD of flame emission spectra

The POD analysis is conducted on the 10-shot averaged high SNR dataset normalized by the intensity of the OH*band. Figure 3.6 shows the ten spectral bases in order of their contribution (energy content), and Figure 3.7 shows the energy content and cumulative energy of each basis. A total of 99.7% of the energy was accounted for by the five dominant bases which contain most of the gas property-sensitive spectral features. Basis 1 consists of dominant H_2O* bands and the broadband baseline profile from which radical emission bands are subtracted. As discussed in Figure 2.7 (b), (c), and (d), the variation of the spectral dataset with increasing pressure shows a diminishing radical emission band while increasing the broadband and H_2O* bands emission. Therefore, Basis 1 is expected to be highly sensitive to pressure variation. Basis 2 contains the distinct carbon-related radical emission bands which are also sensitive to the equivalence ratio as presented in Figure 2.7 (e) and (f). Basis 3 is also highly sensitive to pressure variation because it consists of H_2O* bands emission and negative radical emission band. Basis 4 – 6 primarily indicate the cross-correlations of the emission bands and bases 7 – 10 are dominated by noise signals that should be removed from the signals to improve the signal quality. Excluding these bases can help to reduce signals unrelated to changes in gas properties.

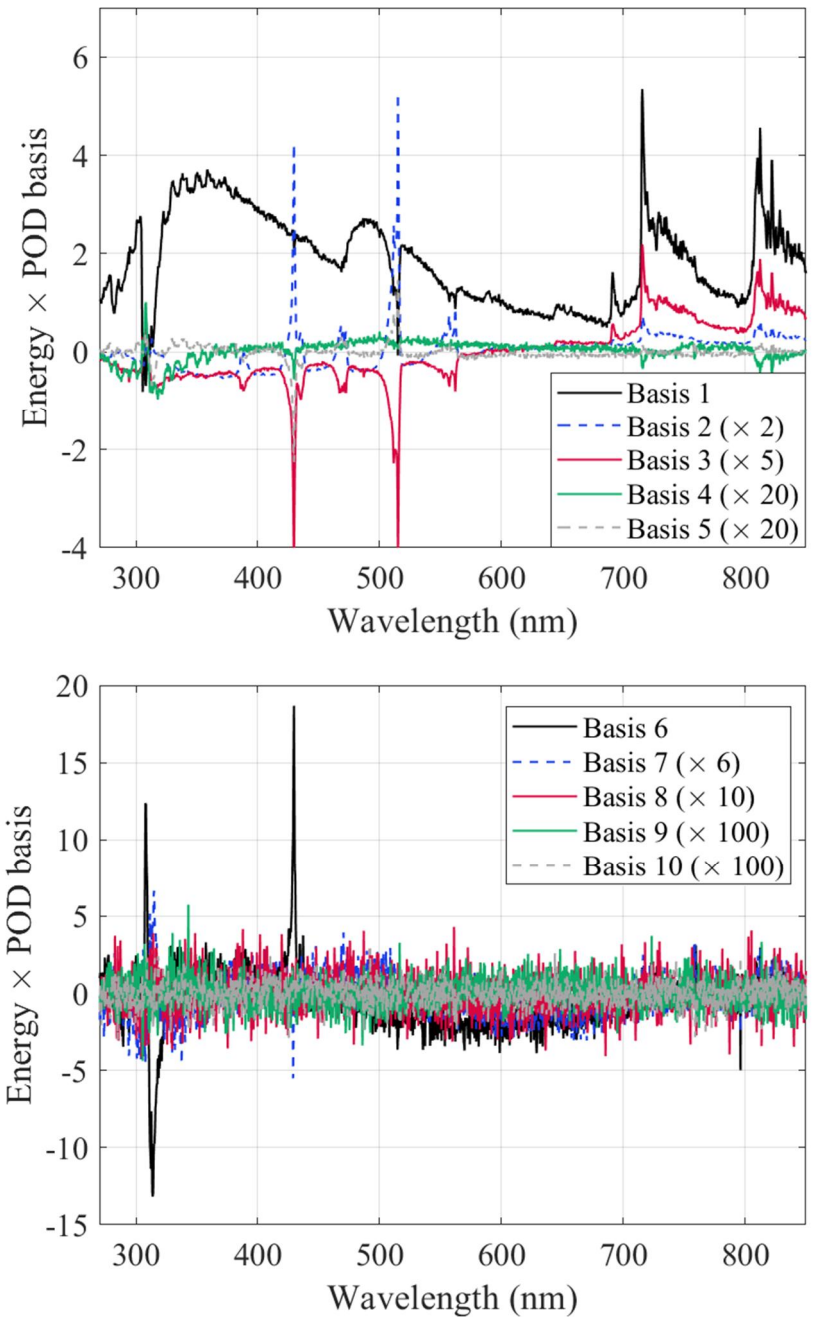

Figure 3.6 Ten dominant POD bases of spectrum data

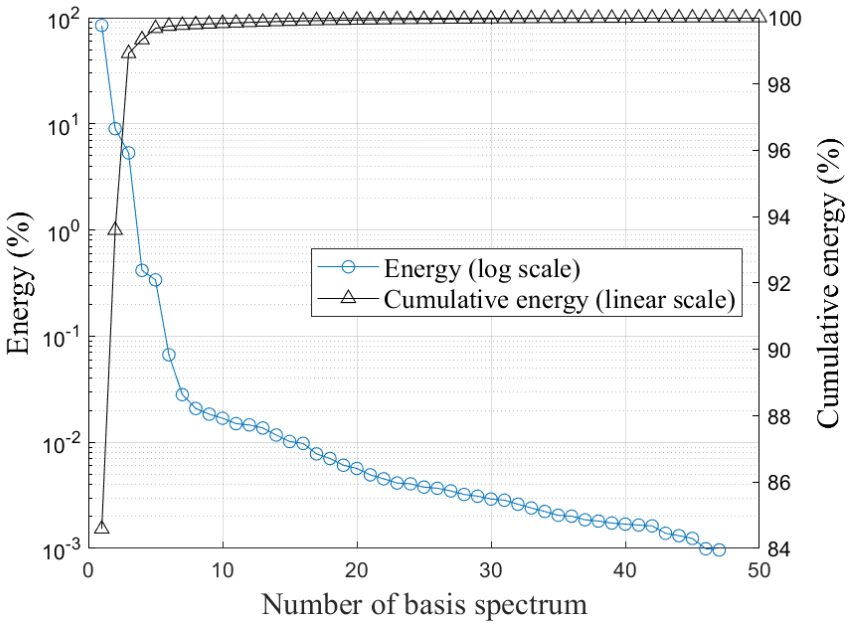

Figure 3.7 Energy contents of the POD bases

An emission spectrum ($\boldsymbol{U}_i$) can be decomposed by projection on the dominant bases (φ_j) and the corresponding POD coefficients ($\alpha_{i,j}$) as explained in Eq. (3.3). The variations of $\alpha_{i,j}$ of three dominant bases are shown in Figure 3.8. As mentioned, Basis 1 has P-sensitive features such as broadband and H_2O^* with subtracted radical emission. Figure 3.8 (a) shows that POD coefficients of Basis1 ($\alpha_{i,1}$) monotonically rise with increase of pressure in all equivalence ratio conditions. Moreover, POD coefficients of Basis2 ($\alpha_{i,2}$) monotonically rise with increase of ϕ in all equivalence ratio conditions except 0.8 – 0.9 of ϕ at the highest pressure. In other words, the coefficients of each POD basis can be an indicator of gas properties, instead of each emission intensity and its ratio.

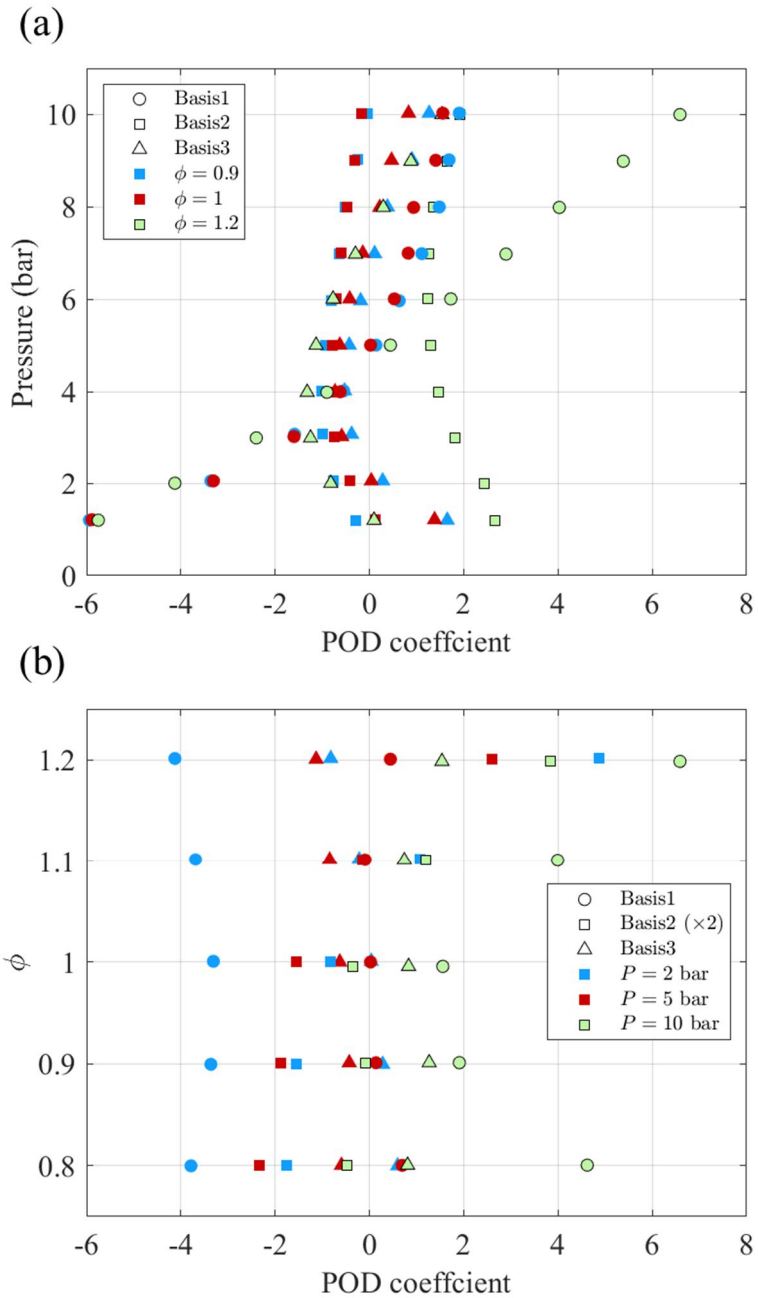

Figure 3.8 POD coefficient distributions projected on (a) P-$\alpha_{i,j}$ (ϕ = 0.9, 1, and 1.2) and (b) ϕ-$\alpha_{i,j}$ (P = 2, 5, 10 bar) planes

The reference raw spectra and the reconstructed spectra using only the five dominant spectrum bases (99.7% of energy content) and the corresponding POD coefficients are compared to investigate whether the POD basis can represent the raw spectra. Figure 3.9 shows the reference and reconstructed spectra of selected gas properties conditions in the wide wavelength range, illustrating the local features of band emission. The reconstructions of representative properties-sensitive spectral features such as the broadband baseline profiles and the emission bands of OH*, CH*, C_2*, and H_2O* are in good agreement with raw spectra. Thus, the POD space with the five variables, $\alpha_{i,1}$, $\alpha_{i,2}$, $\alpha_{i,3}, \alpha_{i,4}$, and $\alpha_{i,5}$, is capable of fully spanning the entire spectral data with varied gas properties. The result is consistent with the hypothesis that information about gas properties survives the POD decomposition process through the five dominant bases, which results in a significant reduction of the dimensionality of variation for spectra data. In other words, the POD coefficients can effectively represent the entire information about gas properties contained in the emission spectrum.

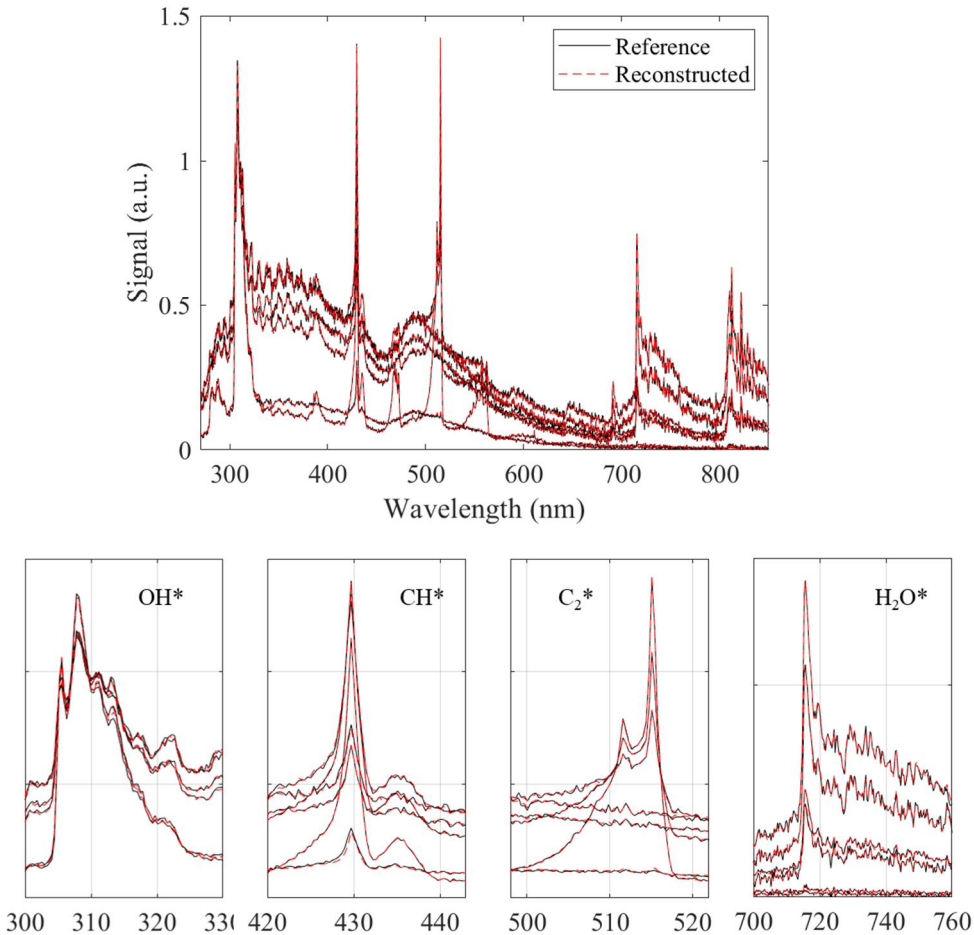

Figure 3.9 Data reconstruction results using the coefficients of five bases

3.3.2 Parametric study using Global sensitivity analysis (GSA)

The Sobol sensitivity indices of dominant bases for P and ϕ from the Kriging model constructed using the ten POD bases are shown in Figure 3.10 (a) and (b), respectively. As shown in Figure 3.10 (a), Basis 1 and 3 have the dominant

contribution to the pressure with Sobel indices 0.71 and 0.21, respectively. The radical bands are subtracted from the broadband baseline in Basis 1. Recall, as the pressure increases, the broadband and H_2O* bands (Bases 1 and 3) increased while the radical bands weakened. Figure 3.10 (b) shows that Basis 2 is the main contributor to ϕ-sensitivity in the Kriging model. The high ϕ-sensitivity of Basis 2 is intuitive because the basis has the distinct characteristics of carbon-related radical bands, specifically the CH* and C2* bands that are directly related to fuel concentration. It is noteworthy that the ϕ-sensitivity of Basis 1 is significantly low (0.10) given its high energy content (84.6%), implying that the broadband baseline with subtracted radical emission bands is nearly insensitive to ϕ variation. This is because the influence of temperature on the broadband baseline was diminished by normalizing the spectra dataset using the OH* band intensity before calibration. The remaining dominant bases correspond to the cross-correlations of the distinct emission bands which have non-negligible impacts on the ϕ-sensitivity of the model, that is, the ϕ-sensitivity indices for Bases 3, 4, and 5 are 0.12, 0.09, and 0.09, respectively.

It is clear that the five dominant bases (1 – 5) as well as their coupled effects determine the outputs of gas properties from the Kriging model. Hence, POD coefficient vectors ($\alpha_{i,1}$, $\alpha_{i,2}$, $\alpha_{i,3}$, $\alpha_{i,4}$, and $\alpha_{i,5}$) including both the separate and coupled effects of the five bases are sufficient as the input to predict the gas properties in the calibration process. As mentioned in the previous section, the basis

vectors were chosen based on their contribution (energy contents) to the variations in the spectrum dataset, whereas the sensitivity indices of indicating how the variation of each gas property related to the POD bases. Consequently, the numbering of the bases in Figure 3.7 based on contained energy does not indicate the order of sensitivity indices for gas properties in Figure 3.10.

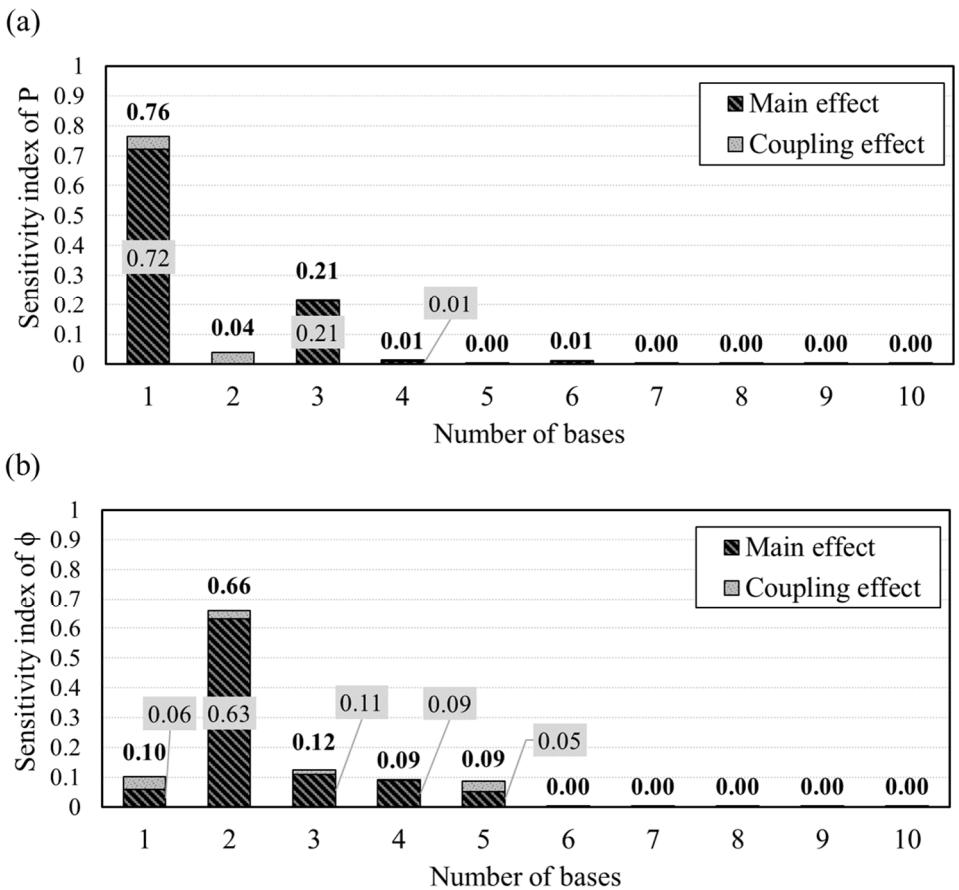

Figure 3.10 Sobol sensitivity indices of P and ϕ: bold label indicates total effect (main + coupling effect) and the shaded label indicates main effect

3.3.3 Validation of Kriging model

A Kriging model is constructed to correlate the vector consisting of POD coefficients of the five bases with P and ϕ so that the ROM can predict the gas properties with an unknown flame emission spectrum as input. The coefficients are calibrated using a training dataset of 50 (10 P and 5 ϕ levels) full factorial data points, 1 bar P-interval between 1 and 5 bars, and 0.1 ϕ-interval between 0.8 and 1.2. The LOOCV method is used to validate the Kriging model. LOOCV is a cross-validation method that leaves out one value, predicts the data sample by the rest of the observed value, and continues with next point value. Figure 3.11 illustrates the results of LOOCV as symbols that represent the predicted vs. sensor-measured (used as ground truth) values, along with a line representing the matched values. R-squared values quantifying the prediction accuracy of the model are 0.9986 and 0.975 for P and ϕ, respectively. It is noteworthy that the majority of prediction errors come from data points near the upper and lower limits. These results could suggest more data points to train the model near the upper and lower limits, although the prediction accuracy of P and ϕ are still acceptably high.

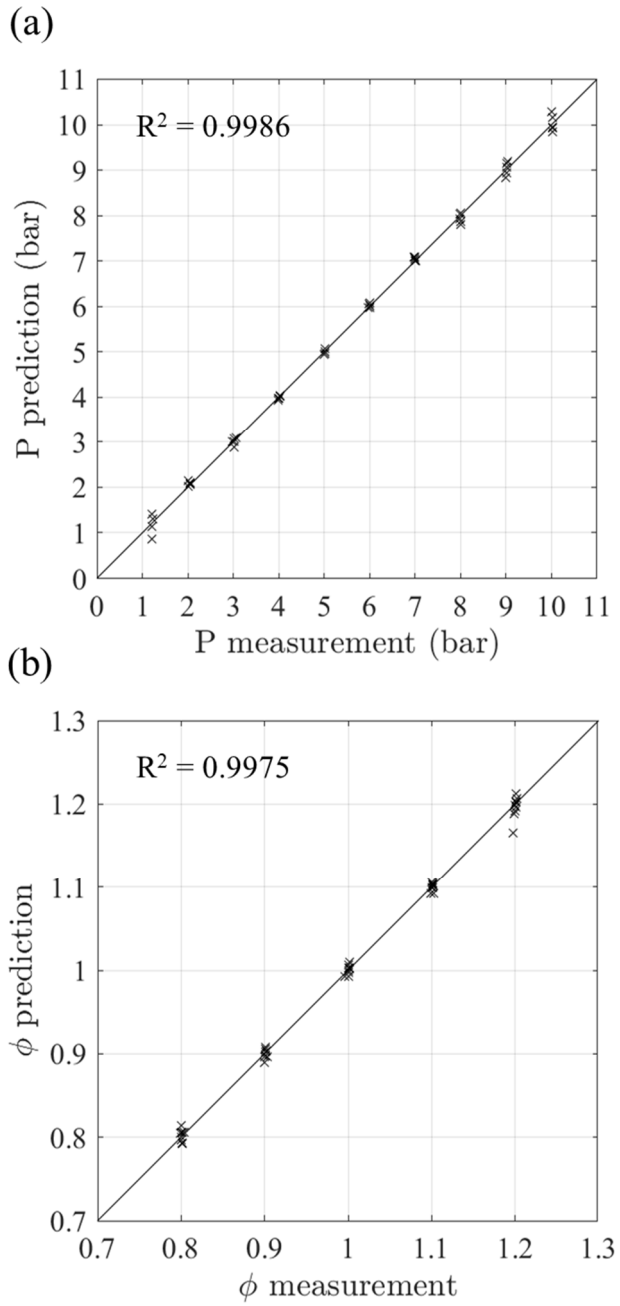

Figure 3.11 Leave-one-out cross-validation (LOOCV) of the Kriging model

3.4 Results of data-driven calibration process

3.4.1 Calibration result on experimental data

The proposed calibration process is applied to arbitrary flame emission to predict the gas properties of the combustion region. Recall that the full factorial dataset (green squares in Figure 3.2) was used to train the calibration ROM and to validate itself, and flame emission spectra at 30 different experimental conditions (black dots in Figure 3.2) were randomly selected using the Latin hypercube sampling method to evaluate and justify the accuracy of the gas property prediction model. Figure 3.12 and Figure 3.13 show the results of the prediction of P and ϕ using various calibration techniques as inputs on the 2 s exposure time dataset. The marker and error bar indicate average values and standard deviation of 10 shots of prediction at the same conditions, respectively. The proposed calibration model referred to as POD + Kriging is compared with other methods, including conventional regression methods that utilize band intensities (BI) and the data-driven PLS-R approach. For the conventional regression methods, local spectral characteristics were selected empirically based on sensitivity to P and ϕ: OH* (306–338 nm), CH* (420 – 443 nm), C_2* (498 – 521 nm), H_2O* (713 – 791 nm), and BB (270 – 650 nm) emission bands. Vectors of BI values are correlated with gas properties using MLR, which is a widely used statistical technique based on the linear relationship between independent parameters and response variables. The following sets of property indicators are selected to build three different MLR models: 1) BI5 for OH*, CH*,

C_2*, H_2O*, 2) BI3 for OH*, CH*, and C2*, and 3) BI2 for BB and H_2O*. For the PLS-R model, five components are chosen, which are the same number of POD bases.

The predictions of the data-driven model, i.e. PLS-R and POD/Kriging, have higher prediction accuracy and precision within the total range of P and ϕ compared to the BI + regression methods. It is evident that the data-driven feature extraction methods are more accurate and precise than the method using manually selected local features as gas property indicators. Furthermore, the proposed POD/Kriging method shows significant improvement in prediction accuracy compared to that of PLS-R. This is mainly because the Kriging method can handle nonlinear and multimodal correlations, whereas the PLS-R method is based on linear regression. Also, it is noteworthy that MLR with BI5 provides better prediction accuracy of ϕ and P than MLR with BI3 of OH*, CH*, and C_2* which are the three most ϕ-sensitive local spectral features, and with BI2 of H_2O* and BB which are the two most P-sensitive local spectral features. BI3/MLR has low accuracy of P-prediction due to the lack of information regarding spectral features, i.e. BB and H_2O*, that are sensitive to P. Likewise, BI2/MLR does not contain radical spectral features that are sensitive to ϕ, resulting in very low accuracy of ϕ-prediction. To improve the accuracy of each gas property using a manually selected indicator, it is very important to choose appropriate features.

REC, REP, and RSD are calculated to determine calibration accuracy, prediction

accuracy, and prediction precision, respectively, which are used to compare quantitatively the performance of different calibration methods. Table 3.1 summarizes the accuracy and precision results from the calibration techniques. REPs obtained using the POD/Kriging method are 1.71% and 0.55% for the pressure and equivalence ratio. RSDs are 1.37% and 0.54% for the pressure and equivalence ratio, respectively.

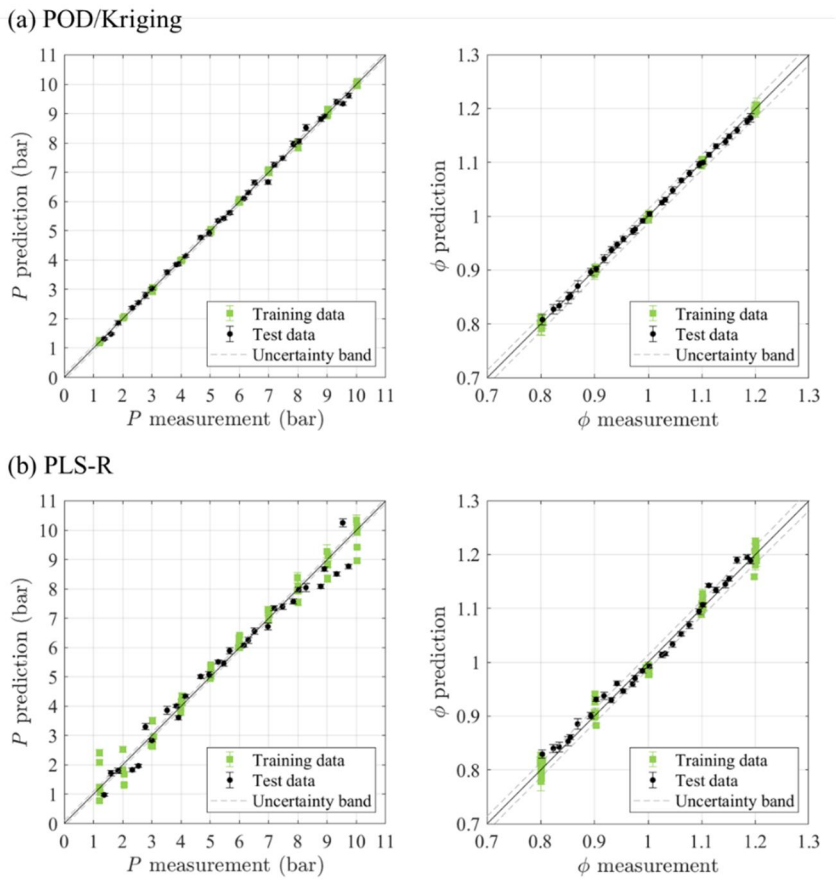

Figure 3.12 Prediction of P and ϕ using (a) POD/Kriging (Proposed method) and (b) PLS-R

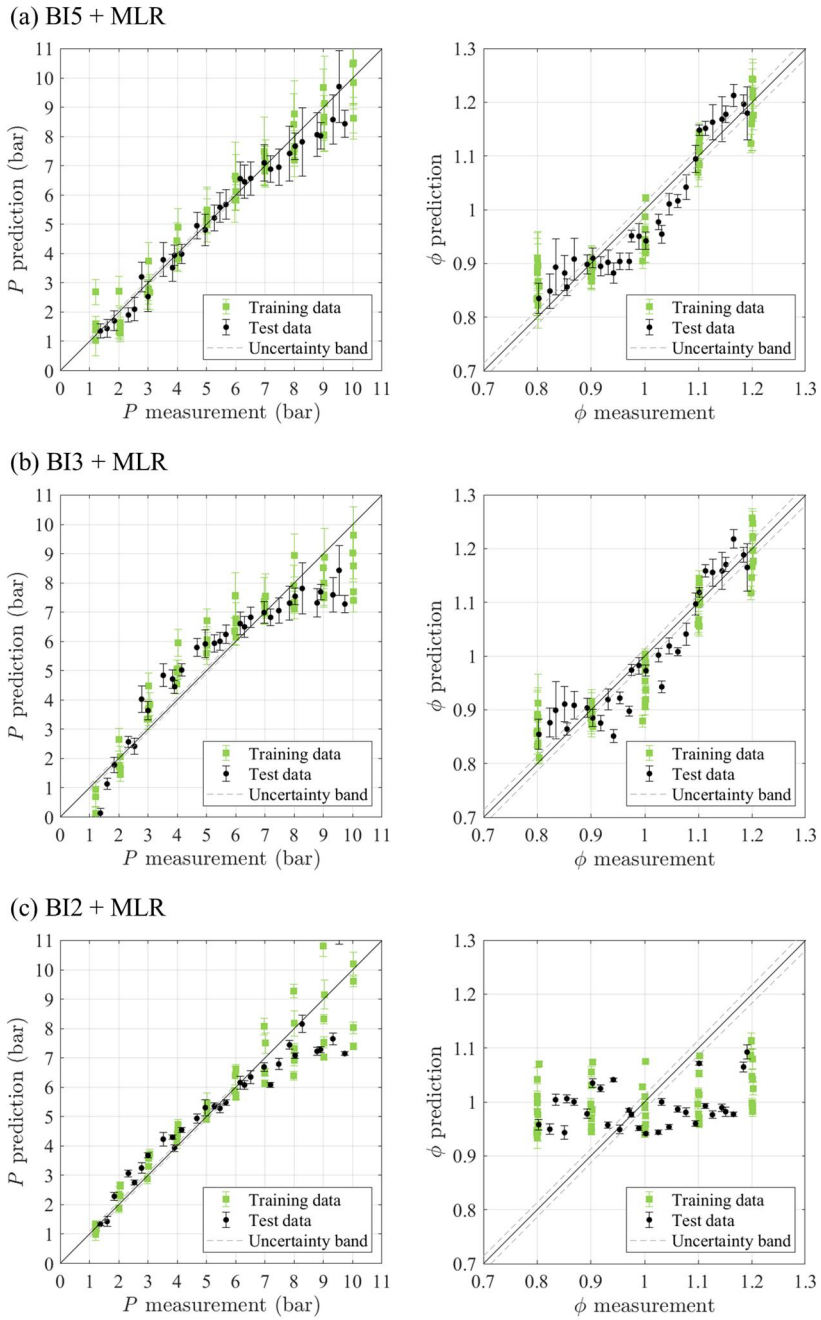

Figure 3.13 Prediction of P and ϕ using (a) BI5 (OH*, CH*, C_2*, BB, H_2O*) / MLR (b) BI3 (OH*, CH*, C_2*) / MLR, and (c) BI2 (BB, H_2O*) / MLR

Table 3.1 Comparison of quantitative performance parameters for calibration techniques: POD/Kriging (Proposed method), PLS-R, BI5/MLR, BI3/MLR, and BI2/MLR

	POD/Kriging			PLS-R					
Unit: %	REC	REP	RSD	REC	REP	RSD			
P	1.52	1.71	1.37	10.5	7.04	1.8			
ϕ	0.62	0.55	0.54	1.41	1.23	0.56			
	BI5/MLR			BI3/MLR			BI2/MLR		
Unit: %	REC	REP	RSD	REC	REP	RSD	REC	REP	RSD
P	16.8	10.7	11.1	22.5	17.8	7.55	11.7	11.4	3.30
ϕ	4.50	3.87	2.35	4.45	3.83	1.96	12.0	9.93	0.70

*REC: average relative error of calibration data, REP: average relative error of model prediction, RSD: average relative standard deviation of predicted gas properties.

3.4.2 Wavelength range effect on calibration accuracy

There is a strong correlation between flame spectra and flame properties such as pressure and equivalence ratio. Even so, the wavelength regions sensitive to gas properties are spread across a wide range of wavelengths while each band emission is correlated with the other. Therefore, the selection of an appropriate wavelength range in which gas characteristic information is included is expected to be critical. Figure 3.14 and Table 3.2 show the wavelength range effect on the accuracy and precision of prediction with two wavelength ranges: 270 – 650 nm where OH*, CH*, C_2*, and BB are observed and 650 – 850 nm where H_2O* is contained. The accuracy of P prediction is significantly degraded using 270 – 650 nm compared to that of 270 – 850 nm while the REP of ϕ only increased by 0.2%. Moreover, using only H_2O* in a relatively narrow wavelength range (650 – 850 nm) has relatively good accuracy (4% of REP), whereas the accuracy of ϕ deteriorates greatly to 11.2%. This is because H_2O* band emission is sensitive to pressure variation but insensitive to ϕ variation. In summary, for higher accuracy and precision in data-driven calibration, it is important to select a wavelength range with sufficient gas characteristic information.

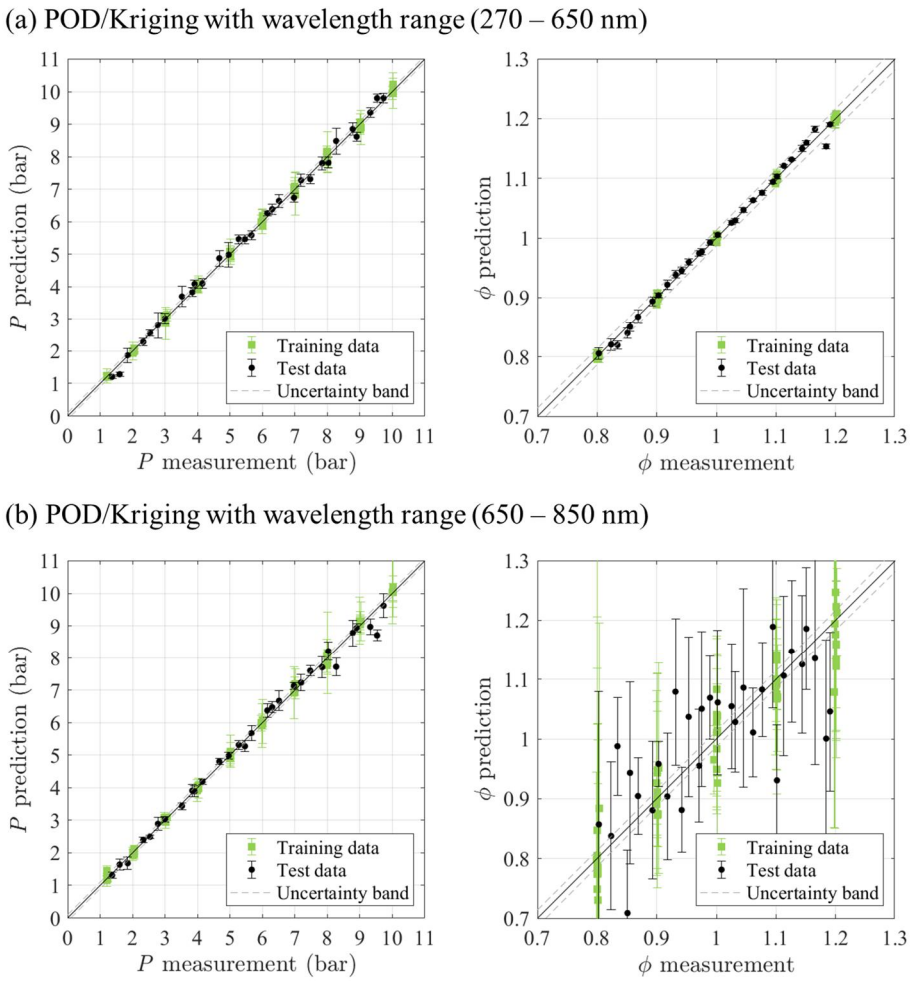

Figure 3.14 Prediction of P and ϕ using POD/Kriging from the dataset in the wavelength ranges (a) 270 – 650 nm and (b) 650 – 850 nm

Table 3.2 Comparison of quantitative performance parameters for POD/Kriging with varied wavelength ranges

	Total (270 – 850 nm)			270 – 650 nm			650 – 850 nm		
Unit: %	REC	REP	RSD	REC	REP	RSD	REC	REP	RSD
P	1.52	1.71	1.37	4.01	4.58	3.97	5.03	4.00	3.83
ϕ	0.62	0.55	0.54	0.59	0.71	0.56	14.7	11.2	11.6

3.4.3 Calibration result on simulation data

The proposed calibration process is applied to predict simulation data such as adiabatic flame temperature (T_{ad}), flame speed (S_l), and concentration of NO, NO_2, CO, and CO_2. This section demonstrates the potential of the proposed calibration process for applications to predict pollutant gas emissions, which is important for combustion diagnostics. These properties are determined by sensor-measured ϕ and P using 1D chemical reaction simulation with GRI-Mech 3.0 as presented in section 2.2. The calibration target is a laminar flat flame burner so the simulation data can follow the qualitative trends of the actual variation of gas properties such as temperature and concentration. If flame emissions have sufficient sensitivity to variation of gas properties, prediction of these properties can be possible. Six POD bases are chosen to construct the Kriging model based on the GSA, and the prediction of T_{ad}, S_l, χ_{NO}, χ_{NO_2}, χ_{CO}, and χ_{CO_2} are shown in Figure 3.15 and Table 3.3. The results show reasonable predictions of gas properties within the total range of each gas property, even though those are simulation results rather than experimental measurements. The REPs of T_{ad}, S_l, χ_{NO_2}, and χ_{CO_2} obtained using the POD/Kriging method are less than 5 %. This shows that the flame emission spectra have enough sensitivity to the gas properties. However, the REPs of χ_{NO} and χ_{CO}, are 17.7% and 52.1%, respectively. Prediction accuracy of χ_{CO} is degraded due to large deviations in data for the low-value range, and the prediction of χ_{NO} is inaccurate for the entire range.

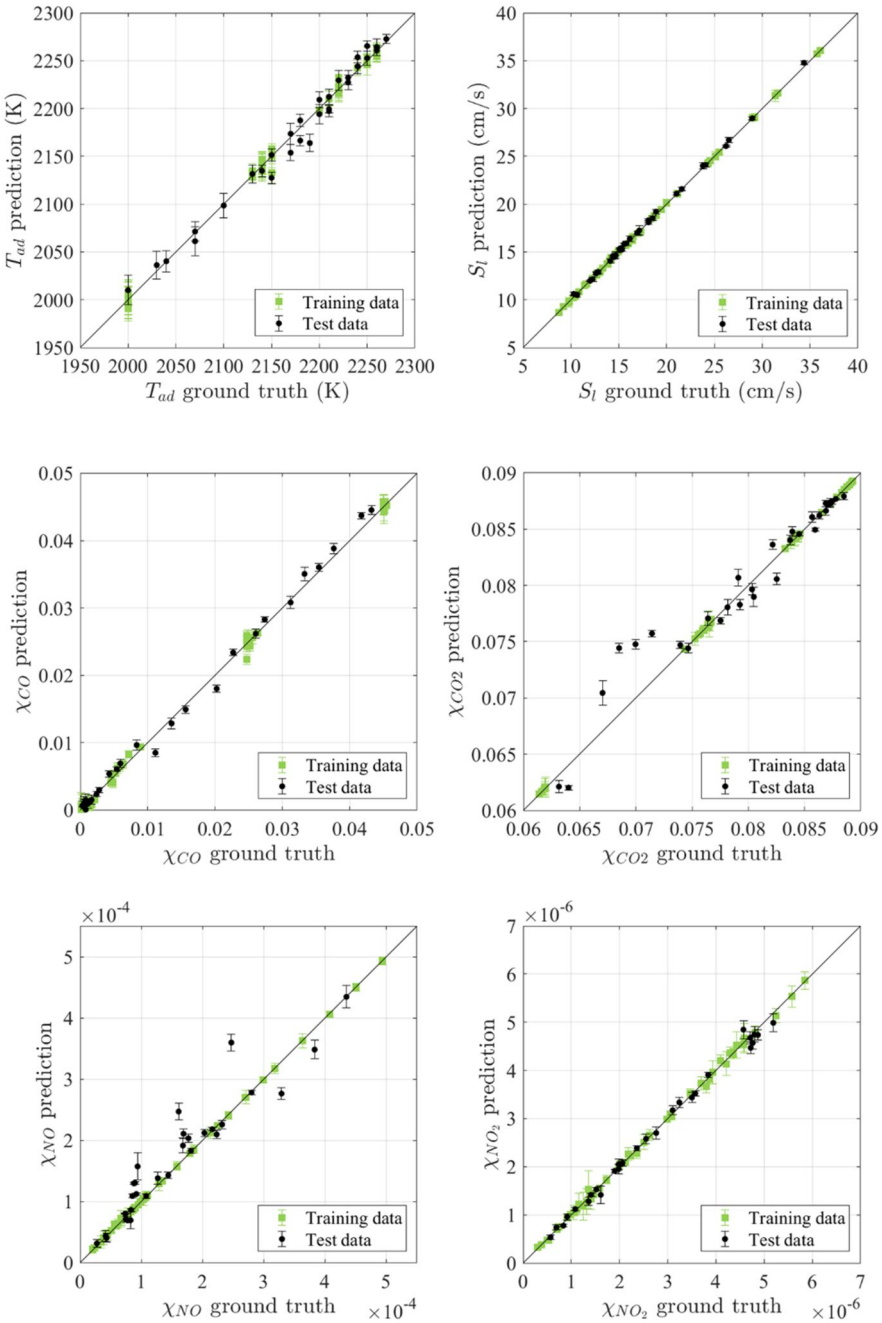

Figure 3.15 Predictions of adiabatic temperature (T_{ad}), flame speed (S_l) and concentration of NO, NO_2, CO, and CO_2 using POD/Kriging method

Table 3.3 Quantitative performance parameters for prediction accuracy and precision using POD/Kriging method

	REC	REP	RSD
Adiabatic temperature (T_{ad})	0.38	0.48	0.40
Flame speed (S_l)	1.20	1.27	1.24
NO concentration (χ_{NO})	5.27	17.7	6.43
NO_2 concentration (χ_{NO_2})	5.23	4.25	3.76
CO concentration (χ_{CO})	112	52.1	52.8
CO_2 concentration (χ_{CO_2})	0.35	1.73	0.54

CHAPTER 4. DEVELOPMENT OF DEEP LEARNING-BASED DENOISING

4.1 Overview of fast time-resolved FES

FES uses instantaneous flame emission so that it can provide measurements of gas properties in real-time. Also, a high acquisition rate of FES is achievable considering that the recent detection system has a high sampling rate (up to 10MHz) [20]. However, as discussed in section 2.1.3, a shorter exposure time with a higher sampling rate provides lower SNR signals, resulting in a degradation of accuracy and precision for predicting gas properties. Figure 4.1 illustrates the signal corrupted by noise due to short exposure times (0.05, 0.2, and 0.4 s) and its results of equivalence ratio prediction using the POD/Kriging calibration process. Since the distinct radical emission bands, which are sensitive to equivalence ratio, e.g. CH*, are overlapped by noise in low SNR signals, it can be difficult to predict the target properties. As a result, FES can be limited in its ability to achieve fast temporal resolution. The limitation can be avoided by applying an intensifier with a highly sensitive photon-detecting device. However, in practice, high-spec equipment can be expensive, bulky, and susceptible to vibration. Alternatively, pre-processing of the raw spectral data can suppress noise and restore information to achieve fast time-resolved FES. Particularly, the recent data-driven pre-processing methods can reduce

noise by utilizing global and local information in the dataset so long as the signal contains sufficient information to represent the characteristics.

In this chapter, a state-of-the-art deep learning-based denoising technique is developed specialized for denoising spectral signals to achieve fast time resolution in FES. In non-scientific fields, deep learning-based denoising has been developed for qualitative image processing [49, 53-60]. The use of denoising neural network architectures to perform quantitative reconstructions of a spectrum dataset requires an understanding of spectrum on both a global and local domain. A novel neural network architecture and regularization function are proposed to selectively eliminate the noise in spectral signals that increases with decreasing exposure time. To be more specific, a neural network architecture combining a reversible DU operator, along with deep CNN layers is introduced and this architecture is guided by a new loss function based on POD coefficients. Moreover, the demonstration of the proposed method on actual flame spectra is presented using a pair of low-SNR (LS) and high-SNR (HS) spectra, which are captured with short and long exposure times.

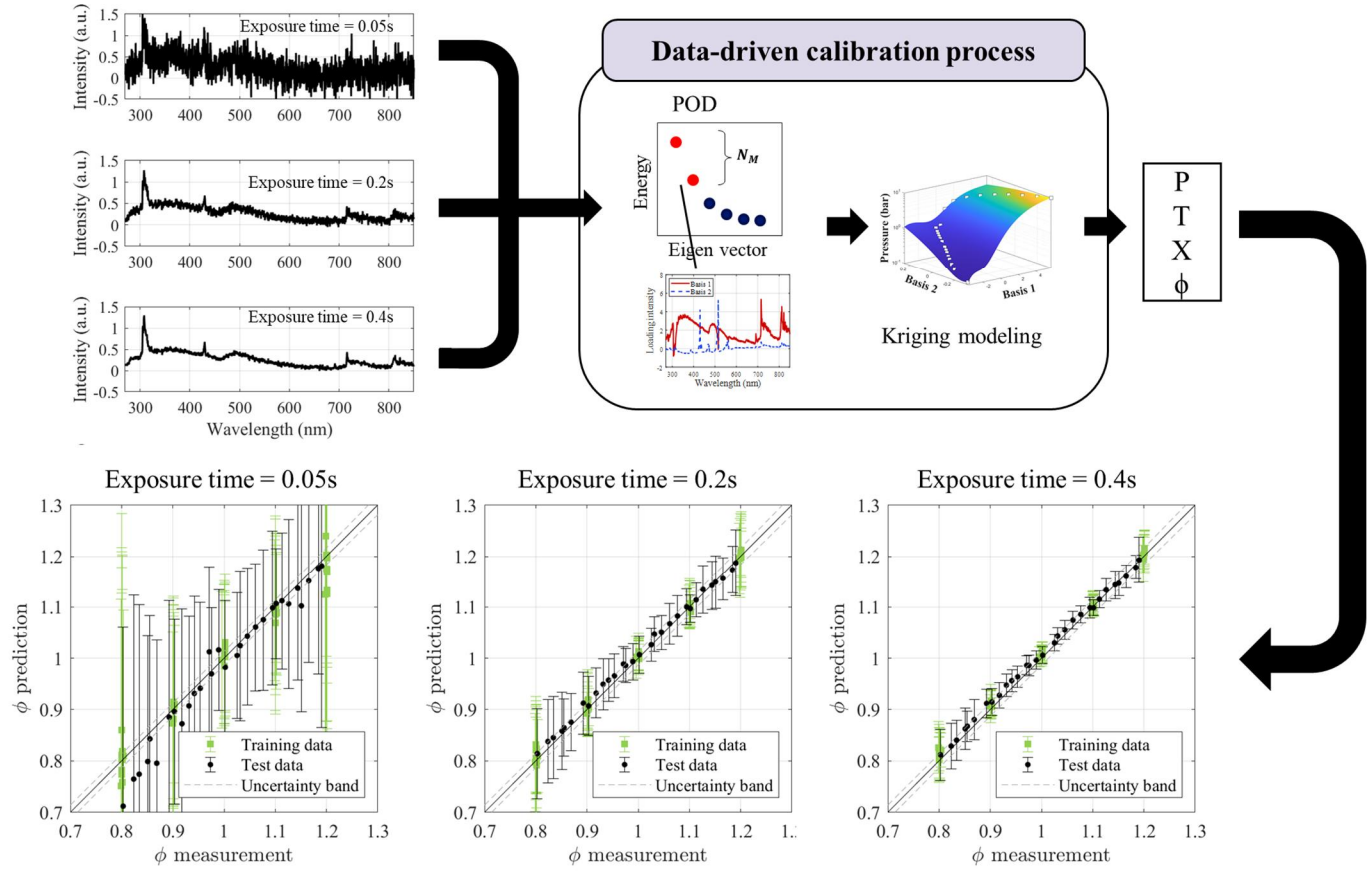

Figure 4.1 An illustration of degradation of prediction accuracy and precision with short exposure times

4.2 Deep learning-based denoising process

4.2.1 Training and test dataset

A data-driven machine learning model requires plenty of qualified and informative data to function efficiently and accurately. In this study, supervised learning using pairs of the actual noisy and clean datasets without noise modeling is selected since it provides high performance for handling the actual noise. The flame emission from a stable methane-air flat flame is used as the input (short exposure)-label (long exposure) pair $(x_i; y_i)_{i=1}^{N}$ for training the neural network model. The x_i and y_i values correspond to short-gated (0.2 s) and long-gated (2 s) spectrum data, respectively. The combination of input-label at the same gas property condition makes a large amount of paired data so that there are 80,000 data pairs used in the training and test neural network models: the combination of 100 low-SNR spectra and 10 high-SNR spectra for each of 80 different flame conditions in the range of ϕ (0.8 – 1.2) and pressure (1 – 10 bar). As indicated in Figure 3.2, the training data for 50 gas conditions are selected based on a full factorial design, and the test data for 30 gas conditions are sampled by the Latin hypercube sampling method. Therefore, the number of training and test data is 50,000 and 30,000, respectively.

As preprocessing, signals of flame emission are subtracted from dark spectra collected without flame, and then the signal is normalized by the average intensity of OH* bands between 306 and 313 nm, which is distinct in the overall gas property

range. Moreover, data augmentation is applied by the intensity of the signals of inputs, and labels which are randomly re-adjusted between 0.8× and 1.2× of the original signal intensity. Data augmentation improves the generalizability of the trained network and the performance of CNN [46, 64, 90]. Adjusting the signal intensity for data augmentation is only applied because flipping, rotating, and shearing the image can distort the information in the signal. Also, this random adjustment of signal intensity imposes the neural network a scale-invariance over a certain intensity range which can handle random fluctuations of total intensity in the dataset.

4.2.2 Neural network architecture

In this section, a neural network architecture for denoising the short-gated low-SNR spectra is proposed combining reversible DU operators and a plain CNN structure without residual learning or skip connection (see Figure 4.2). The low-SNR signal (LS) with a short exposure time is used as input to the neural network and the high-SNR signal (HS) with a long exposure time is used as label for supervision. The reversible down-sampling operator, also known as the sub-pixel convolution or pixel unshuffle, is used to improve the efficiency and receptive field of neural network models by reshaping the input signal vector of $W \times 1$ into a sub-signal tensor of $W/N_d \times N_d$ [55]. Here, W and N_d denote for the number of pixels in the input signal and the down-sampling parameter determining the number of sub-signals, respectively. The down-sampled sub-signals are then fed into the plain CNN. Each layer of the CNN is composed of three types of operations: Convolution (Conv), Batch Normalization (BN) [47], and Rectified Linear Units (ReLU) [46]. Specifically, the first layer consists of Conv + ReLU, the middle layers combine Conv + BN + ReLU, and the last layer is only Conv. According to reference denoising architectures [54, 55], 1) the number of channels (N_c) and kernel size of the filters (N_k) are the same for all layers, 2) the stride (filter movement) is one without pooling layers to minimize data loss, and 3) zero padding is implemented on the tensor before each CNN layer to maintain the component size of data. Then, the denoised sub-signals are operated to reconstruct the output signal which has the same

size as the input signal by the reversible up-sampling operator, which is the inverse operation of the down-sampling operator. As a result, the total neural network architecture is characterized by four hyperparameters: the down-sampling parameter (N_d), the depth of layer (N_l), the number of channels (N_c), and the kernel (filter) size (N_k). A combination of N_d = 1, N_l = 7, N_c = 32, and N_k =15 are chosen empirically as a baseline model for minimal complexity with acceptable performance. Finally, a loss function based on mean square error and POD coefficient error is calculated by comparing the output signal with the high-SNR signal (long-gated spectrum) which is paired with the input signal, i.e. captured under the same flame condition. The weight and bias parameters of the CNN architecture are optimized to minimize this loss function. A detailed description of the loss function is in section 4.2.3.

In the optimization process, the Adam optimizer [91] is used to train the neural network model for 100 epochs with a batch size of 128 samples. A linear warmup cosine annealing learning rate scheduler is used to prevent divergence and oscillation and accelerate the convergence rate. The parameters for the scheduler, the cycle step size (T_0), cycle step magnification (T_{mult}), max learning rate (η_{max}), linear warmup step size (T_{up}), and decrease rate of max learning rate by cycle (γ), are 50, 1, 0.005, 10, and 0.1, respectively [92]. The validation data is randomly selected from 10% of the training data (5000 data pairs in 5 cases) to check the overfitting of the model.

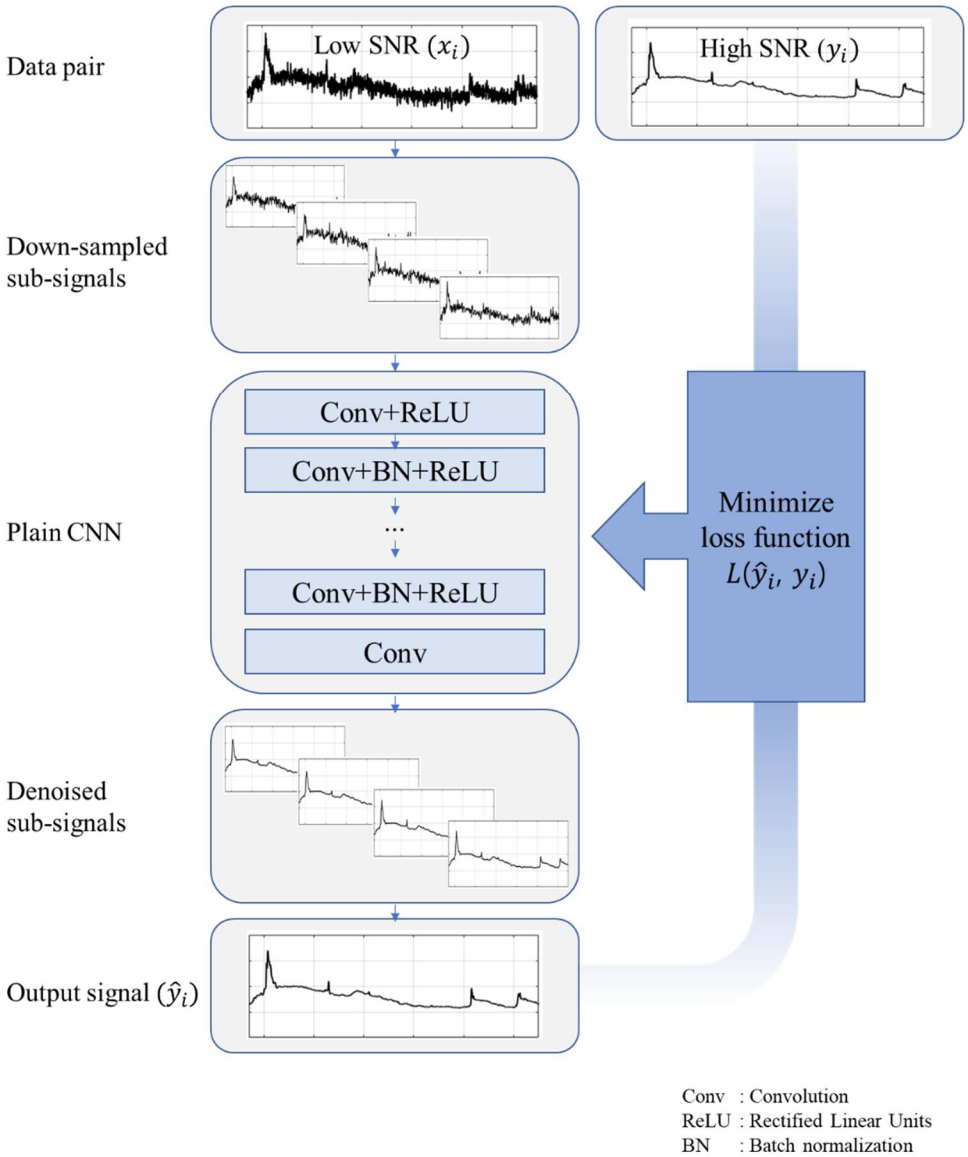

Figure 4.2 A schematic diagram of the proposed denoising neural network architecture

The DU operator is illustrated in Figure 4.3 by comparing a plain CNN and the proposed architecture combining plain CNN and DU operator, which is denoted as DU + CNN. The role of the DU operator is to expand the receptive field and to reduce the number of convolution operations and memory usage [55]. The receptive field is defined as the number of input pixels involved in generating one output pixel, which indicates how wide a range of information is used to reconstruct one data point in the output data. Utilizing information from a wide range of input signals with a wide receptive field offers significant advantages for denoising and reconstructing signals with strong noise. Below is an equation for the receptive field of the proposed CNN architecture:

$$\text{Receptive field} = N_d \times (N_l \times (N_k - 1) + 1) \tag{4.1}$$

The receptive field can be widened by increasing N_l, N_k, and N_d with the same order of magnitude, whereas N_c does not affect the receptive field.

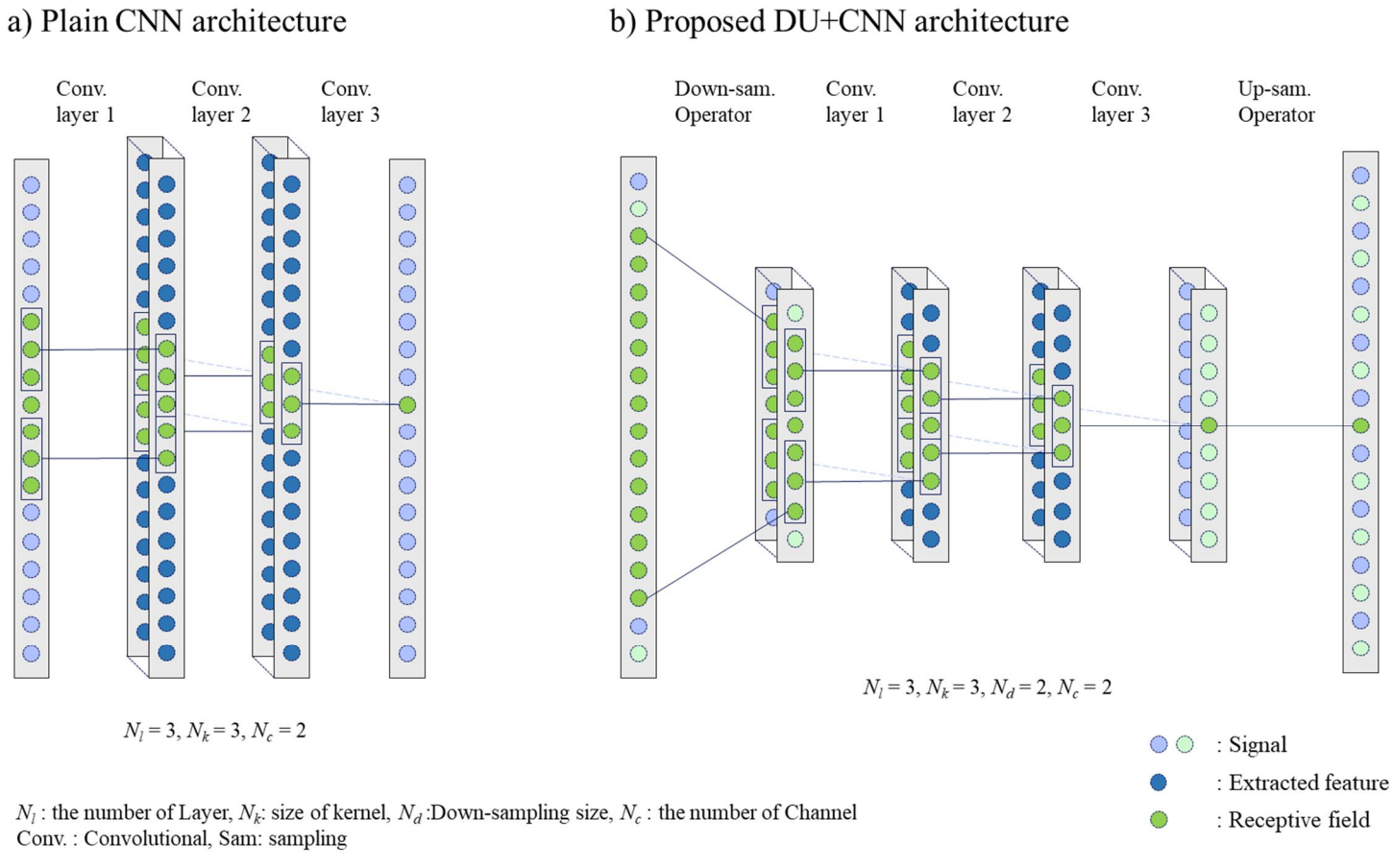

Figure 4.3 An illustration of the receptive fields of neural network architectures and the data size of each layer

4.2.3 Loss function

To enhance the accuracy of the calibration process and prevent data overfitting, we propose a loss function that combines the MSE loss and a regularization term defined as the squared L2 norm of POD coefficients, called the POD loss. The formulation of the loss function is given below (equation 4.2):

$$L = \frac{1}{N}\sum_{i=1}^{N}[(1-\alpha)\|\hat{y_i} - y_i\|_2^2 + \alpha\|POD(\hat{y_i}) - POD(y_i)\|_2^2] \qquad (4.2)$$

where L, N, α, $\hat{y_i}$, y_i, $POD(\hat{y_i})$, and $POD(y_i)$ are the loss function, the number of total data pairs, a blending parameter (set to be 0.1 here), an output signal, the corresponding label spectrum (high-SNR spectrum), and min-max normalized POD coefficients of $\hat{y_i}$ and y_i, respectively. The first term is MSE loss commonly used in the image denoising process and the second term is POD loss defined as the squared L2 norm of the POD coefficient difference. The POD loss is calculated using five POD bases from averaged label data in each gas properties condition (50 cases), considering total energy content (99.7%) and sensitivity to gas properties based on GSA in Chapter 3. Moreover, the five POD coefficients are normalized by the min-max of each coefficient to set the same weight on each basis in the loss function. This is because the variance of each POD coefficient rapidly decreases with increasing basis order, whereas the sensitivity to each gas property does not directly follow the basis order (energy contents), as shown in Figure 3.7. The POD can extract

property-sensitive and high-dimensional spectrums (the same dimension as the input spectrum). POD coefficients represent the weight of each POD basis that composes the spectrum (e.g., $\hat{y}_i$ and y_i); the dot product between the POD coefficients and the POD bases results in the reconstruction of the spectrum. Therefore, the L2 norm of POD coefficients indicates global similarity, particularly regarding the property-sensitive parts of the spectrum, which is important for improving the performance of the denoising CNN.

4.3 Results of data processing

4.3.1 Denoising with the proposed CNN

Figure 4.4 illustrates the denoising capability comparison of conventional filters (low-pass filter and Gaussian filter) and deep learning-based denoising with low and high SNR signals. The chemiluminescence spectra acquired for the two exposure times (0.2 and 2 s), were denoted as LS and HS, respectively, as shown in Figure 4.4 (a) and (f). The presented spectra of LS and HS were obtained from the test dataset that was not used to train the model so the spectra are supposed to be unknown flame emission signals in arbitrary gas conditions. There are distinct spectral features in the HS spectrum that are characteristic of excited molecules including OH* at 306.4 nm, CH* at 431.4 nm, C_2* swan bands at 517 nm, and H_2O* at 700 – 850 nm. The intensity and shape of the spectral features are highly dependent upon the gas

properties in the combustion reaction zone. For example, CH* and C_2* increase in fuel-rich flame conditions, and H_2O* is elevated under high-pressure conditions. Therefore, some relatively weak characteristic spectral features barely appear in LS signals, such as CH* and C_2* at lean conditions and H_2O* at low-pressure conditions.

Figure 4.4 (b) and (c) present the processed signal by the conventional filtering method, i.e., low-pass filter and Gaussian filter. The conventional filtering method considers a high-frequency signal as noise and selectively attenuates the high-frequency signal. Therefore, if the parameters of these conventional filters are not sufficient to suppress the noise floor, denoising preprocessing is not sufficient to improve the SNR. Or in the opposite case, if the filters excessively suppress the high-frequency signal, the peak signals are blurred. Moreover, The filters not only suppress relatively weak characteristic spectral features but also obscure high-intensity peak signals.

Figure 4.4 (d) and (e) present the outputs of a plain CNN (N_l = 7, N_c = 32, and N_k = 15) without DU operator trained with MSE loss and the proposed DU + CNN (N_l = 7, N_c = 32, N_k = 15, and N_d = 16) trained using the combination of MSE and POD loss, which are denoted as plain CNN and DU + CNN / POD loss, respectively. Spectra used for training and validation were the same for both models. A comparison of both signals processed by CNN architectures and filtered signals by low-pass and Gaussian filters clearly demonstrates that CNN architectures are more capable of significantly reducing the noise level in the spectra than the low-

pass and Gaussian filters. Nevertheless, the relatively weak characteristic spectral features, such as CH* at lean conditions and H_2O* emission bands, denoised by the plain CNN model differ from those of the corresponding HS spectra that are close to the ground truth signal. Therefore, the gas property prediction would be inaccurate using denoised LS with the plain CNN model because the CH* and C_2* bands are highly sensitive to the fuel concentration (ϕ) and the H_2O* bands are the most prominent pressure indicator. The spectra denoised by the DU + CNN / POD loss, however, show good agreement with the HS spectra in most details. The noise from the input LS spectra could be successfully suppressed without sacrificing critical spectral features under various gas properties regardless of the noise level. We conjecture that this is due to proper down-sampling, which results in a larger receptive field, the number of input pixels involved in producing a given output pixel, and the regularization of the CNN architecture through POD loss. Thus, each pixel in the output signal is denoised and reconstructed based on the global spectral features of the input signal with a wide receptive field and the POD coefficients of each basis mode. In this regard, the successful denoising process is enabled by decoupling the property-sensitive spectral features from the low SNR signals even though the noise level changes with the randomly re-adjusted overall signal intensity. This will be further discussed in more detail in Section 4.3.2.

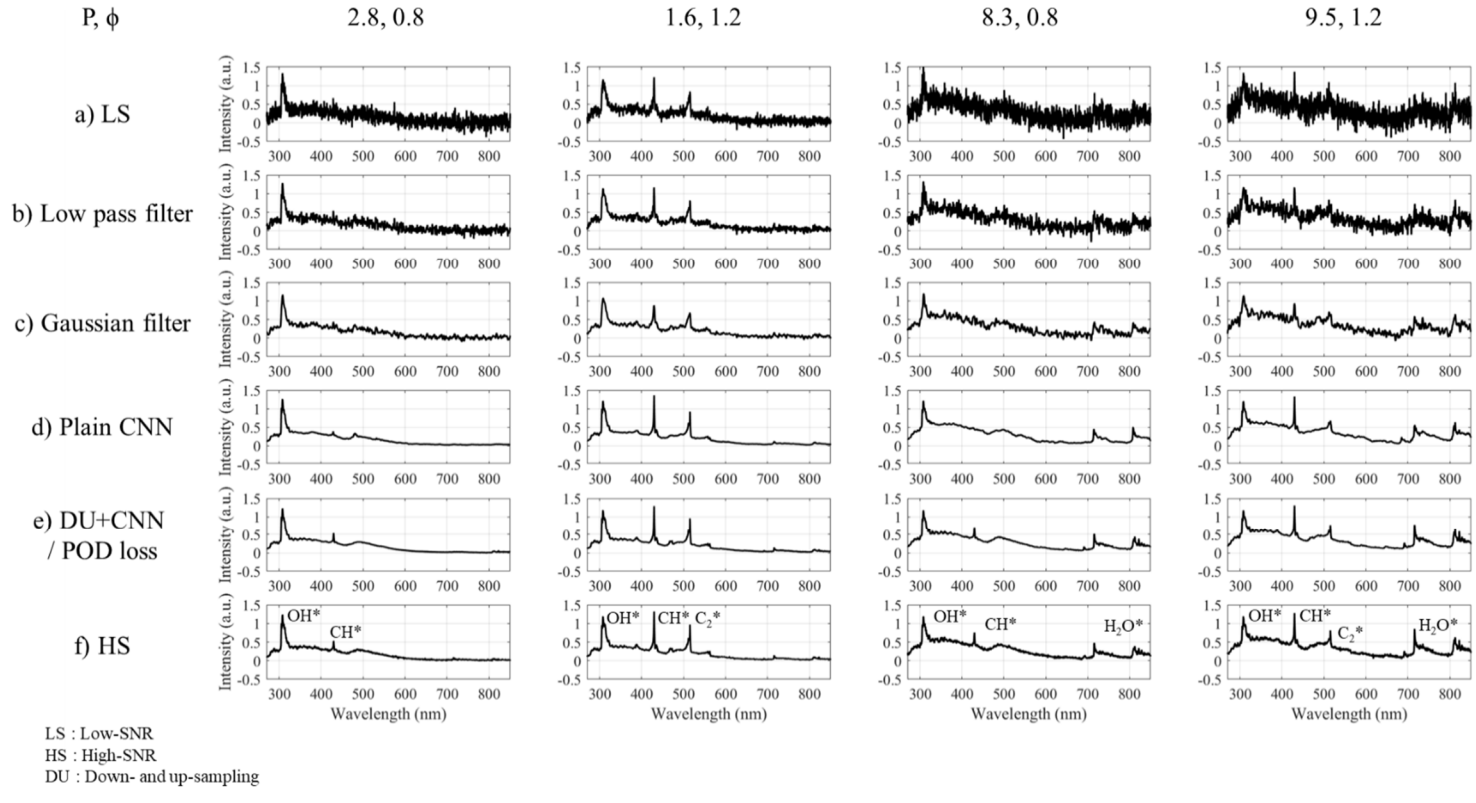

Figure 4.4 Comparison of flame emission spectra captured for 0.2 s (Low-SNR, LS) and 2 s (High-SNR, HS) exposures, and the LS spectra processed by low-pass filter, Gaussian filter, plain CNN and DU + CNN / POD loss

Figure 4.5 shows the power spectrum analysis of (a) LS and (f) HS signals and the processed LS signal using (b) low-pass filter, (c) Gaussian filter, and (d)(e) two neural networks. The power spectrum is calculated by the Fourier transform of the spectrum signals and the magnitude of the power spectrum represents the intensity of the periodic wavelength spatial frequency. As shown in Figure 4.5 (b) and (c), the conventional filters, i.e. low-pass filter and Gaussian filter, exhibit suppression of signal magnitude in the wavelength spatial high-frequency region, indicating information loss at a high frequency based on the power spectrum of corresponding HS signals. Since the sharp peak signals, which are sensitive indicators of gas properties, are also in the wavelength spatial high-frequency range, the accuracy of gas characteristics prediction can be compromised. On the other hand, as shown in Figure 4.5 (d) and (e), the neural network denoising preserves sharp peak signals by selectively reducing noise and reconstructing signals, rather than simply suppressing the magnitude at high frequencies in the power spectrum. Therefore, the neural network denoiser suppresses noise while preventing information loss in peak signals such as OH*, CH*, and H_2O* which are sensitive indicators of the target gas properties.

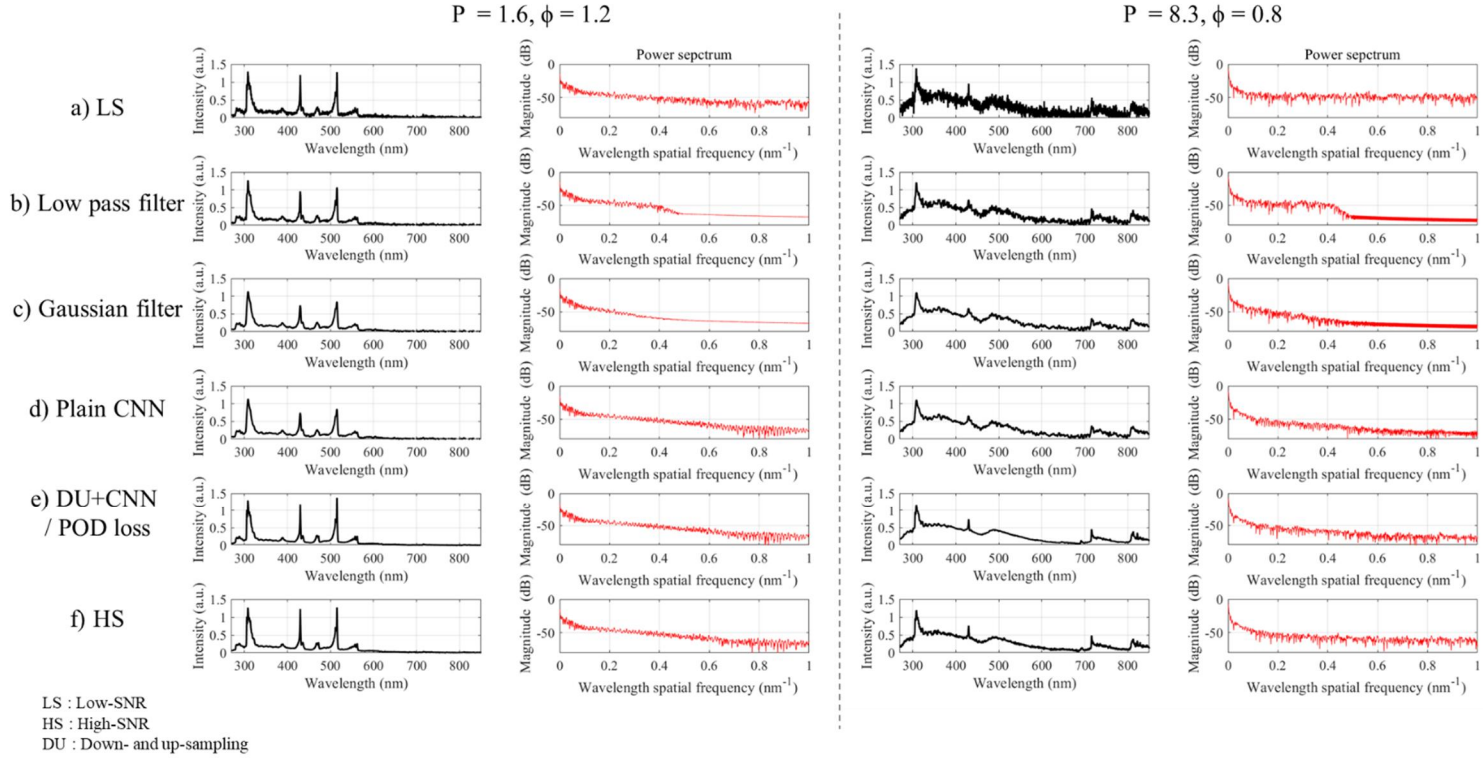

Figure 4.5 Comparison of flame emission spectra and power spectrum captured for 0.2 s (Low-SNR, LS) and 2 s (High-SNR, HS) exposures, and the LS spectra processed by low-pass filter, Gaussian filter, plain CNN, and DU + CNN / POD loss

4.3.2 Neural network architecture and loss function

Figure 4.4 (d) and (e) show the importance of deep learning-based denoising architecture and the regularization method because the architecture and the regularization method determine the capacity and performance of the model. The architecture is specified by the hyperparameter setting and the regularization method is determined by the configuration of the loss function. The neural network with sixty different architectures based on hyperparameter pairs which are the combinations of N_k (3, 7, 15, 25, and 45) and N_d (1, 16), and N_l (2, 3, 5, 7, 11, and 15). When N_d equals one, the DU operator is an identity operation so the architecture is the plain CNN. These sixty architectures are trained with different loss functions, i.e. MSE loss and MSE + POD loss. To compare the different neural network models combined with each of the two loss functions, the performance measures of denoising results are estimated quantitatively by the average relative error of the area (REA) defined as the following equation:

$$REA_{M^*}\ (\%) = \frac{100}{N_{test}} \sum_{i=1}^{N_{test}} \left[\frac{1}{N_{i,shot}} \sum_{j=1}^{N_{i,shot}} \left| \frac{Area(M^*\ in\ \hat{y}_{i,j}) - Area(M^*\ in\ y_{i,j})}{Area(M^*\ in\ y_{i,j})} \right| \right] \quad (4.3)$$

Where M*, N_{test}, $N_{i,shot}$, $\hat{y}_{i,j}$, $y_{i,j}$, and $Area(M^*\ in\ \hat{y}_{i,j})$ is one of the excited molecules emitting local spectral features, the total number of test cases in the different conditions, the number of spectral shots in the ith condition, denoised low

SNR spectra, high SNR spectra, and spectral area of M* in $\hat{y}_{i,j}$ calculated in the same way presented in section 2.3, respectively. M* is chosen as OH* (306 – 338 nm), CH* (420 – 443 nm), and C_2* (498 – 522 nm), H_2O* (713 – 791 nm), and broadband (BB, 270 – 650 nm) by following section 2.3. Additionally, $Area(M^* \ in \ \hat{y}_{i,j})$ is calculated using the POD coefficient vector of the $\hat{y}_{i,j}$ multiplied by the area of M^* in each POD basis and the average spectra of all snapshots.

In this study, as long as the neural network is trainable, it is observed that the denoising performance improvs as N_l, N_k, and N_d, increase, resulting in a wider receptive field. Therefore, one critical parameter that determines the performance of deep learning architectures is the receptive field of neural networks. Figure 4.6 (a) and (b) describe the trends of each denoising performance parameter, REA of OH*, CH*, C_2*, H_2O*, and BB as functions of the receptive field with different neural network architecture regularized by MSE loss. As shown in Figure 4.6 (a), REAs of OH*, CH*, and BB are nearly constant with the receptive field under 100 but rapidly decrease until the receptive field reaches the pixel number of the input spectrum (W, 1696 × 1), and both the three REA indicators approach the minima at around 2 × W. Implementing the DU operator increases the receptive field by N_d times, so the performances of DU + CNNs outperform those of plain CNNs. Notably, each output pixel is constructed by observing all the input pixels when the receptive field is 2 × W; therefore, further increase in the receptive field beyond 2 × W does not have

much benefit in improving model performance. The error trend in Figure 4.6 (b) for C_2* and H_2O* is similar in that the error decreases as the receptive field increases, but the magnitude of the error is large because these local spectral features are very weak under certain conditions; C_2* disappears under lean fuel conditions and H_2O* cannot exist under low pressures. In conclusion, the receptive field of neural network architectures should be set between W and 2 × W to maximize denoising performance, or close to W to reduce model complexity with acceptable performance.

According to previous studies on denoising CNN architectures for general 2D images, the optimal receptive field size has been discussed between 35 x 35 and 61 x 61 in reference [55]. The flame emission spectrum, however, has an important characteristic that distinguishes it from typical 2D images: all pixels are closely related, not just those closest to each other, but also those far apart. This is because the entire range of spectra is affected by variations in gas properties. For example, 1) Increasing fuel concentration will prompt multiple molecular bands that are far separated in the spectrum at the same time such as OH*, CH*, C_2*, and BB. 2) As P increases, the molecular emission band broadens and the peak intensity diminishes. 3) Broadband background emissions become stronger with increasing gas density and CO_2 concentration. In summary, expanding the receptive field to exploit the global contextual information of the emission spectrum can improve the denoising performance while keeping it below 2 × W, because the pixels in the emission spectrum are all related (unlike typical 2D images).

Figure 4.7 presents the denoising performance of neural network architecture with two different loss functions: MSE loss and MSE + POD loss. As shown in Figure 4.7 (a) and (b), the REAs of OH*, CH*, BB, C_2*, and H_2O* for neural network architecture with MSE + POD loss have similar trends to the REAs with MSE loss. It is observed that denoising performance improves as the receptive field increases regardless of the configuration of the loss functions. Furthermore, the neural networks trained with MSE + POD loss show better performance for reconstructing the area of OH*, CH*, BB, C_2*, and H_2O* compared to the models regulated by MSE loss. For example, when training neural networks with MSE + POD loss, the band area of CH*, which is sensitive to the equivalence ratio, shows a maximum error reduction of 30% depending on the neural network architecture, and the minimum error with MSE + POD loss decreased by 7% compared to the error with MSE loss. Recall that POD decomposes spectral data into dominant bases in the entire spectral space correlated with gas properties. Therefore, the loss function, including the POD loss, can preserve global features of the LS signal by decoupling random noise from signals sensitive to gas properties. In contrast, the conventional loss function simply considers the mean square error of the spectra, regardless of the sensitivity of the spectral profile to the properties of interest. All REAs of each molecular band emission for the combination of different neural network architectures and loss functions are summarized in Figure 4.8, and the table is shown in tables A.2 and A.3 in Appendix A.2 and A.3.

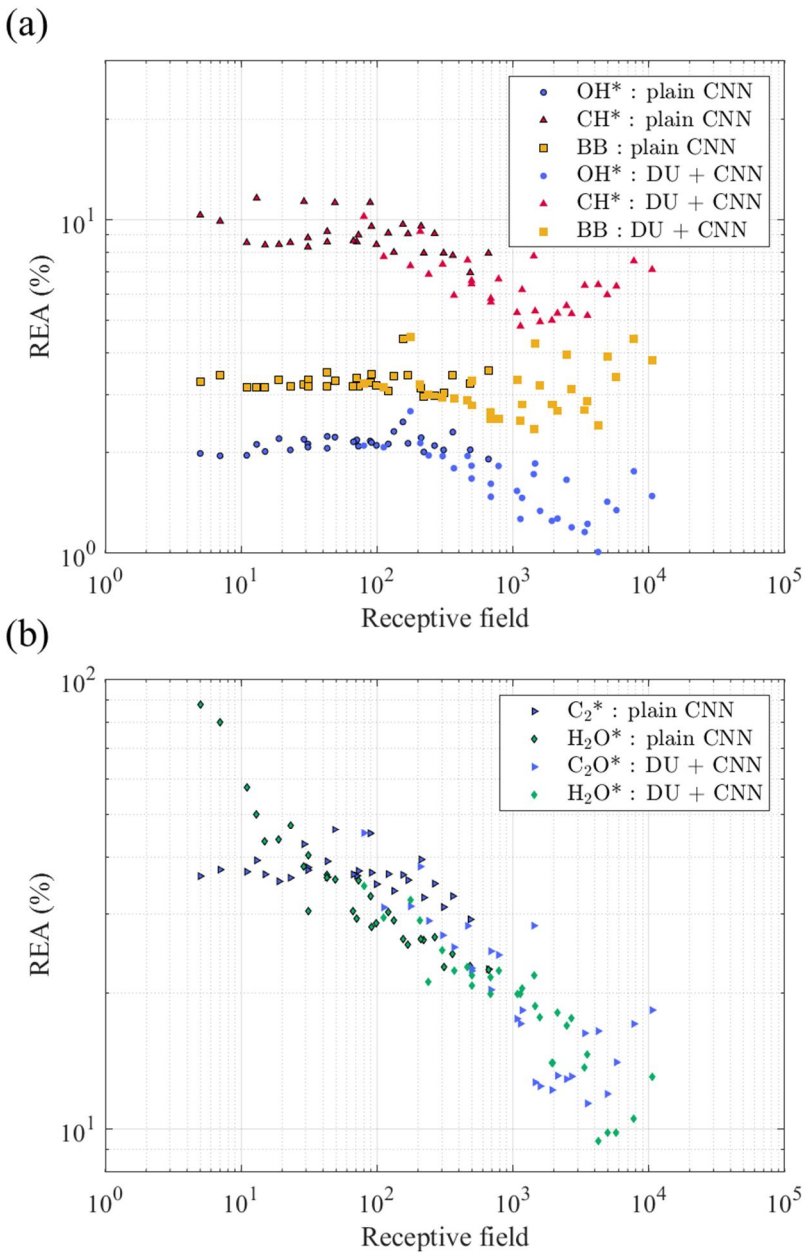

Figure 4.6 REA of each band emission versus the receptive fields of plain CNN (N_d = 1) and DU + CNN (N_d = 16) trained by MSE loss

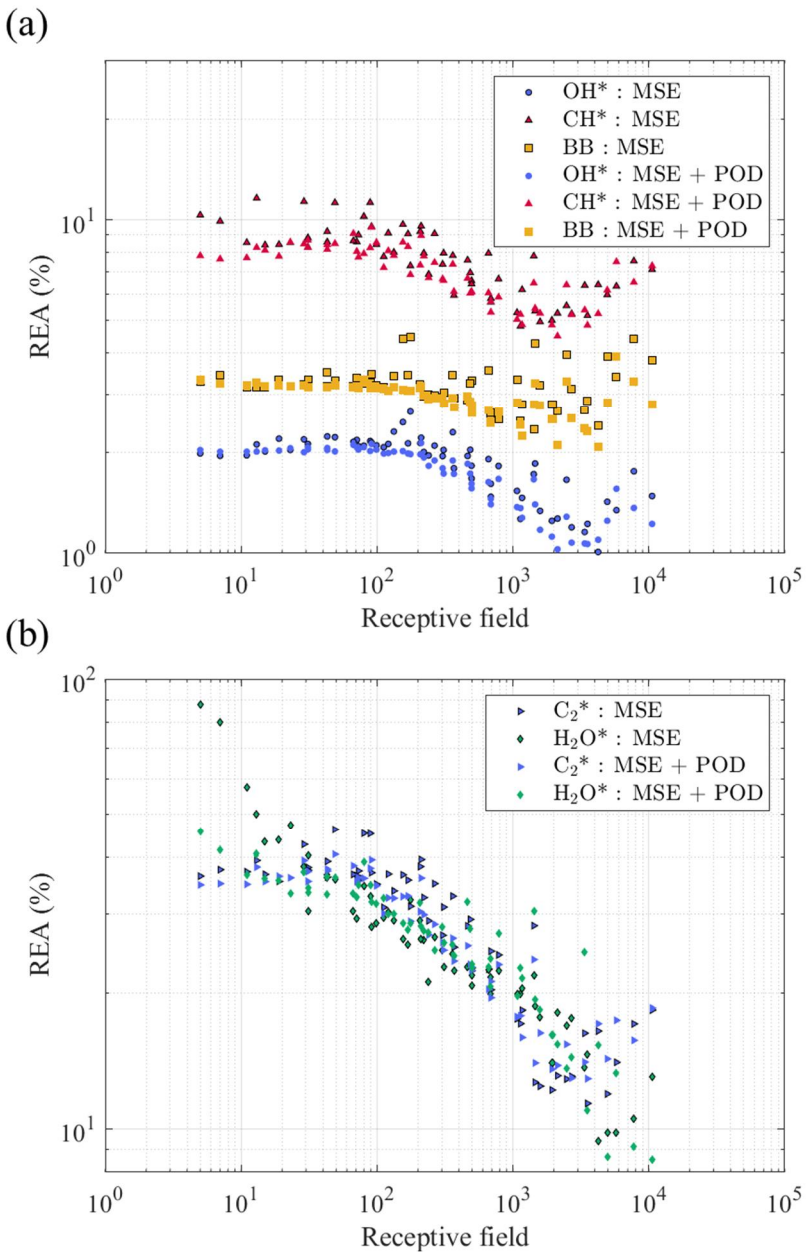

Figure 4.7 REA of each band emission versus the receptive fields of plain CNN (N_d = 1) and DU + CNN (N_d = 16) trained by MSE and POD loss

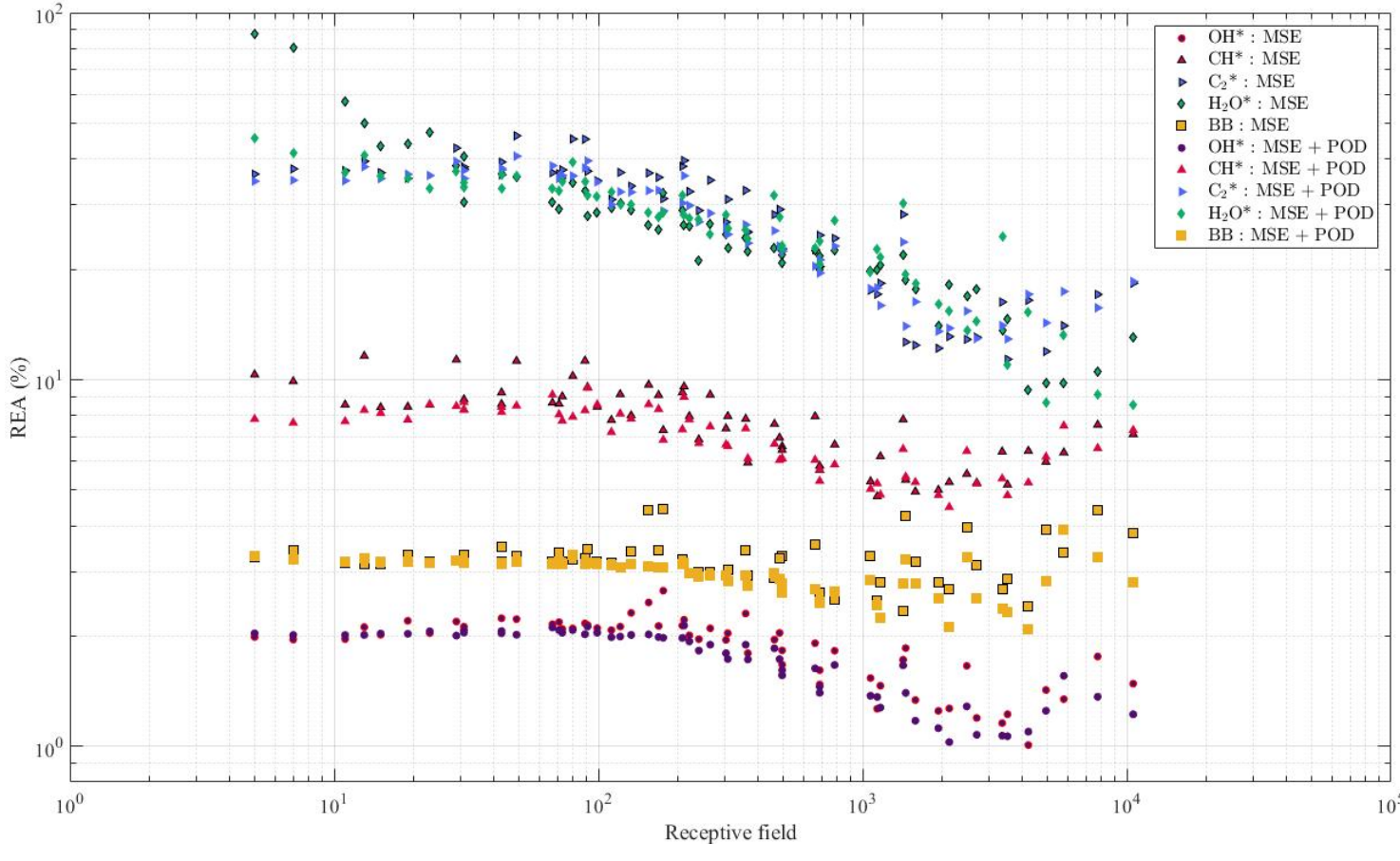

Figure 4.8 REA for each local emission feature versus the receptive fields trained by MSE loss and POD loss

4.3.3 Computational Efficiency

The computational efficiency of a deep learning-based method is one of the critical aspects that is required for the real-time denoising process of fast measurements. The performance of the deep learning-based denoising method can be improved by increasing the receptive field as summarized in Figure 4.8; however, increasing N_l and N_k to obtain a large receptive field introduces neural network computational complexity, increasing forward calculation time (running time shown in Figure 4.9) and limiting real-time gas property measurements. In contrast, implementing the DU operator to increase the receptive field by a factor of N_d accelerates the running and training of a neural network model. This is because using the DU operator makes the data size of the extracted features decrease, resulting in reducing the number of convolution operations and memory usage [55].

Figure 4.9 and Figure 4.10 present the computation time of the proposed CNN model in a Python environment. These results were obtained on a personal computer with NVIDIA GeForce RTX 3090, AMD Ryzen 5 2600X, and 32GB of RAM. The running time in Figure 4.9 is calculated by averaging the time using 5,000 inputs with a batch size of 1. And the training time in Figure 4.10 is evaluated by the time used to train a model for 100 iterations. The DU operator accelerates computations under a given receptive field as shown in Figure 4.9 and Figure 4.10. Given that the same order of expanding receptive field results from raising N_d, N_l or N_k (Equation 4.1), increasing N_d to widen the receptive field of a neural network is

much more cost-effective than increasing N_k or N_l. This is because the DU operator (N_d > 1) reconstructs the input pixels into sub-signals which in turn reduces the convolution operation range and thus the computation time. Furthermore, the number of training weights and bias parameters (N_p) calculated by Equation 4.4 is always smaller for increasing N_d than for increasing N_k or N_l for a given receptive field.

$$\# \ of \quad paramter \ (N_p) \ = \\ (N_l - 2) \times (N_c^2 N_k + N_c) + 2N_d N_c N_k + (N_c + N_d) \tag{4.4}$$

N_p increases with all three parameters: N_l, N_k, and N_d. However, N_l and N_k increments N_p by N_c^2 (>> N_c). So N_d has less impact on the computational cost than N_l and N_k as presented in Figure 4.11.

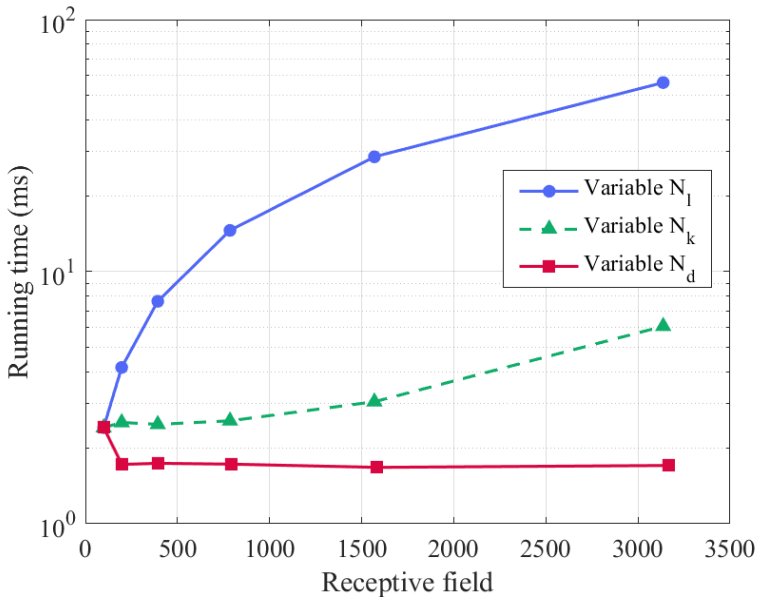

Figure 4.9 Running time versus the receptive field with increasing three parameters (N_l, N_k, and N_d)

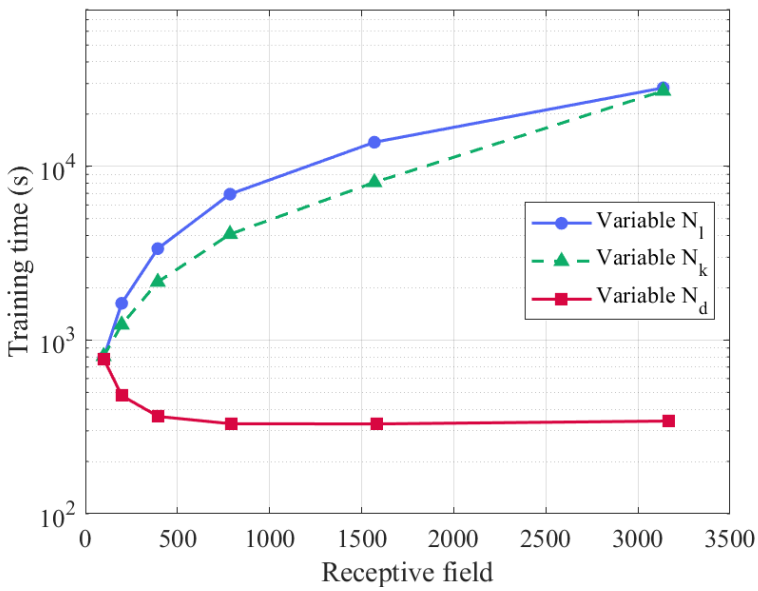

Figure 4.10 Training time versus the receptive field with increasing three parameters (N_l, N_k, and N_d)

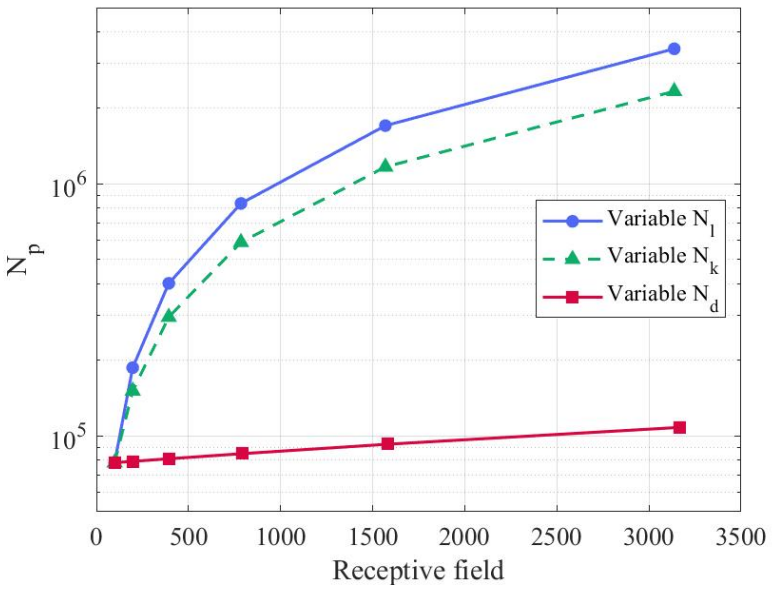

Figure 4.11 The number of trainable parameters versus the receptive field with increasing three parameters (N_l, N_k, and N_d)

CHAPTER 5. FRAMEWORK FOR FAST TIME-RESOLVED AND HIGH ACCURACY FES

5.1 Overview of proposed framework

The proposed fast time-resolved and high-accuracy FES combining the data-driven calibration process and deep learning-based denoising method are summarized in Figure 5.1. The proposed FES consists of a calibration process for training and validating a model and a prediction procedure for the trained model to estimate gas properties from an arbitrary spectrum. The calibration process is divided into three stages: 1) Acquire training data, 2) Map data, and 3) Train CNN. Then, the prediction procedure achieves measurements under arbitrary conditions: 4) Test data acquisition. The following is a detailed description of each of the four parts.

1) Pairs of high-SNR (long exposure) and low-SNR (short exposure) spectra are collected in steady-state calibration experiments to train and validate the model. 2) The averaged high-SNR spectra are used to map the high-SNR spectrum data to the gas properties of interest, e.g., pressure (P) and equivalence ratio (ϕ). Any calibration techniques, e.g., the conventional one-to-one calibration functions of emission band intensity ratios, PLS-R[40], and ANN [43], can be used. In this study, a ROM based on POD and the Kriging model is adopted because of its high accuracy and precision as presented in Chapter 3. The ROM is capable of accurately predicting multiple gas

properties using property-sensitive spectrum features decomposed by POD bases. In the next stage, 3) a denoising CNN is trained on the high-SNR (label) and low-SNR (input) spectrum pairs to produce a denoised spectrum output generated from a short-gated spectrum of low-SNR (input). The spectral datasets are divided into training data and validation data for checking the under-fitting or over-fitting of the calibration model. Lastly, 4) arbitrary short-gated flame emission spectrum data is collected to predict multiple gas properties with fast time-resolution and high accuracy using trained CNN and ROM. Figure 5.2 presents details on prediction procedures of the fast time-resolved and high accuracy FES. A low SNR short-gated spectrum from the target flame is processed with denoising and the corresponding gas properties are predicted by mapping function (Kriging model in this study) from the POD coefficient vector of the processed spectrum.

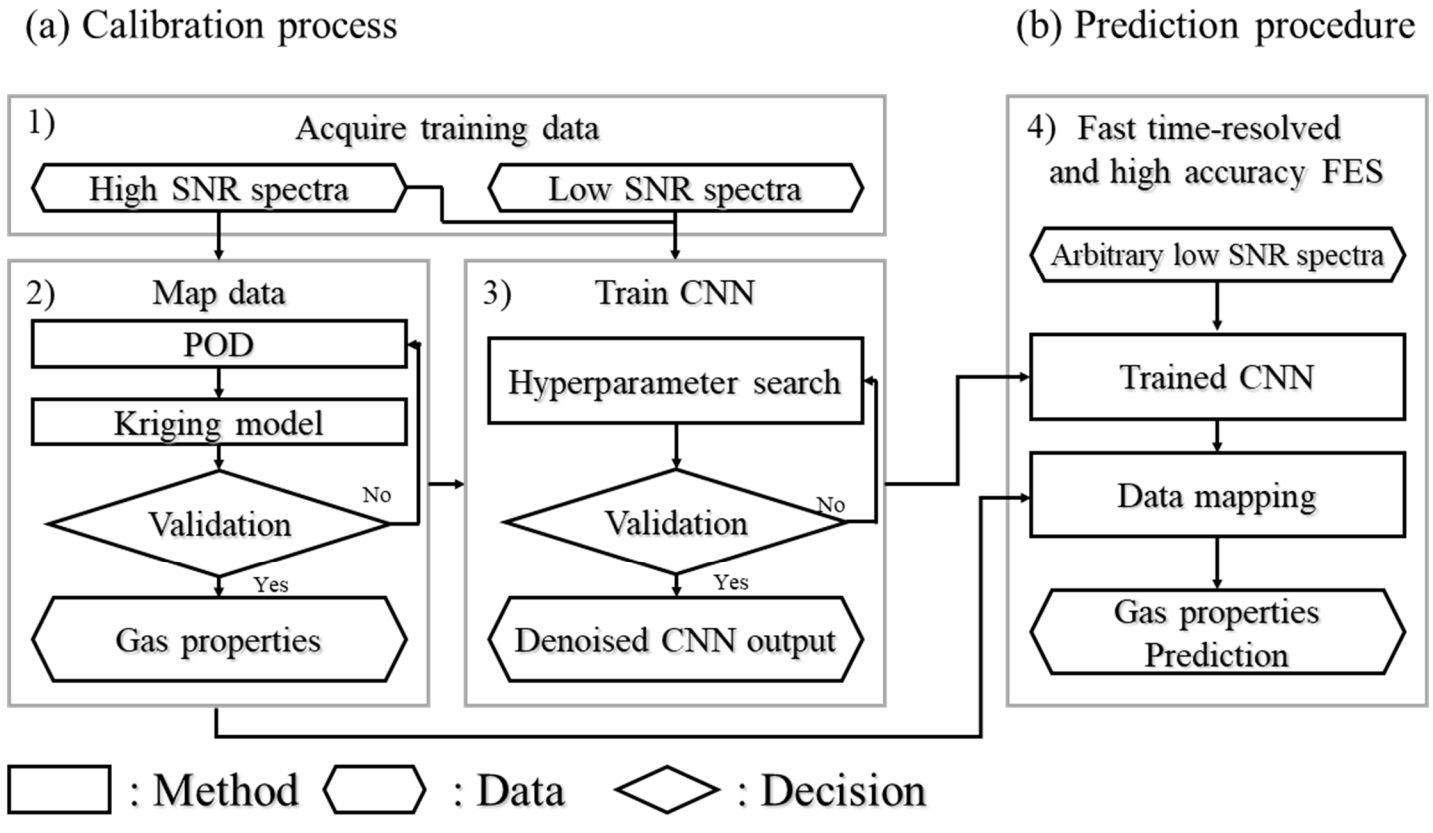

Figure 5.1 A flowchart for (a) calibration process and (b) prediction procedure

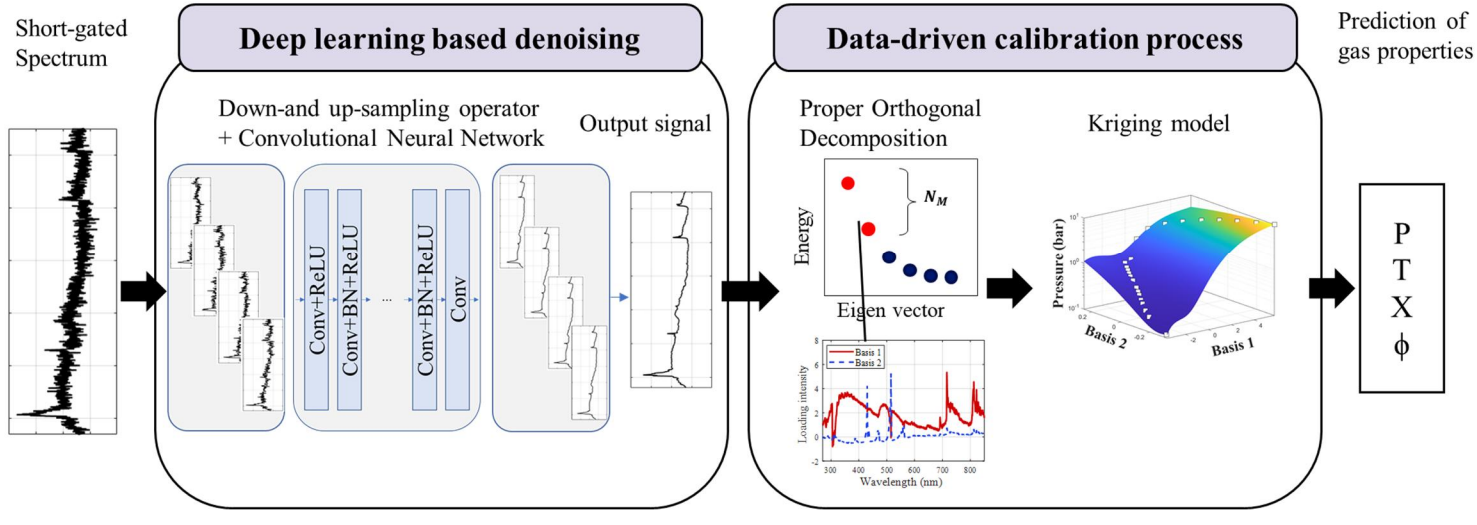

Figure 5.2 An illustration of fast time-resolved and high-accuracy FES for gas property prediction

5.2 Fast time-resolved and high accuracy FES

5.2.1 Calibration and prediction of gas properties

The proposed FES method is applied to the spectral dataset. As shown in Figure 5.3 (a), (b), and (c), to evaluate the performance of the proposed framework quantitatively, gas properties (P and ϕ) are predicted by calibrating 1) raw LS spectrum signals (without denoising), and the emission spectra denoised-reconstructed by 2) a plain CNN (N_l = 7, N_c = 32, N_k = 15, and α = 0), and 3) a DU + CNN / POD loss architectures (N_l = 7, N_c = 32, N_k = 15, N_d = 16, and α = 0.1), respectively. The x-axis in Figure 5.3. is ground truth values measured by high-accuracy sensors, whereas the y-axis represents predictions based on three sets of spectra: (a) LS without denoising, (b) denoised LS by the plain CNN, and (c) denoised LS by the DU + CNN / POD loss. The error bars present standard deviations of the gas property predictions obtained from 100 short-gated LS signals. The uncertainty bands of sensor-measured P and ϕ are also shown (gray dotted lines) which are calculated considering uncertainty propagation based on Taylor series expansions, as presented in section 2.1.2.

Given that the plain CNN effectively removed noise in the LS spectrum signals as shown in Figure 4.4, the accuracy of the gas property prediction using the preprocessed signals from the plain CNN (Figure 5.3 (b)) is not significantly improved compared to the prediction using the LS signals without the denoising

CNN process (Figure 5.3 (a)). In contrast, the DU + CNN / POD loss model impressively improves the accuracy and precision of the property prediction, P and ϕ in Figure 5.3 (c). This is because DU + CNN / POD loss can effectively suppress the noise from the LS spectrum signals with minimal information loss of local characteristic features resulting from utilizing the DU operator and POD loss, as confirmed in Figure 4.4. In other words, multiple molecular bands (OH*, CH*, C_2*, and H_2O*) distributed over a wide range are interconnected with varied gas properties. With the wider receptive field of down-sampled signals and regularized training by adding POD loss, these global molecular band features can be preserved, improving the accuracy of gas property prediction. In comparison, the receptive field of the DU + CNN is 16 times larger than that of the plain CNN.

Table 5.1 presents the performance of gas property prediction based on LS, plain CNN, and DU + CNN / POD loss. The REC, REP, and RSD of P and ϕ are tabulated, which are measures to evaluate the calibration accuracy of training data, the prediction accuracy of test data, and the prediction precision of test data, respectively. The accuracy and precision of gas properties prediction using DU + CNN / POD loss outperform LS and plain CNN. Particularly, the accuracy (REP) and precision (RSD) of the ϕ-prediction are 1.5% and 1.6%, respectively, which are comparable to the sensor measurement uncertainty.

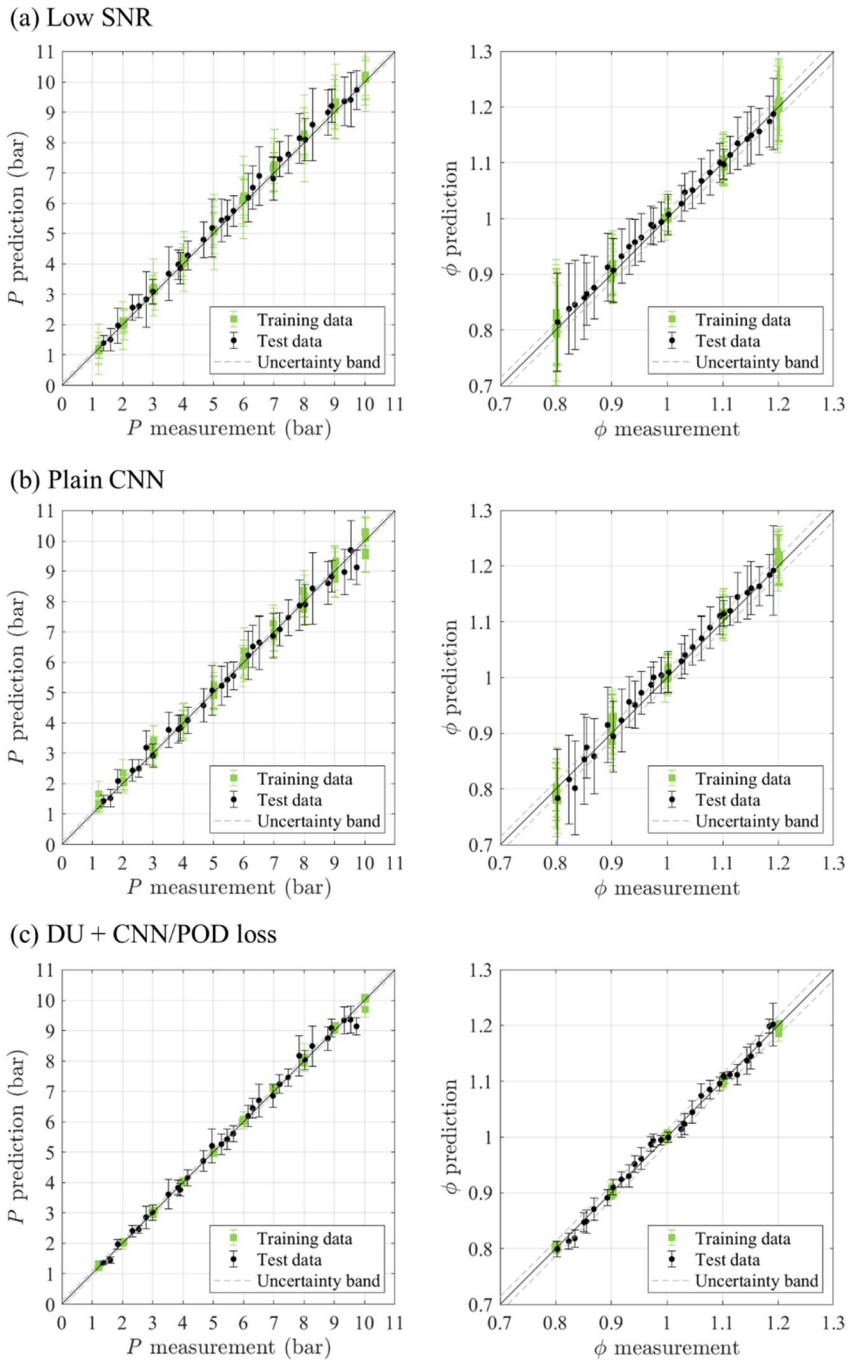

Figure 5.3 Prediction of P and ϕ using (a) Low SNR signal (without denoising), (b) Plain CNN, and (c) DU + CNN /POD loss (Proposed method)

Table 5.1 Comparison of quantitative performance parameters

Error	LS			Plain CNN			DU + CNN / POD loss		
Unit: %	REC	REP	RSD	REC	REP	RSD	REC	REP	RSD
P	14	12	14	10	9.9	12	2.2	5.7	6.4
ϕ	4.8	4.1	5.0	3.6	4.2	5.0	0.56	1.5	1.6

*LS: low-SNR, REC: average relative error of training data in calibration, REP: average relative error of test data in prediction, RSD: average relative standard deviation of test data in prediction.

5.2.2 Neural network architecture and loss function

As discussed in sections 4.3.2 and 4.3.3, hyperparameters of a neural network architecture and a loss function determine denoising capacity, efficiency, and performance. Denoised and reconstructed spectral features by the trained neural network model outputs are used to predict gas properties. Consequently, prediction accuracy and precision of gas properties using the model are determined by the neural network architecture and loss function. Figure 5.4 shows the prediction accuracy of P and ϕ depending on the selection of hyperparameters and loss function configurations; the REP, prediction error of P and ϕ, represents the performance of the CNN architecture to predict the gas properties of interest. The prediction accuracy improves as the marker approaches the origin of the graph in Figure 5.4, which means zero prediction error. The blue markers represent the prediction accuracy of the novel proposed loss function that combines MSE and POD losses, whereas the green markers indicate the prediction accuracy of the conventional loss function, MSE losses. The shape of the marker indicates six different combinations of N_k (3, 15, and 25) and N_d (1 and 16), and the brightness of the markers

indicates N_l, which increases from 2 to 15 as it gets darker. Generally, prediction errors decrease as N_l increases due to model capacity. In addition, it is evident that the DU operator (N_d = 16) and the new loss function (MSE + POD) significantly reduce REP. On the other hand, the prediction errors of some cases using the plain CNN with MSE loss are even greater than those of the calibration process using raw LS spectra without denoising. In this case, the denoising CNN can misinterpret the properties contained in the raw spectrum data when misguided by the MSE loss function.

Recall that POD decomposes spectra into dominant bases spanning the entire spectrum space, and the POD coefficients (the weight of basis) correlate with gas properties. Therefore, the denoising architecture regulated by adding POD losses can preserve and reconstruct property-sensitive spectral features in the spectrum to improve REP of gas properties, whereas the conventional loss function simply considers the mean square errors (MSE) of the spectra regardless of the sensitivity of the spectrum profile to the properties of interest.

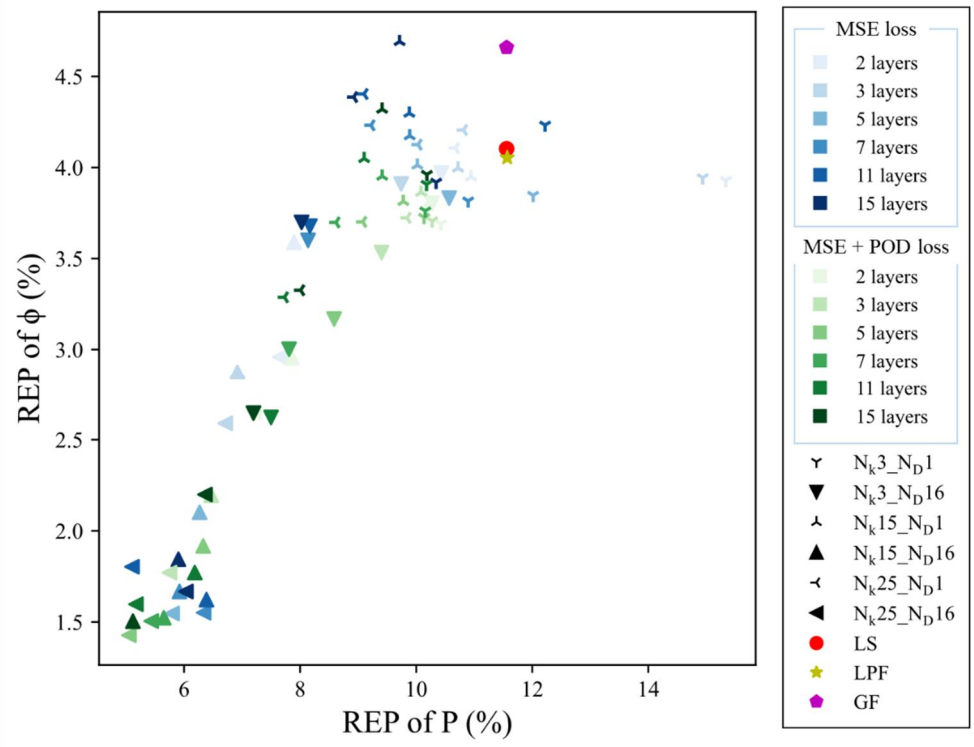

Figure 5.4 REP of P and ϕ with different combinations of two loss functions, six pairs of N_k (3, 15, and 25) and N_d (1 and 16), and six N_l (2, 3, 5, 7, 11, and 15).

Moreover, as discussed in section 4.3.2, it is observed that the receptive field of neural networks determines its denoising performance; therefore, the receptive field would be critical to prediction accuracy. Figure 5.5 describes the trends of REP and RSD with respect to the receptive field. The hyperparameters N_l (2 – 15), N_k (3 – 45), and N_d (1 – 32) vary to represent the effect of the receptive field on model performance. N_d is 1 for 'plain CNN' and varies from 2 to 32 for 'DU + CNN'. Both neural network architectures are regularized by MSE + POD loss for a fair comparison of their receptive fields. The trends of REP and RSD are similar to those of the denoising performance parameter (REA) in Figure 4.6; the REP and RSD are nearly constant for the receptive fields below 100, but rapidly decline until the receptive field reaches the number of components of the input spectrum (W, 1696 × 1), and both the performance indicators (REP and RSD) approach their minimums at around 2 × W. As mentioned in section 4.3.2, each output pixel is constructed using all the input pixels when the receptive field is 2 × W (consider the endpoints on each side). Therefore, further increasing the receptive field beyond 2 × W does not significantly affect model performance. In conclusion, the receptive field of CNN should be set between W and 2 × W to minimize REP and RSD, and near W to reduce model complexity with acceptable prediction accuracy and precision.

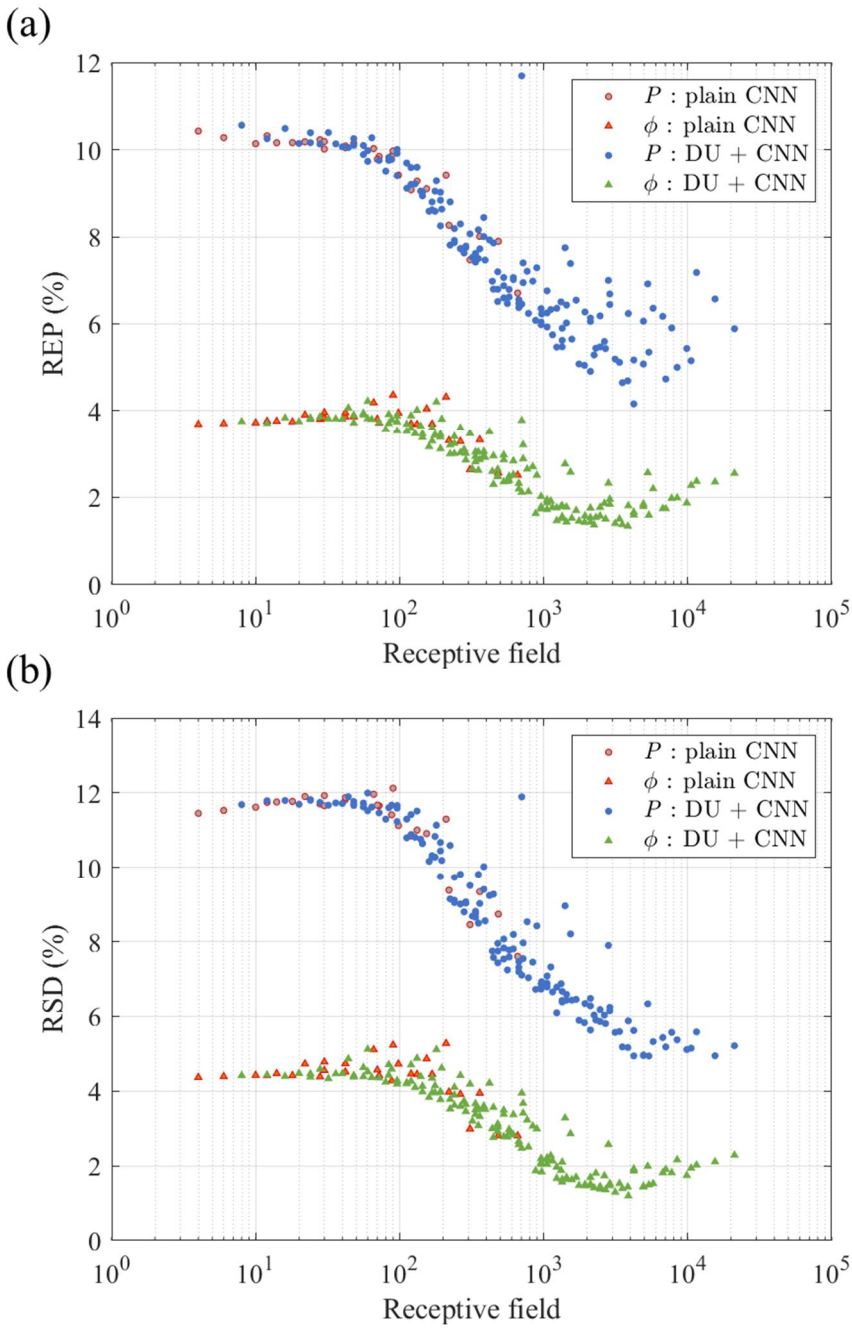

Figure 5.5 (a) REP and (b) RSD of P and ϕ versus the receptive fields of plain CNN (N_d = 1) and DU + CNN (N_d = 2 – 32) trained by MSE loss

5.2.3 Hyperparameter search

Neural network architecture and regularization method are controlled by the hyperparameters chosen by the experimenter. To obtain the best neural network model, the experimenter needs to tune the hyperparameters. The hyperparameters of the proposed neural network architecture are the depth of the layer (N_l), the number of channels (N_c), the kernel (filter) size (N_k), and the down-sampling parameter (N_d). Also, the hyperparameter for the loss function is the blending parameter (α). A baseline model of plain CNN without POD loss (N_l = 7, N_c = 32, N_k = 15, N_d = 1, and α = 0) and a baseline model of DU+CNN with POD loss (N_l = 7, N_c = 32, N_k = 15, N_d = 16, and α = 0.1) are chosen to show the impact of the proposed CNN architecture and loss function. These are examples of parameter sets from the parametric study. The effect of N_l, N_k, and N_d were analyzed in Figure 5.4 and the critical parameters influencing the performance of the model were revealed, i.e., the receptive field calculated in Eq. 4.1 and discussed in Figure 4.6 and Figure 5.5. Furthermore, N_c is fixed as 32 because the effect of the variation of N_c is negligible if N_c is a sufficiently large number (greater than 16 in our dataset), as shown in Figure 5.6. α is set to 0.1 to account for the magnitude of each loss term to be matched because the loss function consists of the summation of the two terms: MSE loss and POD loss.

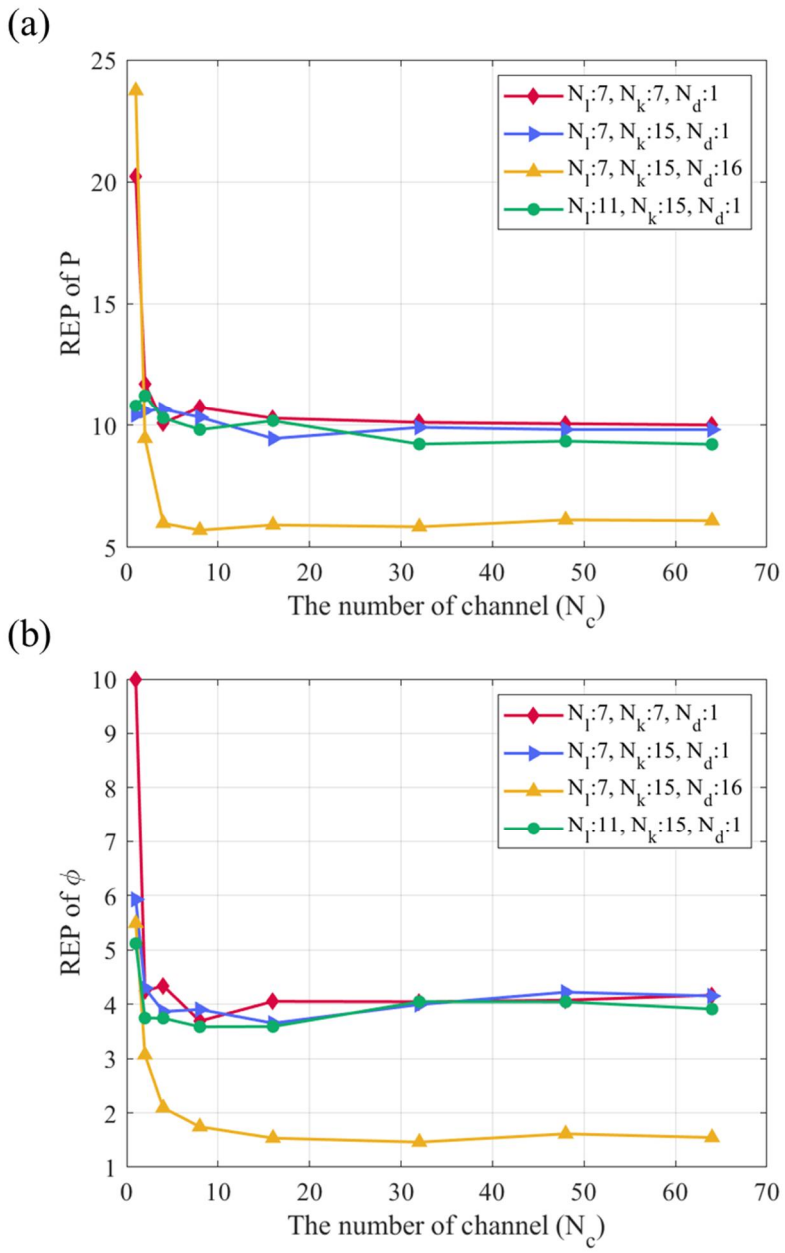

Figure 5.6 Performance variation according to the number of channels of neural networks.

In general, the best hyperparameter of a neural network model can be determined by the process called hyperparameter search (which is also known as hyperparameter optimization or hyperparameter tuning) and the best hyperparameter set can be validated using a dataset that is not used in the training process [93]. Figure 5.7 presents the results of the hyperparameter search for neural network models. Here, the average relative error of validation data (REV) is introduced. The REV is calculated by the same equation as REC but uses the validation data that is included in training data but not used in the training process. The REVs of P and ϕ are used as objective functions in this optimization process. This is because the test data is not available during the calibration process. The objective function (REV) should be minimized and it reaches its optimum point as the marker approaches the origin of the graph in Figure 5.7. Therefore, the result of the hyperparameter search provides a Pareto front that indicates potential sets of optimized hyperparameters. Three sets of optimized hyperparameters in the Pareto front are selected and investigated: OPT1 (N_l = 3, N_k = 45, and N_d = 16), OPT2 (N_l = 5, N_k = 45, and N_d = 16), and OPT3 (N_l = 15, N_k = 45, and N_d = 16). The gas property prediction results of OPT1, OPT2, and OPT2 with POD/Kriging are shown in Figure 5.8 and Table 5.2. REPs of both gas properties using OPT1 and OPT2 are improved compared to DU+CNN/POD loss architecture. However, OPT3 degraded prediction performance (REP) despite improved REV and REC of both gas properties. This is because the denoising process using OPT3 overfits the training data with a receptive field of 10560, which is too large for the component size of the spectral data.

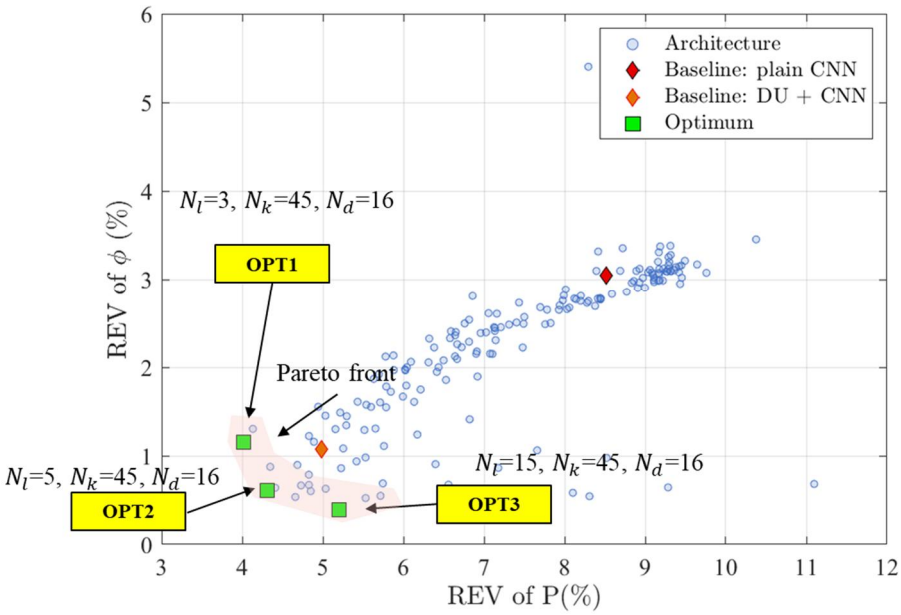

Figure 5.7 Hyperparameter search using REV as optimization function

Table 5.2 Comparison of quantitative performance parameters for OPT1, OPT2, and OPT3 with POD/Kriging

Error Unit: %	OPT1			OPT2			OPT3		
	REC	REP	RSD	REC	REP	RSD	REC	REP	RSD
P	2.9	4.9	5.6	1.9	4.7	5.2	2.1	5.2	5.1
ϕ	0.83	1.4	1.7	0.35	1.4	1.4	0.29	2.3	1.9

*LS: low-SNR, REC: average relative error of calibration data, REP: average relative error of test data in prediction, RSD: average relative standard deviation of test data in prediction.

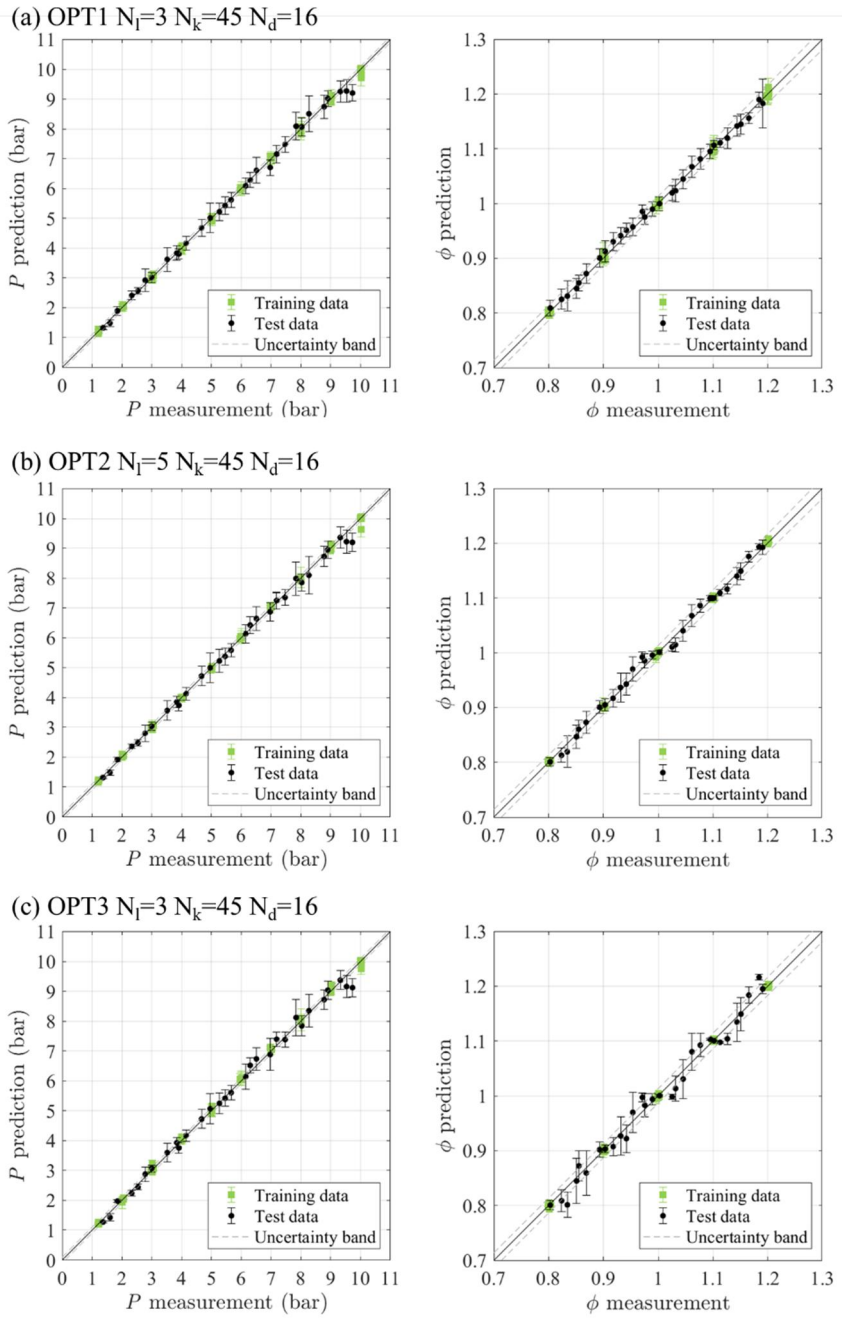

Figure 5.8 Prediction of P and ϕ using signals processed by (a) OPT1, (b) OPT2, and (c) OPT3

5.2.4 Noise level sensitivity analysis

In practical applications, the noise level of spectral signals can suffer from drift depending on the detection system. For example, variation in sensor temperature causes the fluctuation of dark current noise. Therefore, with varying different input noise levels, the performance of a neural network denoiser trained on a spectral dataset is evaluated in this section.

Different levels of noise are imposed by data augmentation that changes the intensity of the signals of inputs during training neural networks. Therefore, trained neural networks should be able to handle different noise levels. Moreover, As shown in Figure 5.9, the noise level of our dataset inherently varies with the flame conditions in the target system since the fuel volume flow rate depends on the flame speed to operate the flat flame burner. The SNR of each spectrum is estimated using the peak signal-to-noise ratio (PSNR) defined below:

$$PSNR = 10 \log_{10} \frac{MAX_I^2}{MSE} \tag{5.1}$$

Where MAX_I is the maximum possible value and MSE is the mean squared error. The ground truth signals for PSNR analysis are the 10-shot averaged high SNR dataset. The denoising neural networks are trained using the dataset with the variable noise level of PSNR from 13 to 29.

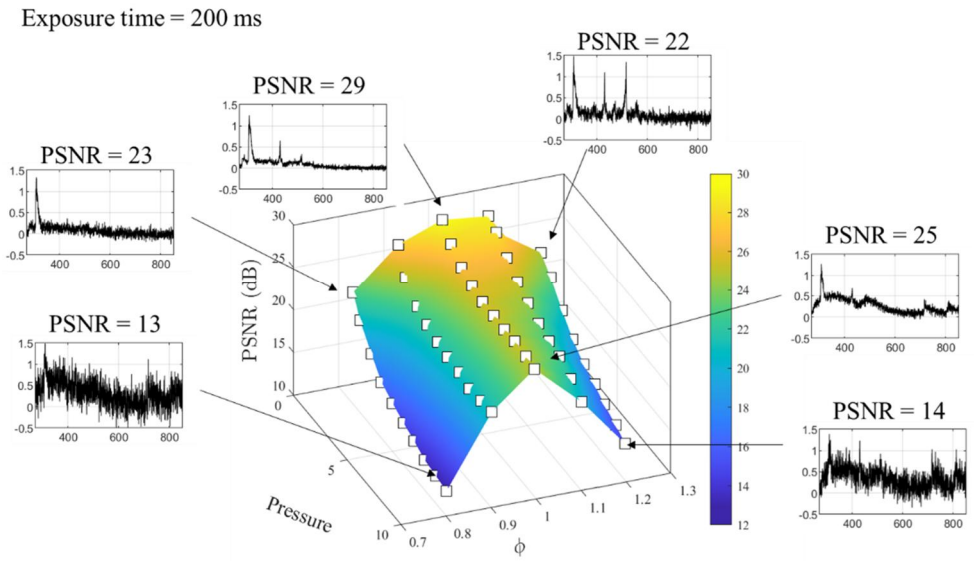

Figure 5.9 PSNR variations of flame emission with 0.2 s exposure time

To check the noise sensitivity of the trained neural network, the noise is approximated as white Gaussian noise. In white Gaussian noise, the level of noise can be controlled by adjusting the variation parameter. The examples of signals with various noise and noise sensitivity curves using signals with 5 flame conditions are shown in Figure 5.10. For the five flame conditions, the PSNR of signals remains almost constant until the noise level reaches 0.02 and then decreases.

The prediction results using the denoised signal with various noise levels are shown in Figure 5.11. The prediction results are quantified using REP and RSD of P and ϕ. The prediction results of P and ϕ show rapid degradation of accuracy and precision over noise levels 0.02 and 0.1, respectively.

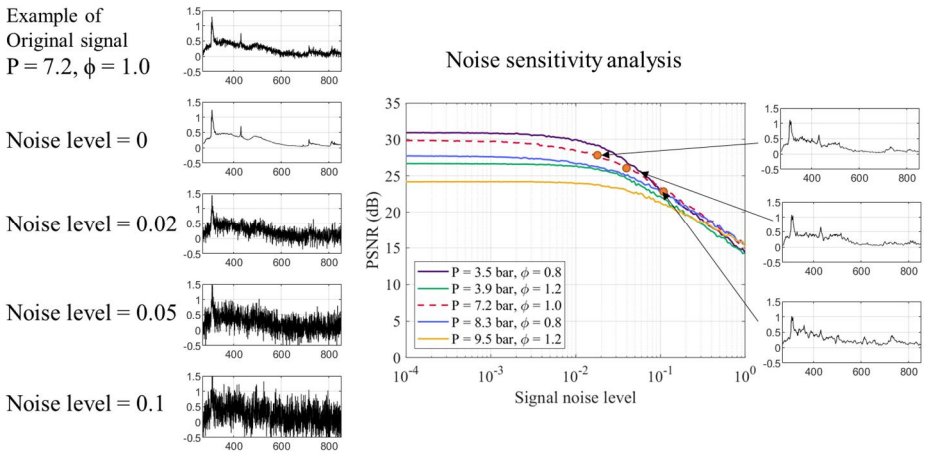

Figure 5.10 Typical signals with different noise levels and PSNR variations of denoised flame emissions

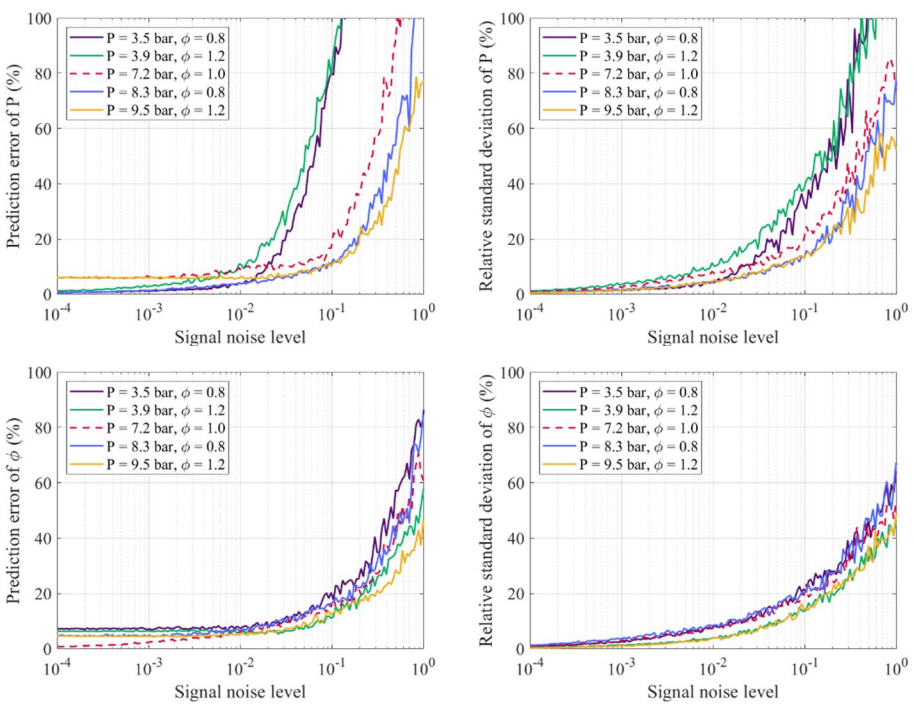

Figure 5.11 Accuracy and precision performance using inputs with different noise levels.

5.2.5 Exposure time

In order to monitor gas properties in rapidly evolving combustion, it is important to match the sampling rate and exposure time to the characteristic time scale. For example, the characteristic time for swirl flames with a processing vortex core is several milliseconds (ms) [23, 94]. Moreover, the time scales of turbulent flame dynamics are the integral time scale and Kolmogorov time scale, which are hundreds and tens of microseconds (μs), respectively [24, 95]. According to section 2.1.3, a monotonic decrease in SNR is estimated with reduced exposure time. The experimental results support the analysis, as presented in Figure 2.3. Therefore, as the exposure time decreases, the accuracy of gas prediction decreases. In this section, the effect of reduced exposure time on the performance of the calibration models is evaluated by repeating the experiments with varying exposure times (0.05, 0.2, and 0.4 s). As shown in Figure 5.12 (a) and (b), REP was compared between BI3/MLR (section 3.4.1), PLS-R (section 3.4.1), and POD/Kriging with and without deep learning-based denoising. The prediction error of P and ϕ using every calibration method increases by reducing the exposure time. Furthermore, the REP of the POD/Kriging method with denoising outperformed REP of the method without denoising although OPT3 architecture showed a higher value of error when the exposure time is 400 ms, which is resulting from overfitting to the calibration dataset (see Figure 5.8 (c)).

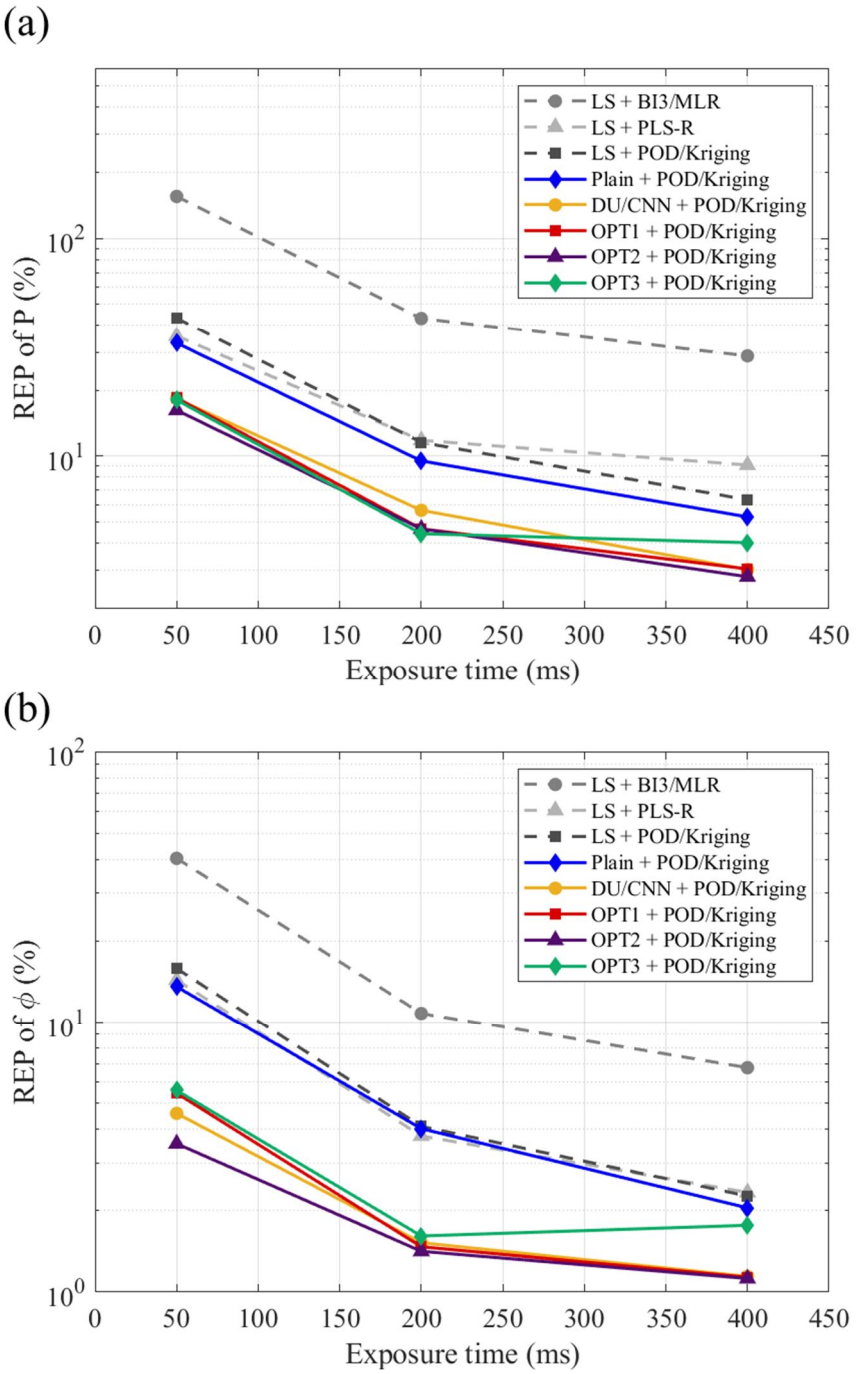

Figure 5.12 REP of (a) P and (b) ϕ versus exposure time.

CHAPTER 6. CONCLUSIONS

This dissertation proposes a framework of FES combining the data-driven calibration process and deep learning-based denoising method to achieve fast time-resolved and high-accuracy combustion diagnostics. The data-driven calibration process consists of mapping the emission spectra from a high-dimensional non-linear dimension to gas properties (P and ϕ) by using the emission dataset from high-pressure methane-air combustion. As a result of this calibration model, gas properties can be evaluated without any additional information from electrical sensors or chemical reaction simulations. Moreover, pre-processing of the raw spectral data using deep learning-based denoising methods can suppress noise and restore information to achieve accurate measurement from fast time-resolved low SNR spectral data. With these strategies, it would be possible to utilize the potential of a fast time-resolved FES, given that modern detection systems have high sampling rates.

A data-driven calibration method based on ROM consists of the POD and Kriging model trained using only high SNR data from the training dataset. The dimension of the data can be significantly reduced by extracting POD basis vectors that span the entire space of the spectrum. Then the variations of the weight of the POD basis

(POD coefficient) are correlated with gas properties using the Kriging model to predict gas properties using unknown spectra in arbitrary flame conditions. Moreover, LOOCV and GSA validate and analyze the ROM trained by the training dataset so that it can be used to predict gas properties. It is confirmed that the POD defines the directions most sensitive to gas properties and extracts gas property indicators over a wide spectral region. Moreover, the gas properties, the outputs of the Kriging model, can be accurately predicted using a POD coefficient vector, which is a projection of an unknown flame emission spectrum (test data) onto the POD bases. The prediction accuracy of the gas properties is significantly improved within a few percent.

The deep learning-based denoising method utilizes an architecture consisting of a DU operator and deep plain CNN layers. The architecture is trained by pairs of low and high SNR spectra, i.e. captured at short and long exposure times, respectively. This training is regularized by a loss function in which the MSE loss and POD loss are combined. The POD loss is the L2 norm for POD coefficient difference, which indicates the error of property-sensitive components in the emission spectrum. The proposed neural network architecture successfully suppresses noise in the LS spectral signals while maintaining the characteristic spectral characteristics of the spectra. Moreover, the selection of hyperparameters for neural network architecture is investigated. It is revealed that the size of the receptive field calculated by the combination of N_l, N_k, and N_d is critical to improving the performance of the

neural network model.

Then, the trained ROM and deep learning-based denoising method are combined so that the gas properties are predicted from the short-gated low SNR spectrum from an unknown flame condition. With the proposed framework of FES, the prediction errors of the P and ϕ improved to approximately 5.7% and 1.5% at 0.2 s exposure time (11% and 4% using the POD and Kriging model without denoising), and to 18% and 5% at 0.05 s exposure time (from 43% and 16% without denoising), respectively.

It is clear that the proposed calibration method can further improve the temporal resolution and accuracy to fully exploit the potential of FES. Also, the method is straightforward to apply to data from other detection systems. Therefore, when using a more sensitive and faster detection system, such as a high-speed kHz frame camera with a signal intensifier with devices currently available on the market, accurate monitoring of gas properties at sampling rates of several hundred kHz is possible. Furthermore, the proposed calibration method is applicable to turbulent flames, given that previous FES studies on turbulent flames also utilized a calibration process that collected flame emissions from the entire flame region.

Moreover, the proposed combined framework of denoising and ROM technique can also be used for other types of multi-dimensional data such as 2D/3D images due to the nature of the data-driven technique. Therefore, this new calibration method can significantly improve the measurement accuracy of various other optical

methods including laser absorption spectroscopy (LAS), laser-induced breakdown spectroscopy (LIBS), Raleigh and Raman scattering spectroscopy, and electron spectroscopy. In future works, the application of the proposed method to various optical measurement methods will be investigated.

APPENDIX A

A.1 Result of computational simulation

Table A.1 presents the simulation results to operate a high-pressure combustor.

Table A.1 Simulation result of flame properties

case #	ϕ	P (bar)	χ_{NO} $(\times 10^{-5})$	χ_{NO_2} $(\times 10^{-8})$	χ_{CO} $(\times 10^{-3})$	χ_{CO_2} $(\times 10^{-2})$	T_{ad} (K)	Flame speed (cm/s)
A1	0.8	1.2	2.1	1.7	0.5	7.6	1996	25.1
A2	0.9	1.2	6.0	2.8	2.2	8.3	2135	31.6
A3	1	1.2	9.9	2.1	8.9	8.5	2225	35.7
A4	1.1	1.2	7.6	0.4	26.3	7.4	2204	36.0
A5	1.2	1.2	7.1	0.1	45.4	6.1	2129	31.3
B1	0.8	2	2.4	2.5	0.4	7.6	1996	20.0
B2	0.9	2	7.8	4.7	1.6	8.4	2139	25.5
B3	1	2	13.4	3.4	7.2	8.7	2239	29.0
B4	1.1	2	8.2	0.5	25.6	7.5	2213	29.2
B5	1.2	2	8.0	0.1	45.3	6.2	2134	24.5
C1	0.8	3	2.9	3.7	0.3	7.6	1997	16.4
C2	0.9	3	10.4	7.7	1.4	8.4	2141	21.1
C3	1	3	17.9	5.3	6.4	8.7	2247	24.3
C4	1.1	3	8.9	0.5	25.2	7.6	2217	24.4
C5	1.2	3	8.5	0.1	45.2	6.2	2134	19.4
D1	0.8	4	3.4	5.0	0.3	7.7	1997	14.2
D2	0.9	4	12.9	11.0	1.2	8.4	2142	18.4
D3	1	4	22.4	7.4	5.9	8.8	2251	21.1
D4	1.1	4	9.5	0.5	25.1	7.6	2219	21.1
D5	1.2	4	8.6	0.1	45.1	6.2	2134	16.3

Table A.1 Simulation result of flame properties (Continued)

case #	ϕ	P (bar)	χ_{NO} $(\times 10^{-5})$	χ_{NO_2} $(\times 10^{-8})$	χ_{CO} $(\times 10^{-3})$	χ_{CO_2} $(\times 10^{-2})$	T_{ad} (K)	Flame speed (cm/s)
E1	0.8	5	3.9	6.5	0.2	7.7	1997	12.6
E2	0.9	5	15.8	15.0	1.1	8.4	2144	16.5
E3	1	5	27.1	9.7	5.5	8.8	2254	18.9
E4	1.1	5	10.0	0.6	24.9	7.6	2220	18.7
E5	1.2	5	8.4	0.1	45.0	6.2	2136	14.2
F1	0.8	6	4.4	8.1	0.2	7.7	1998	11.5
F2	0.9	6	18.6	19.3	1.0	8.4	2144	15.0
F3	1	6	31.8	12.3	5.2	8.9	2256	17.3
F4	1.1	6	10.3	0.6	24.9	7.6	2220	17.0
F5	1.2	6	8.0	0.1	45.1	6.2	2135	12.7
G1	0.8	7	5.1	9.9	0.2	7.7	1998	10.5
G2	0.9	7	21.3	24.0	0.9	8.4	2145	13.9
G3	1	7	36.3	14.8	5.0	8.9	2258	16.0
G4	1.1	7	10.6	0.6	24.8	7.6	2221	15.7
G5	1.2	7	7.5	0.1	45.0	6.2	2136	11.6
H1	0.8	8	5.6	11.9	0.2	7.7	1999	9.8
H2	0.9	8	24.2	29.0	0.9	8.4	2145	13.0
H3	1	8	40.7	17.4	4.8	8.9	2260	14.9
H4	1.1	8	10.8	0.6	24.7	7.6	2221	14.6
H5	1.2	8	6.9	0.1	45.0	6.2	2136	10.8
I1	0.8	9	6.2	13.8	0.2	7.7	1998	9.2
I2	0.9	9	27.0	34.3	0.8	8.5	2146	12.2
I3	1	9	45.1	20.1	4.6	8.9	2261	14.0
I4	1.1	9	10.9	0.6	24.7	7.6	2222	13.8
I5	1.2	9	6.4	0.1	45.0	6.2	2136	10.2
J1	0.8	10	6.7	15.9	0.2	7.7	1998	8.7
J2	0.9	10	29.9	40.0	0.8	8.5	2146	11.6
J3	1	10	49.4	22.9	4.5	8.9	2262	13.3
J4	1.1	10	11.0	0.6	24.7	7.6	2222	13.0
J5	1.2	10	5.9	0.1	45.0	6.2	2137	9.7

Table A.1 Simulation result of flame properties (Concluded)

case #	ϕ	P (bar)	χ_{NO} ($\times 10^{-5}$)	χ_{NO_2} ($\times 10^{-8}$)	χ_{CO} ($\times 10^{-3}$)	χ_{CO_2} ($\times 10^{-2}$)	T_{ad} (K)	Flame speed (cm/s)
K1	1.1	1.36	7.8	0.4	26.1	7.5	2208	34.4
K2	1.18	1.59	7.4	0.2	41.7	6.4	2149	28.9
K3	0.85	1.84	4.3	3.4	0.8	8.0	2070	23.8
K4	0.97	2.33	14.4	5.4	4.3	8.7	2220	26.5
K5	1.11	2.53	8.3	0.4	27.4	7.4	2209	26.2
K6	0.8	2.76	2.7	3.4	0.3	7.6	1997	17.1
K7	0.99	3	18.1	6.1	5.4	8.7	2240	24.1
K8	0.82	3.5	4.2	5.3	0.4	7.8	2028	16.1
K9	1	3.83	21.6	7.0	6.0	8.8	2250	21.6
K10	1.16	3.93	8.6	0.2	37.6	6.7	2168	18.9
K11	1.02	4.15	20.3	4.8	8.4	8.7	2259	21.0
K12	0.95	4.65	23.2	14.6	2.4	8.7	2206	18.5
K13	0.85	4.99	8.2	10.6	0.5	8.0	2073	14.7
K14	0.93	5.25	22.3	17.5	1.7	8.6	2183	16.9
K15	1.09	5.43	10.8	0.7	22.7	7.8	2228	18.1
K16	1.05	5.68	16.9	2.4	13.6	8.4	2257	18.1
K17	1.15	6.14	8.8	0.3	35.4	6.9	2178	15.1
K18	1.13	6.28	9.2	0.3	31.2	7.1	2196	15.8
K19	0.89	6.49	17.7	20.4	0.8	8.4	2131	14.1
K20	1.14	6.98	9.0	0.3	33.3	7.0	2187	14.5
K21	0.97	7.17	38.3	24.0	2.8	8.9	2232	15.3
K22	1.08	7.47	12.7	1.0	20.2	7.9	2238	15.5
K23	0.87	7.84	16.1	23.1	0.5	8.2	2103	12.2
K24	1.06	8.03	16.8	2.0	15.6	8.3	2253	15.1
K25	0.83	8.28	9.4	17.2	0.3	7.9	2044	10.6
K26	0.92	8.76	32.9	35.8	1.1	8.6	2173	12.9
K27	1.04	8.89	24.7	4.5	11.2	8.6	2265	14.4
K28	0.9	9.33	28.0	36.2	0.8	8.5	2146	12.0
K29	1.19	9.54	6.6	0.1	43.2	6.3	2145	10.3
K30	0.94	9.72	43.5	42.3	1.5	8.7	2199	12.6

A.2 Denoising performance of neural networks with MSE loss

Table A.2 presents the REA of each local characteristic feature with different neural network architectures trained by MSE loss.

Table A.2 REA of neural networks trained with MSE loss

N_l	N_k	N_c	N_d	RF	REA (%)				
					OH*	CH*	C_2*	H_2O*	BB
2	3	32	1	5	1.99	10.33	36.33	87.77	3.29
2	3	32	16	80	2.10	10.23	45.30	34.52	3.25
2	7	32	1	13	2.12	11.60	39.38	49.95	3.15
2	7	32	16	208	2.13	9.23	38.14	29.00	3.23
2	15	32	1	29	2.19	11.34	42.79	38.22	3.22
2	15	32	16	464	1.96	7.57	28.18	22.79	2.89
2	25	32	1	49	2.22	11.25	46.22	35.68	3.31
2	25	32	16	784	1.82	6.65	24.28	22.45	2.52
2	45	32	1	89	2.17	11.26	45.23	32.81	3.26
2	45	32	16	1424	1.72	7.79	28.20	21.84	2.35
3	3	32	1	7	1.96	9.90	37.55	80.10	3.42
3	3	32	16	112	2.08	7.76	30.96	29.34	3.17
3	7	32	1	19	2.20	8.43	35.38	43.77	3.33
3	7	32	16	304	1.95	7.36	26.86	24.91	2.94
3	15	32	1	43	2.24	8.58	39.20	36.49	3.51
3	15	32	16	688	1.61	5.67	24.75	19.94	2.52
3	25	32	1	73	2.09	9.00	37.31	35.53	3.18
3	25	32	16	1168	1.46	6.18	18.31	20.46	2.79
3	45	32	1	133	2.31	7.99	33.70	29.02	3.40
3	45	32	16	2128	1.27	5.26	13.10	18.10	2.68
5	3	32	1	11	1.96	8.54	37.15	57.38	3.17
5	3	32	16	176	2.66	7.28	31.14	32.23	4.45
5	7	32	1	31	2.12	8.29	37.99	40.47	3.33

Table A.2 REA of neural networks trained with MSE loss (Continued)

N_l	N_k	N_c	N_d	RF	REA (%)				
					OH*	CH*	C_2*	H_2O*	BB
5	15	32	1	71	2.18	8.59	36.40	29.20	3.37
5	15	32	16	1136	1.27	4.81	17.10	19.88	2.50
5	25	32	1	121	2.12	9.12	36.73	30.19	3.08
5	25	32	16	1936	1.25	5.00	12.18	13.98	2.80
5	45	32	1	221	2.01	7.95	32.56	26.17	2.97
5	45	32	16	3536	1.22	5.17	11.37	14.60	2.87
7	3	32	1	15	2.02	8.40	36.67	43.40	3.15
7	3	32	16	240	1.96	6.87	28.91	21.18	2.99
7	7	32	1	43	2.06	9.22	36.15	36.06	3.18
7	7	32	16	688	1.48	5.82	20.32	21.68	2.64
7	15	32	1	99	2.10	8.43	34.87	28.51	3.20
7	15	32	16	1584	1.34	4.95	12.42	17.63	3.20
7	25	32	1	169	2.13	9.07	35.59	25.58	3.43
7	25	32	16	2704	1.20	5.24	13.05	17.59	3.12
7	45	32	1	309	2.04	7.95	31.01	22.89	3.04
7	45	32	16	4944	1.43	5.97	11.94	9.81	3.89
11	3	32	1	23	2.04	8.55	36.02	47.21	3.18
11	3	32	16	368	1.80	5.94	25.26	22.35	2.92
11	7	32	1	67	2.15	8.65	36.66	30.43	3.19
11	7	32	16	1072	1.54	5.28	17.52	19.85	3.31
11	15	32	1	155	2.47	9.68	36.58	26.31	4.40
11	15	32	16	2480	1.66	5.53	12.88	16.91	3.95
11	25	32	1	265	2.10	9.09	34.97	26.64	2.99
11	25	32	16	4240	1.01	6.40	16.46	9.39	2.41
11	45	32	1	485	2.04	6.95	29.13	22.89	3.25
11	45	32	16	7760	1.76	7.53	17.07	10.53	4.39
15	3	32	1	31	2.08	8.83	37.47	30.43	3.17
15	3	32	16	496	1.67	6.43	22.70	20.80	2.77
15	7	32	1	91	2.14	9.55	36.99	27.95	3.46
15	7	32	16	1456	1.86	5.33	12.66	18.68	4.26

Table A.2 REA of neural networks trained with MSE loss (Concluded)

N_l	N_k	N_c	N_d	RF	REA (%)				
					OH*	CH*	C_2*	H_2O*	BB
15	15	32	1	211	2.22	9.58	39.57	26.36	3.14
15	15	32	16	3376	1.16	6.36	16.28	13.64	2.69
15	25	32	1	361	2.30	7.82	32.80	24.36	3.43
15	25	32	16	5776	1.35	6.33	14.03	9.79	3.38
15	45	32	1	661	1.91	7.94	22.58	22.47	3.54
15	45	32	16	10576	1.48	7.10	18.32	13.04	3.81

A.3 Denoising performance of neural networks with MSE and POD loss

Table A.3 presents the REA of each local characteristic feature with different neural network architectures trained by combined MSE loss and POD loss.

Table A.3 REA of neural networks trained with MSE+POD loss

N_l	N_k	N_c	N_d	RF	REA (%)				
					OH*	CH*	C_2*	H_2O*	BB
2	3	32	1	5	2.04	7.81	34.74	45.62	3.32
2	3	32	16	80	2.08	7.92	35.93	39.06	3.32
2	7	32	1	13	2.01	8.26	38.05	40.85	3.25
2	7	32	16	208	1.98	7.32	30.29	31.68	3.13
2	15	32	1	29	2.01	8.47	39.36	37.06	3.21
2	15	32	16	464	1.85	6.68	25.45	31.81	2.96
2	25	32	1	49	2.02	8.49	40.66	35.97	3.20
2	25	32	16	784	1.67	5.87	23.12	27.13	2.65
2	45	32	1	89	2.02	8.25	37.80	34.70	3.14
2	45	32	16	1424	1.66	6.47	23.72	30.33	2.79
3	3	32	1	7	2.01	7.63	34.95	41.56	3.23
3	3	32	16	112	1.99	7.20	30.01	32.45	3.12
3	7	32	1	19	2.03	7.78	36.29	35.50	3.20
3	7	32	16	304	1.80	6.66	25.90	28.07	2.92
3	15	32	1	43	2.04	8.16	37.66	36.28	3.16
3	15	32	16	688	1.46	5.69	21.21	23.85	2.46
3	25	32	1	73	2.04	7.73	36.02	34.68	3.14
3	25	32	16	1168	1.28	4.86	15.93	21.60	2.24
3	45	32	1	133	2.01	7.82	32.45	29.99	3.15
3	45	32	16	2128	1.03	4.49	13.81	15.38	2.11
5	3	32	1	11	2.01	7.70	34.85	36.57	3.20
5	3	32	16	176	1.98	6.85	28.84	28.50	3.08
5	7	32	1	31	2.04	8.26	35.37	34.29	3.16

Table A.3 REA of neural networks trained with MSE+POD loss (Continued)

N_l	N_k	N_c	N_d	RF	REA (%)				
					OH*	CH*	C_2*	H_2O*	BB
5	15	32	1	71	2.08	8.04	35.35	32.60	3.19
5	15	32	16	1136	1.37	5.21	17.80	22.69	2.43
5	25	32	1	121	1.99	8.08	32.51	29.99	3.09
5	25	32	16	1936	1.12	4.84	13.55	16.10	2.53
5	45	32	1	221	1.93	7.79	29.82	27.49	2.98
5	45	32	16	3536	1.07	4.84	12.90	11.00	2.32
7	3	32	1	15	2.03	8.11	35.33	35.84	3.19
7	3	32	16	240	1.83	6.71	26.91	27.25	2.91
7	7	32	1	43	2.06	8.42	37.29	33.14	3.15
7	7	32	16	688	1.40	5.29	19.52	20.68	2.47
7	15	32	1	99	2.04	8.55	34.59	31.58	3.14
7	15	32	16	1584	1.18	5.25	16.30	18.34	2.78
7	25	32	1	169	1.99	8.31	32.82	27.64	3.08
7	25	32	16	2704	1.08	5.20	12.94	14.41	2.54
7	45	32	1	309	1.73	6.58	24.88	25.89	2.82
7	45	32	16	4944	1.25	6.16	14.28	8.67	2.83
11	3	32	1	23	2.06	8.57	36.02	33.21	3.17
11	3	32	16	368	1.73	6.10	23.54	24.22	2.74
11	7	32	1	67	2.11	9.10	38.31	33.20	3.15
11	7	32	16	1072	1.38	5.04	17.71	19.68	2.83
11	15	32	1	155	2.02	8.57	32.74	28.56	3.10
11	15	32	16	2480	1.29	6.39	15.38	13.63	3.28
11	25	32	1	265	1.89	7.45	28.41	24.91	2.92
11	25	32	16	4240	1.10	5.24	17.09	15.32	2.09
11	45	32	1	485	1.73	6.04	23.12	27.72	2.86
11	45	32	16	7760	1.37	6.50	15.70	9.10	3.28
15	3	32	1	31	2.07	8.68	37.18	33.43	3.16
15	3	32	16	496	1.62	6.08	22.81	22.77	2.78
15	7	32	1	91	2.12	9.49	39.49	31.84	3.17
15	7	32	16	1456	1.40	5.44	13.99	19.37	3.23

Table A.3 REA of neural networks trained with MSE+POD loss (Concluded)

N_l	N_k	N_c	N_d	RF	REA (%)				
					OH*	CH*	C_2*	H_2O*	BB
15	15	32	1	211	2.14	8.97	35.97	28.14	3.17
15	15	32	16	3376	1.07	5.37	14.05	24.59	2.37
15	25	32	1	361	1.89	7.36	26.44	25.54	2.93
15	25	32	16	5776	1.56	7.49	17.39	13.27	3.90
15	45	32	1	661	1.63	6.04	20.38	22.88	2.68
15	45	32	16	10576	1.22	7.28	18.51	8.51	2.80

A.4 Calibration and prediction performance of neural network architecture trained by MSE and POD loss

Table A.4 presents the REC, REP, and RSD of P and ϕ with different neural network architectures trained by combined MSE loss and POD loss.

Table A.4 REC, REP, and RSD of neural networks trained with MSE+POD loss

N_l	N_k	N_c	N_d	RF	P			ϕ		
					REC	REP	RSD	REC	RSD	REP
2	3	32	1	4	12.26	10.42	11.45	4.30	3.69	4.37
2	3	32	2	8	12.41	10.56	11.69	4.32	3.75	4.42
2	3	32	4	16	12.11	10.48	11.80	4.36	3.84	4.39
2	3	32	8	32	11.88	10.39	11.67	4.34	3.82	4.33
2	3	32	16	64	11.60	10.27	11.62	4.17	3.80	4.36
2	3	32	32	128	10.40	9.21	10.81	3.59	3.47	4.10
2	7	32	1	12	11.87	10.32	11.75	4.31	3.76	4.41
2	7	32	2	24	11.97	10.39	11.82	4.36	3.84	4.38
2	7	32	4	48	11.84	10.25	11.66	4.37	3.90	4.38
2	7	32	8	96	11.29	10.00	11.66	4.10	3.74	4.27
2	7	32	16	192	10.04	9.02	10.67	3.45	3.39	3.98
2	7	32	32	384	8.39	8.00	9.40	2.60	2.96	3.51
2	15	32	1	28	11.69	10.23	11.71	4.30	3.81	4.38
2	15	32	2	56	11.57	10.09	11.63	4.42	3.95	4.38
2	15	32	4	112	11.12	9.69	11.30	4.09	3.69	4.20
2	15	32	8	224	9.55	8.80	10.59	3.39	3.21	3.78
2	15	32	16	448	7.97	7.86	9.27	2.60	2.96	3.56
2	15	32	32	896	5.70	7.29	8.42	1.83	2.51	2.99
2	25	32	1	48	11.61	10.14	11.69	4.36	3.87	4.41
2	25	32	2	96	11.25	9.91	11.59	4.31	3.88	4.28
2	25	32	4	192	10.09	8.84	10.45	3.69	3.46	3.97
2	25	32	8	384	8.79	8.44	10.02	2.86	3.05	3.60

Table A.4 REC, REP, and RSD of neural networks trained with MSE+POD loss (Continued)

N_l	N_k	N_c	N_d	RF	P			ϕ		
					REC	REP	RSD	REC	RSD	REP
2	25	32	16	768	6.60	7.21	8.53	2.03	2.65	3.23
2	25	32	32	1536	7.82	7.39	8.20	2.51	2.58	2.86
2	45	32	1	88	11.26	9.86	11.41	4.27	3.80	4.28
2	45	32	2	176	10.15	9.05	10.83	3.79	3.45	3.95
2	45	32	4	352	8.74	8.16	9.81	3.05	3.04	3.53
2	45	32	8	704	13.19	11.69	11.89	4.28	3.78	3.95
2	45	32	16	1408	8.19	7.75	8.96	2.50	2.77	3.28
2	45	32	32	2816	5.15	7.00	7.90	1.75	2.33	2.57
3	3	32	1	6	11.85	10.27	11.53	4.27	3.71	4.39
3	3	32	2	12	11.59	10.25	11.79	4.11	3.71	4.43
3	3	32	4	24	11.32	10.16	11.80	4.03	3.81	4.46
3	3	32	8	48	11.18	10.10	11.77	3.88	3.72	4.42
3	3	32	16	96	10.24	9.40	11.23	3.56	3.53	4.19
3	3	32	32	192	8.49	8.25	9.75	2.88	3.12	3.77
3	7	32	1	18	11.38	10.16	11.77	4.01	3.75	4.42
3	7	32	2	36	11.19	10.13	11.73	3.86	3.82	4.46
3	7	32	4	72	10.58	9.75	11.47	3.65	3.74	4.35
3	7	32	8	144	9.43	8.94	10.65	3.12	3.38	3.98
3	7	32	16	288	8.11	7.75	9.03	2.45	2.86	3.45
3	7	32	32	576	6.09	6.79	7.77	1.86	2.49	2.98
3	15	32	1	42	11.04	10.08	11.82	3.63	3.86	4.51
3	15	32	2	84	10.34	9.82	11.60	3.11	3.71	4.43
3	15	32	4	168	8.82	8.61	10.28	2.73	3.30	3.96
3	15	32	8	336	7.55	7.58	8.75	2.25	2.94	3.50
3	15	32	16	672	5.66	6.47	7.46	1.56	2.19	2.66
3	15	32	32	1344	3.60	5.47	6.42	1.07	1.81	2.10
3	25	32	1	72	10.36	9.84	11.66	3.12	3.72	4.42
3	25	32	2	144	9.01	9.03	10.64	2.69	3.46	4.13
3	25	32	4	288	7.53	7.78	9.06	2.16	3.01	3.64

Table A.4 REC, REP, and RSD of neural networks trained with MSE+POD loss (Continued)

N_l	N_k	N_c	N_d	RF	P			ϕ		
					REC	REP	RSD	REC	RSD	REP
3	25	32	8	576	6.01	6.62	7.59	1.79	2.39	2.89
3	25	32	16	1152	4.21	5.75	6.65	1.18	1.77	2.13
3	25	32	32	2304	2.52	5.44	5.90	0.74	1.54	1.80
3	45	32	1	132	8.88	9.28	11.01	2.35	3.69	4.45
3	45	32	2	264	7.61	7.72	9.00	2.22	3.03	3.59
3	45	32	4	528	6.27	6.60	7.53	1.90	2.36	2.78
3	45	32	8	1056	4.40	5.93	6.79	1.22	1.72	2.04
3	45	32	16	2112	2.90	4.91	5.64	0.83	1.43	1.69
3	45	32	32	4224	2.13	4.16	4.94	0.64	1.66	1.92
5	3	32	1	10	11.34	10.14	11.62	4.07	3.73	4.42
5	3	32	2	20	11.31	10.14	11.70	3.83	3.75	4.47
5	3	32	4	40	10.79	10.06	11.72	3.60	3.81	4.47
5	3	32	8	80	9.91	9.50	11.30	3.26	3.56	4.24
5	3	32	16	160	8.74	8.59	10.17	2.63	3.17	3.83
5	3	32	32	320	7.42	7.53	8.68	2.01	2.65	3.20
5	7	32	1	30	10.81	10.01	11.66	3.52	3.84	4.55
5	7	32	2	60	10.08	9.73	11.52	3.13	3.82	4.52
5	7	32	4	120	9.21	9.20	10.89	2.68	3.59	4.26
5	7	32	8	240	7.63	7.91	9.11	2.06	3.01	3.62
5	7	32	16	480	5.99	6.79	7.75	1.57	2.50	3.05
5	7	32	32	960	4.09	5.98	6.87	1.04	1.78	2.09
5	15	32	1	70	10.00	9.78	11.67	2.82	3.81	4.57
5	15	32	2	140	8.35	9.05	10.76	2.07	3.65	4.39
5	15	32	4	280	7.02	7.63	8.80	1.75	3.10	3.73
5	15	32	8	560	5.73	6.47	7.24	1.43	2.37	2.77
5	15	32	16	1120	5.32	6.33	7.32	1.79	1.92	2.27
5	15	32	32	2240	2.11	5.29	6.03	0.45	1.37	1.41
5	25	32	1	120	8.83	9.08	10.85	2.11	3.70	4.46
5	25	32	2	240	7.25	7.87	9.04	1.66	3.24	3.89

Table A.4 REC, REP, and RSD of neural networks trained with MSE+POD loss (Continued)

N_l	N_k	N_c	N_d	RF	P			ϕ		
					REC	REP	RSD	REC	RSD	REP
5	25	32	4	480	5.71	6.51	7.43	1.35	2.48	2.92
5	25	32	8	960	4.18	6.04	6.73	0.99	1.74	2.04
5	25	32	16	1920	2.45	5.05	5.83	0.56	1.43	1.47
5	25	32	32	3840	1.57	4.69	5.17	0.31	1.34	1.43
5	45	32	1	220	7.49	8.26	9.38	1.81	3.31	3.97
5	45	32	2	440	6.06	6.98	7.75	1.47	2.60	3.00
5	45	32	4	880	4.59	6.08	6.72	1.13	1.63	1.87
5	45	32	8	1760	2.69	5.08	5.89	0.62	1.46	1.47
5	45	32	16	3520	1.90	4.65	5.18	0.35	1.38	1.39
5	45	32	32	7040	1.37	4.74	5.18	0.31	1.74	1.91
7	3	32	1	14	11.21	10.16	11.76	3.84	3.76	4.47
7	3	32	2	28	10.90	10.13	11.75	3.49	3.87	4.59
7	3	32	4	56	10.24	9.89	11.73	3.16	3.91	4.63
7	3	32	8	112	9.21	9.11	10.80	2.63	3.53	4.22
7	3	32	16	224	7.54	7.81	9.14	1.99	3.00	3.52
7	3	32	32	448	5.96	6.80	7.57	1.57	2.30	2.76
7	7	32	1	42	10.33	10.04	11.87	2.99	3.96	4.74
7	7	32	2	84	9.53	9.75	11.60	2.43	3.92	4.71
7	7	32	4	168	7.82	8.80	10.32	1.90	3.61	4.35
7	7	32	8	336	6.54	7.42	8.65	1.50	2.82	3.38
7	7	32	16	672	4.58	6.37	7.19	1.13	2.19	2.57
7	7	32	32	1344	2.82	5.62	6.38	0.67	1.52	1.63
7	15	32	1	98	8.94	9.41	11.13	2.16	3.95	4.73
7	15	32	2	196	6.87	8.63	10.19	1.47	3.81	4.62
7	15	32	4	392	5.85	7.46	8.56	1.25	2.92	3.51
7	15	32	8	784	4.14	6.24	7.03	0.90	2.13	2.50
7	15	32	16	1568	2.21	5.65	6.43	0.56	1.52	1.63
7	15	32	32	3136	1.53	5.19	5.57	0.30	1.40	1.30
7	25	32	1	168	7.53	8.62	10.29	1.66	3.70	4.45

Table A.4 REC, REP, and RSD of neural networks trained with MSE+POD loss (Continued)

N_l	N_k	N_c	N_d	RF	P			ϕ		
					REC	REP	RSD	REC	RSD	REP
7	25	32	2	336	5.96	7.62	8.81	1.24	3.05	3.66
7	25	32	4	672	4.61	6.56	7.31	1.20	2.32	2.65
7	25	32	8	1344	2.71	5.90	6.67	0.69	1.56	1.56
7	25	32	16	2688	1.71	5.43	5.81	0.34	1.51	1.36
7	25	32	32	5376	1.34	5.35	4.94	0.26	1.59	1.49
7	45	32	1	308	7.40	7.47	8.45	2.06	2.64	2.99
7	45	32	2	616	8.59	7.06	8.19	2.95	2.52	2.83
7	45	32	4	1232	4.91	5.47	6.09	1.34	1.47	1.66
7	45	32	8	2464	2.22	5.47	5.86	0.40	1.58	1.38
7	45	32	16	4928	1.81	5.08	4.97	0.30	1.79	1.46
7	45	32	32	9856	1.41	5.44	5.11	0.26	1.87	1.74
11	3	32	1	22	10.57	10.18	11.90	3.08	3.91	4.73
11	3	32	2	44	10.21	10.05	11.90	2.74	4.07	4.86
11	3	32	4	88	9.10	9.77	11.67	2.39	3.79	4.59
11	3	32	8	176	7.69	8.58	10.28	1.90	3.43	4.15
11	3	32	16	352	6.15	7.50	8.49	1.45	2.62	3.08
11	3	32	32	704	4.47	6.45	7.10	1.11	2.12	2.47
11	7	32	1	66	8.87	10.02	11.96	1.85	4.19	5.11
11	7	32	2	132	7.35	9.59	11.51	1.51	4.01	4.88
11	7	32	4	264	5.89	8.29	9.82	1.24	3.60	4.42
11	7	32	8	528	4.43	6.88	7.83	1.01	2.86	3.38
11	7	32	16	1056	2.96	6.25	6.89	0.72	1.88	2.17
11	7	32	32	2112	1.69	6.13	6.28	0.35	1.76	1.48
11	15	32	1	154	6.77	9.10	10.91	1.58	4.05	4.86
11	15	32	2	308	5.41	8.07	9.50	1.14	3.47	4.19
11	15	32	4	616	3.82	7.02	7.80	0.92	2.84	3.37
11	15	32	8	1232	2.33	6.36	6.78	0.56	1.76	1.97
11	15	32	16	2464	1.52	6.18	6.18	0.32	1.77	1.44
11	15	32	32	4928	1.45	6.06	4.95	0.30	1.85	1.43

Table A.4 REC, REP, and RSD of neural networks trained with MSE+POD loss (Continued)

N_l	N_k	N_c	N_d	RF	P			ϕ		
					REC	REP	RSD	REC	RSD	REP
11	25	32	1	264	6.07	7.73	9.01	1.46	3.29	3.91
11	25	32	2	528	4.90	7.06	8.07	1.11	2.98	3.49
11	25	32	4	1056	3.19	6.76	7.08	0.74	1.94	2.21
11	25	32	8	2112	2.09	6.06	6.48	0.56	1.54	1.51
11	25	32	16	4224	5.08	5.17	5.62	1.26	1.60	1.86
11	25	32	32	8448	2.94	5.00	5.37	0.74	1.99	2.16
11	45	32	1	484	8.42	7.89	8.74	2.55	2.56	2.81
11	45	32	2	968	6.33	6.23	6.92	1.68	1.75	1.84
11	45	32	4	1936	2.47	6.27	6.34	0.62	1.58	1.50
11	45	32	8	3872	1.67	6.24	5.88	0.31	1.81	1.20
11	45	32	16	7744	1.66	5.91	5.57	0.27	1.98	1.81
11	45	32	32	15488	1.66	6.57	4.95	0.23	2.36	2.11
15	3	32	1	30	10.10	10.18	11.93	2.72	3.96	4.78
15	3	32	2	60	9.36	9.98	12.00	2.24	4.22	5.12
15	3	32	4	120	8.17	9.59	11.42	2.01	3.89	4.70
15	3	32	8	240	6.87	8.19	9.73	1.63	3.40	4.10
15	3	32	16	480	5.07	7.20	7.95	1.31	2.65	3.12
15	3	32	32	960	3.52	6.35	6.77	0.85	2.02	2.20
15	7	32	1	90	7.67	9.97	12.12	1.42	4.36	5.23
15	7	32	2	180	6.59	9.28	11.14	1.29	4.21	5.11
15	7	32	4	360	7.13	7.72	9.02	1.81	2.87	3.32
15	7	32	8	720	3.47	6.95	7.54	0.83	2.89	3.41
15	7	32	16	1440	2.10	6.43	6.58	0.58	1.78	1.69
15	7	32	32	2880	1.57	6.45	6.15	0.33	1.96	1.53
15	15	32	1	210	4.77	9.41	11.30	0.99	4.32	5.28
15	15	32	2	420	4.38	7.93	9.24	0.92	3.51	4.21
15	15	32	4	840	2.92	6.98	7.45	0.75	2.71	3.06
15	15	32	8	1680	2.85	6.55	6.45	0.57	1.70	1.69
15	15	32	16	3360	3.68	5.12	5.59	0.69	1.50	1.53

Table A.4 REC, REP, and RSD of neural networks trained with MSE+POD loss (Concluded)

N_l	N_k	N_c	N_d	RF	P			ϕ		
					REC	REP	RSD	REC	RSD	REP
15	15	32	32	6720	1.85	6.17	5.43	0.38	1.74	1.82
15	25	32	1	360	5.41	8.01	9.34	1.17	3.33	3.94
15	25	32	2	720	3.14	7.40	7.96	0.80	3.21	3.67
15	25	32	4	1440	4.56	6.02	6.43	1.23	1.44	1.64
15	25	32	8	2880	2.04	6.69	6.24	0.39	1.84	1.47
15	25	32	16	5760	1.77	6.36	5.32	0.26	2.20	1.52
15	25	32	32	11520	1.95	7.18	5.58	0.28	2.37	2.02
15	45	32	1	660	5.43	6.71	7.60	1.37	2.51	2.80
15	45	32	2	1320	2.92	6.50	6.87	0.84	1.79	1.88
15	45	32	4	2640	4.53	5.60	6.03	1.39	1.86	1.73
15	45	32	8	5280	1.67	6.92	6.33	0.26	2.57	1.99
15	45	32	16	10560	2.09	5.16	5.15	0.29	2.27	1.94
15	45	32	32	21120	1.90	5.89	5.21	0.23	2.55	2.29
28	15	32	1	392	7.35	8.51	9.60	1.93	3.57	4.18
28	29	32	1	784	7.48	7.98	7.80	2.23	2.51	2.83
28	45	32	1	1232	10.22	8.21	9.62	3.81	3.48	3.45
28	57	32	1	1568	3.04	6.85	6.63	0.83	2.10	2.07
28	115	32	1	3192	5.70	5.42	5.71	1.12	1.55	1.64
56	15	32	1	784	8.53	7.94	8.75	3.31	3.00	3.36
56	29	32	1	1568	10.28	9.00	9.26	2.80	2.95	3.14
56	45	32	1	2464	11.23	8.78	8.16	3.19	2.88	3.24
56	57	32	1	3136	11.04	9.00	6.80	2.27	2.11	2.19
56	115	32	1	6384	23.11	15.86	7.55	11.28	9.24	2.43
14	15	32	1	196	5.80	8.99	10.63	1.31	3.92	4.80
7	29	32	1	196	7.03	8.71	10.12	1.63	3.65	4.32
7	57	32	1	392	7.98	7.51	8.54	2.51	2.53	2.86
7	113	32	1	784	6.58	6.20	6.61	1.98	2.00	1.92
7	225	32	1	1568	6.15	5.60	5.54	1.44	1.53	1.59
7	449	32	1	3136	4.04	4.15	4.42	0.64	1.24	1.13

REFERENCES

[1] International Energy Agency (IEA),"Energy Statistics Data Browser." Paris, 2020, https://www.iea.org/data-and-statistics/data-tools/energy-statistics-data-browser.

[2] Falkner, R. "The Paris Agreement and the new logic of international climate politics." *International Affairs* 92, no. 5 (2016): 1107-1125.

[3] (IEA), I.E.A. "Net Zero by 2050: A Roadmap for the Global Energy Sector." Paris, 2021. https://www.iea.org/reports/net-zero-by-2050.

[4] Samuelsen, S. *Rich burn, quick-mix, lean burn (RQL) combustor.* The Gas Turbine Handbook. 2006.

[5] Feitelberg, A.S. and M.A. Lacey. "The GE rich-quench-lean gas turbine combustor." *Journal of Engineering for Gas Turbines and Power-Transactions of the Asme* 120, no. 3 (1998): 502-508.

[6] Yu, B., et al. "Study on the combustion characteristics of a premixed combustion system with exhaust gas recirculation." *Energy* 61 (2013): 345-353.

[7] Foster, J. and R.S. Miller, *Fundamentals of High Pressure Combustion*, in *High Pressure Processes in Chemical Engineering*, M. Lackner, Editor. 2010, Verlag ProcessEng Engineering GmbH: Weinheim, Germany. pp. 53–75.

[8] Allam, R., et al. "Demonstration ofthe allam cycle: an update on the development status of a high efficiencysupercritical carbon dioxide power process employing full carbon capture." *EnergyProcedia* 114 (2017): 5948-5966.

[9] Iwai, Y., et al. "Development Approach to the Combustor of Gas Turbine for Oxy-fuel, Supercritical CO2 Cycle." Paper presented at the Proceedings of ASME Turbo Expo 2015: Turbine Technical Conference and Exposition, Montreal, Canada, June 15-19 2015.

[10] Anitescu, G., T.J. Bruno, and L.L. Tavlarides. "Dieseline for Supercritical Injection and Combustion in Compression-Ignition Engines: Volatility, Phase Transitions, Spray/Jet Structure, and Thermal Stability." *Energy & Fuels* 26, no. 10 (2012): 6247-6258.

[11] Higgins, B., et al. "Systematic measurements of OH chemiluminescence for fuel-lean, high-pressure, premixed, laminar flames." *Fuel* 80, no. 1 (2001): 67-74.

[12] Kojima, J., Y. Ikeda, and T. Nakajima. "Spatially resolved measurement of OH*, CH*, and C-2* chemiluminescence in the reaction zone of laminar

methane/air premixed flames." *Proceedings of the Combustion Institute* 28 (2000): 1757-1764.

[13] Docquier, N., F. Lacas, and S. Candel. "Closed-loop equivalence ratio control of premixed combustors using spectrally resolved chemiluminescence measurements." *Proceedings of the Combustion Institute* 29 (2002): 139-145.

[14] Oh, S., et al. "Impacts of N2 and CO2 diluent gas composition on flame emission spectroscopy for fuel concentration measurements in flames." *International Journal of Heat and Mass Transfer* 149 (2020).

[15] Qiu, X.B., et al. "Fire Detection Algorithm Combined with Image Processing and Flame Emission Spectroscopy." *Fire Technology* 54, no. 5 (2018): 1249-1263.

[16] Ikeda, Y., J. Kojima, and H. Hashimoto. "Local chemiluminescence spectra measurements in a high-pressure laminar methane/air premixed flame." *Proceedings of the Combustion Institute* 29 (2002): 1495-1501.

[17] Docquier, N., et al. "Experimental and numerical study of chemiluminescence in methane/air high-pressure flames for active control applications." *Proceedings of the Combustion Institute* 28 (2000): 1765-1774.

[18] Guiberti, T.F., D. Durox, and T. Schuller. "Flame chemiluminescence from CO2- and N-2-diluted laminar CH4/air premixed flames." *Combustion and Flame* 181 (2017): 110-122.

[19] Gupta, S.B., et al. "On use of CO2 chemiluminescence for combustion metrics in natural gas fired reciprocating engines." *Proceedings of the Combustion Institute* 33 (2011): 3131-3139.

[20] Parajuli, P., et al. "High-Speed Hydroxyl and Methylidyne Chemiluminescence Imaging Diagnostics in Spherically Expanding Flames." *AIAA Journal* 59, no. 8 (2021): 3118-3126.

[21] Syred, N. "A review of oscillation mechanisms and the role of the precessing vortex core (PVC) in swirl combustion systems." *Progress in Energy and Combustion Science* 32, no. 2 (2006): 93-161.

[22] Steinberg, A.M. and J.F. Driscoll. "Straining and wrinkling processes during turbulence-premixed flame interaction measured using temporally-resolved diagnostics." *Combustion and Flame* 156, no. 12 (2009): 2285-2306.

[23] Karlis, E., et al. "Extinction strain rate suppression of the precessing vortex core in a swirl stabilised combustor and consequences for thermoacoustic oscillations." *Combustion and Flame* 211 (2020): 229-252.

[24] Sick, V. "High speed imaging in fundamental and applied combustion research." *Proceedings of the Combustion Institute* 34 (2013): 3509-3530.

[25] Cheng, T.S., et al. "Chemiluminescence measurements of local equivalence ratio in a partially premixed flame." *Combustion Science and Technology* 178, no. 10-11 (2006): 1821-1841.

[26] Turns, S.R. *An Introduction to Combustion: Concepts and Applications.* 3rd

ed.: McGraw Hill, 2011.
[27] Yuan, Y., et al. "Characterization on hetero-homogeneous ignition of pulverized coal particle streams using CH* chemiluminescence and 3 color pyrometry." *Fuel* 184 (2016): 1000-1006.
[28] Mekhrengin, M.V., et al. "Multispectral pyrometer for high temperature measurements inside combustion chamber of gas turbine engines." *Measurement* 139 (2019): 355-360.
[29] Muruganandam, T.M., et al. "Optical equivalence ratio sensors for gas turbine combustors." *Proceedings of the Combustion Institute* 30 (2005): 1601-1609.
[30] Oh, J. "Spectral characteristics of a premixed oxy-methane flame in atmospheric conditions." *Energy* 116 (2016): 986-997.
[31] Hanson, R.K., C.S. Goldenstein, and R.M. Spearrin. *Spectroscopy and Optical Diagnostics for Gases.* 1st ed.: Springer, 2016. doi:10.1007/978-3-319-23252-2.
[32] Panoutsos, C.S., Y. Hardalupas, and A.M.K.P. Taylor. "Numerical evaluation of equivalence ratio measurement using OH* and CH* chemiluminescence in premixed and non-premixed methane-air flames." *Combustion and Flame* 156, no. 2 (2009): 273-291.
[33] Nori, V.N. and J.M. Seitzman. "CH* chemiluminescence modeling for combustion diagnostics." *Proceedings of the Combustion Institute* 32 (2009): 895-903.
[34] Kathrotia, T., Riedel, U., and Warnatz, J. "A Numerical Study on the Relation of OH*, CH*, and C2* Chemiluminescence and Heat Release in Premixed Methane Flames." In *Proceedings of the European Combustion Meeting*, 2009.
[35] Hu, X.Z., et al. "Investigation of laminar flame speeds of CH4/O-2/CO2 mixtures at ordinary pressure and kinetic simulation." *Energy* 70 (2014): 626-634.
[36] Kamal, M.M. "Two-line (CH*/CO2*) chemiluminescence technique for equivalence ratio mapping in turbulent stratified flames." *Energy* 192 (2020).
[37] McCord, W., et al. "Quantitative fuel-to-air ratio determination for elevated-pressure methane/air flames using chemiluminescence emission." *Applied Optics* 58, no. 10 (2019): C61-C67.
[38] Yang, J.B., et al. "Experimental studies of the effects of global equivalence ratio and CO2 dilution level on the OH* and CH* chemiluminescence in CH4/O-2 diffusion flames." *Fuel* 278 (2020).
[39] Zhu, X.R., et al. "Chemiluminescence signature of premixed ammonia-methane-air flames." *Combustion and Flame* 231 (2021).
[40] Tripathi, M.M., et al. "Chemiluminescence-based multivariate sensing of local equivalence ratios in premixed atmospheric methane-air flames." *Fuel* 93, no. 1 (2012): 684-691.
[41] Tripathi, M.M., et al. "A comparison of multivariate LIBS and

chemiluminescence-based local equivalence ratio measurements in premixed atmospheric methane-air flames." *Fuel* 106 (2013): 318-326.
[42] de Paulo, J.M., J.E.M. Barros, and P.J.S. Barbeira. "A PLS regression model using flame spectroscopy emission for determination of octane numbers in gasoline." *Fuel* 176 (2016): 216-221.
[43] Ballester, J., et al. "Chemiluminescence monitoring in premixed flames of natural gas and its blends with hydrogen." *Proceedings of the Combustion Institute* 32 (2009): 2983-2991.
[44] Yoon, T., et al. "Proper orthogonal decomposition of continuum-dominated emission spectra for simultaneous multi-property measurements." *Energy* (2022): 124458.
[45] Grauer, S.J., et al. "Instantaneous 3D flame imaging by background-oriented schlieren tomography." *Combustion and Flame* 196 (2018): 284-299.
[46] Krizhevsky, A., I. Sutskever, and G.E. Hinton. "Imagenet classification with deep convolutional neural networks." *Advances in neural information processing systems* 25 (2012): 1097-1105.
[47] Ioffe, S. and C. Szegedy. "Batch Normalization: Accelerating Deep Network Training by Reducing Internal Covariate Shift." In *Proceedings of the 32nd International Conference on Machine Learning*, edited by B. Francis and B. David, 448--456. Proceedings of Machine Learning Research: PMLR, 2015.
[48] He, K., et al. "Deep residual learning for image recognition." Paper presented at the Proceedings of the IEEE conference on computer vision and pattern recognition, 2016.
[49] Tian, C.W., et al. "Deep learning on image denoising: An overview." *Neural Networks* 131 (2020): 251-275.
[50] Simonyan, K. and A. Zisserman. "Very deep convolutional networks for large-scale image recognition." *arXiv preprint arXiv:1409.1556* (2014).
[51] Szegedy, C., et al. "Going deeper with convolutions." Paper presented at the Proceedings of the IEEE conference on computer vision and pattern recognition, 2015.
[52] Xu, Q., C. Zhang, and L. Zhang. "Denoising convolutional neural network." Paper presented at the 2015 IEEE International Conference on Information and Automation, 2015.
[53] Jain, V. and S. Seung. "Natural image denoising with convolutional networks." *Advances in neural information processing systems* 21 (2008).
[54] Zhang, K., et al. "Beyond a Gaussian Denoiser: Residual Learning of Deep CNN for Image Denoising." *Ieee Transactions on Image Processing* 26, no. 7 (2017): 3142-3155.
[55] Zhang, K., W.M. Zuo, and L. Zhang. "FFDNet: Toward a Fast and Flexible Solution for CNN-Based Image Denoising." *Ieee Transactions on Image Processing* 27, no. 9 (2018): 4608-4622.
[56] Abdelhamed, A., S. Lin, and M.S. Brown. "A high-quality denoising dataset for smartphone cameras." Paper presented at the Proceedings of the IEEE

Conference on Computer Vision and Pattern Recognition, 2018.
[57] Guo, S., et al. "Toward convolutional blind denoising of real photographs." Paper presented at the Proceedings of the IEEE/CVF conference on computer vision and pattern recognition, 2019.
[58] Lehtinen, J., et al. "Noise2Noise: Learning image restoration without clean data." *arXiv preprint arXiv:1803.04189* (2018).
[59] Batson, J. and L. Royer. "Noise2self: Blind denoising by self-supervision." Paper presented at the International Conference on Machine Learning, 2019.
[60] Krull, A., T.-O. Buchholz, and F. Jug. "Noise2void-learning denoising from single noisy images." Paper presented at the Proceedings of the IEEE/CVF conference on computer vision and pattern recognition, 2019.
[61] Manifold, B., et al. "Denoising of stimulated Raman scattering microscopy images via deep learning." *Biomedical Optics Express* 10, no. 8 (2019): 3860-3874.
[62] Zhang, G.S., et al. "Optimized adaptive Savitzky-Golay filtering algorithm based on deep learning network for absorption spectroscopy." *Spectrochimica Acta Part a-Molecular and Biomolecular Spectroscopy* 263 (2021).
[63] Miyatake, T., et al. "Denoising application for electron spectrometer in laser-driven ion acceleration using a Simulation-supervised Learning based CDAE." *Nuclear Instruments & Methods in Physics Research Section a-Accelerators Spectrometers Detectors and Associated Equipment* 999 (2021).
[64] Kim, Y., et al. "Deep learning-based statistical noise reduction for multidimensional spectral data." *Review of Scientific Instruments* 92, no. 7 (2021): 073901.
[65] Barwey, S., et al. "Using Machine Learning to Construct Velocity Fields from OH-PLIF Images." *Combustion Science and Technology* 194, no. 1 (2022): 93-116.
[66] Rodriguez, A., et al. "Retrieving soot volume fraction fields for laminar axisymmetric diffusion flames using convolutional neural networks." *Fuel* 285 (2021).
[67] Yoon, T., et al. "Deep learning-based denoising for fast time-resolved flame emission spectroscopy in high-pressure combustion environment." *Combustion and Flame* 248 (2023): 112583.
[68] Lavoie, J.M. "Review on dry reforming of methane, a potentially more environmentally-friendly approach to the increasing natural gas exploitation." *Frontiers in Chemistry* 2 (2014).
[69] Smith, R.C. *Uncertainty quantification : theory, implementation, and applications.* Computational science and engineering series. Philadelphia: Society for Industrial and Applied Mathematics, 2013.
[70] Tkaczyk, T.S. *Field guide to microscopy.* The SPIE field guides. Bellingham, Wash.: SPIE Press, 2010.

[71] Howell, S.B. *Handbook of CCD astronomy.* Vol. 5: Cambridge University Press, 2006.

[72] McCormick, D.T. "Line Array Sensor Comparison: Hamamatsu S11639, Sony ILX511B, Toshiba TCD1205DG." AdvancedMEMS, 2016.

[73] Rozenchan, G., et al. "Outward propagation, burning velocities, and chemical effects of methane flames up to 60 ATM." *Proceedings of the Combustion Institute* 29 (2002): 1461-1470.

[74] Akima, H. "A method of bivariate interpolation and smooth surface fitting based on local procedures." *Communications of the ACM* 17, no. 1 (1974): 18-20.

[75] Fahl, M. and E.W. Sachs, *Reduced order modelling approaches to PDE-constrained optimization based on proper orthogonal decomposition*, in *Large-scale PDE-constrained optimization*. 2003, Springer. pp. 268-280.

[76] Amsallem, D. and C. Farhat. "Interpolation method for adapting reduced-order models and application to aeroelasticity." *AIAA Journal* 46, no. 7 (2008): 1803-1813.

[77] Bai, Z.J. "Krylov subspace techniques for reduced-order modeling of large-scale dynamical systems." *Applied Numerical Mathematics* 43, no. 1-2 (2002): 9-44.

[78] Jeong, S., M. Murayama, and K. Yamamoto. "Efficient optimization design method using kriging model." *Journal of Aircraft* 42, no. 5 (2005): 1375-1375.

[79] Yoon, T. and K. Yee. "Design optimization of airfoil for wind turbine with respect to ice accretion." Paper presented at the 31st Congress of the International Council of the Aeronautical Sciences, 2018.

[80] Yao, W.G., et al. "A reduced-order model for gradient-based aerodynamic shape optimisation." *Aerospace Science and Technology* 106 (2020).

[81] Helton, J.C. and F.J. Davis. "Latin hypercube sampling and the propagation of uncertainty in analyses of complex systems." *Reliability Engineering & System Safety* 81, no. 1 (2003): 23-69.

[82] Sirovich, L. "Turbulence and the Dynamics of Coherent Structures .1. Coherent Structures." *Quarterly of Applied Mathematics* 45, no. 3 (1987): 561-571.

[83] Taira, K., et al. "Modal Analysis of Fluid Flows: An Overview." *AIAA Journal* 55, no. 12 (2017): 4013-4041.

[84] Brindise, M.C. and P.P. Vlachos. "Proper orthogonal decomposition truncation method for data denoising and order reduction." *Experiments in Fluids* 58, no. 4 (2017).

[85] Martin, J.D. and T.W. Simpson. "Use of kriging models to approximate deterministic computer models." *AIAA Journal* 43, no. 4 (2005): 853-863.

[86] Sobol, I.M. "Global sensitivity indices for nonlinear mathematical models and their Monte Carlo estimates." *Mathematics and Computers in Simulation* 55, no. 1-3 (2001): 271-280.

[87] Herman, J. and W. Usher. "SALib: an open-source Python library for sensitivity analysis." *Journal of Open Source Software* 2, no. 9 (2017).

[88] Saltelli, A., et al. "Variance based sensitivity analysis of model output. Design and estimator for the total sensitivity index." *Computer Physics Communications* 181, no. 2 (2010): 259-270.

[89] Sirven, J.B., et al. "Qualitative and quantitative investigation of chromium-polluted soils by laser-induced breakdown spectroscopy combined with neural networks analysis." *Analytical and Bioanalytical Chemistry* 385, no. 2 (2006): 256-262.

[90] van Noord, N. and E. Postma. "Learning scale-variant and scale-invariant features for deep image classification." *Pattern Recognition* 61 (2017): 583-592.

[91] Kingma, D.P. and J. Ba. "Adam: A method for stochastic optimization." *arXiv preprint arXiv:1412.6980* (2014).

[92] Loshchilov, I. and F. Hutter. "Sgdr: Stochastic gradient descent with warm restarts." *arXiv preprint arXiv:1608.03983* (2016).

[93] Bergstra, J., D. Yamins, and D. Cox. "Making a Science of Model Search: Hyperparameter Optimization in Hundreds of Dimensions for Vision Architectures." In *Proceedings of the 30th International Conference on Machine Learning*, edited by D. Sanjoy and M. David, 115--123. Proceedings of Machine Learning Research: PMLR, 2013. https://proceedings.mlr.press/v28/bergstra13.html.

[94] Zhang, R., et al. "Coupled interactions of a helical precessing vortex core and the central recirculation bubble in a swirl flame at elevated power density." *Combustion and Flame* 202 (2019): 119-131.

[95] Bohm, B., et al. "New Perspectives on Turbulent Combustion: Multi-Parameter High-Speed Planar Laser Diagnostics." *Flow Turbulence and Combustion* 86, no. 3-4 (2011): 313-341.

ABSTRACT (KOREAN)

연소환경 진단을 위한 고속 및 고정확도 화염 자발광 분광법에 관한 연구

윤 태 근
서울대학교 대학원
기계항공공학부

최근 연소의 효율성, 안정성 및 성능을 유지하면서 환경 문제에 대응하기 위해 많은 연소 기술이 개발되었다. 이러한 기술이 적용된 연소기를 최적으로 작동하기 위해 연소기 내부 화학 반응 영역의 가스 특성은 빠르고 정확하게 감시되고 즉각적으로 제어되어야 한다. 가스 특성을 측정하기 위해 화염 자발광 분광신호를 사용하는 화염 방출 분광법(FES, Flame Emission Spectroscopy)은 실시간으로 정확한 가스 특성 측정을 제공할 수 있는 기법의 하나다. 이는 화염 방출 분광법이 자발광을 이용한 비침입식 광학 측정으로 정확도가 높으며 광 검출 장비만을 사용하는 실험 특성으로 인해 고속 측정이 가능하기 때문이다. 그러나 정보 수집 속도를 높이기 위해 광 검출 장치의 노출 시간이 짧아짐에 따라, 화염의

자발광 분광신호의 신호 대 잡음비(SNR, Signal to Noise Ratio)가 낮아지고 FES 측정의 정확도가 감소한다. 그 뿐만 아니라 신호 대 잡음비가 높은 신호 수집이 가능하여도, 자발광으로 가스 특성을 직접 예측하는 것은 화학 발광의 완전한 화학 반응 경로 모델링이 요구되어 어렵다. 이에 따라 분광 신호로부터 가스 특성을 예측하는 것은 자발광과 가스 특성을 상호 연관시키는 보정 절차(Calibration process)에 의해 달성된다. 기존의 방법은 들뜬 상태인 화학종의 분광신호 면적 비율과 같은 국부적인 분광 신호 특징을 추출하고, 이 특징의 변화를 가스 특성과 연관 지어 일대일 보정 곡선을 이용한다. 그렇지만 분광신호 특징의 변화가 항상 단조로운 것은 아니므로 보정 프로세스가 간단하지 않다.

본 논문에서는 화염 방출 분광법을 이용한 가스 특성 예측의 시간 분해능과 정확도를 개선하기 위한 체계를 제안하였다. 1) 합성곱 신경망(CNN, Convolutional Neural Network) 구조에 기반한 신호 처리와 2) 적합 직교 분해(POD, Proper Orthogonal Decomposition) 및 크리깅 기법(Kriging Method)을 포함한 차수 축소 모델(ROM, Reduced Order Model) 보정을 결합한 데이터 기반 보정 체계 기법이다. 분광신호의 적합 직교 분해 기저를 포함한 손실 함수 및 잡음이 있는 데이터와 깨끗한 신호의 데이터 쌍으로 학습되는 딥 러닝 신경망은 정보 손실을 최소화하면서 신호 대 잡음비를 향상할 수 있다. 처리된 화염 분광신호를 가스 특성에 높은 연관

성을 가지는 분광신호의 직교 적합 분해 기저의 계수로 차수를 축소하고, 이 계수로 크리깅 모델을 활용하여 가스 특성 예측을 하였다. 결과적으로 제안된 보정 체계는 짧은 노출 시간을 가지는 신호를 사용하여 압력 및 연료 당량비 같은 다중 가스 특성의 예측 정확도를 향상할 수 있다.

제안된 새로운 기법을 실제 고압 메탄-공기 화염 신호에 적용하여, 고정확도 감지기로 측정된 실험값과 비교 및 제안된 기법의 정확도 및 정밀도를 분석하였다. 압력 및 연료 당량비의 특성 예측 정확도 및 정밀도는 임의의 실시간 측정을 나타내는 평가 분광 데이터(보정 체계 학습에 사용되지 않음)의 가스 특성 예측 평균 상대 오차(REP, average Relative Errors of Prediction) 및 평균 상대 표준 편차(RSD, average Relative Standard deviation)를 사용하여 정량화되었다. 제안된 방법은 메탄-공기 화염의 당량비(0.8 – 1.2)와 압력(1 – 10 bar)의 넓은 시험 범위에서 짧은 노출 시간(0.05, 0.2, 0.4 초)의 화염 자발광 신호를 이용하여 연소 조건의 가스 특성을 정확하게 예측하였다. 이를 통해 제안된 체계가 높은 정확도와 높은 시간 분해능의 화염 방출 분광법을 가능하게 할 수 있음을 확인하였다.

주요어: 연소환경 진단, 화염자발광, 화염 방출 분광법, 합성곱 신경망, 적합 직교 분해

학번: 2017-26386